Fermilab FERMILAB-THESIS-2003-02

A Measurement of the Z^0 Boson Production Cross Section Times Muon Branching Fraction in $p\bar{p}$ Collisions at 1.96 TeV

Gavin Hesketh

THE UNIVERSITY
of MANCHESTER

Particle Physics Group
Department of Physics and Astronomy
March 26, 2003

A thesis submitted to The University of Manchester for the degree of Doctor of Philosophy in the Faculty of Science and Engineering

Contents

List of Figures

List of Tables

Abstract

This thesis describes work carried out on the DØ experiment, a multi-purpose particle detector located on the Tevatron proton anti-proton collider in Illinois, USA. There is a summary of some technical work on the monitoring software for the new silicon detector at DØ, on a method to combine information from the different detector subsystems to improve particle identification and on work carried out to improve muon identification.

Finally, there is a preliminary measurement of the Z^0 boson production cross section (σ_Z) multiplied by muon branching fraction (B_μ) in $p\bar{p}$ collisions at 1.96 TeV. This measurement is made using data recorded during the commissioning phase of DØ, as a result of which faced several challenges. The final result obtained is:

$$\sigma_Z \times B_\mu = 309 \ \pm \ 31 \ \pm \ 51 \ \pm \ 31 \text{ pb}, \tag{1}$$

where the first uncertainty is statistical, the second systematic and the third due to the uncertainty on the luminosity. The result is consistent with the measurement in the electron channel and the theoretical prediction. The determination of many of the uncertainties is limited mainly by statistics, and the analysis will benefit hugely from recent improvements to both DØ and Tevatron performance.

Declaration

No portion of the work referred to in this thesis has been submitted in support of an application for another degree or qualification of this or any other university or other institute of learning.

The ownership of any intellectual property rights which may be described in this thesis is vested in the University of Manchester, subject to any prior agreement to the contrary, and may not be made available for use by third parties without the written permission of the University, which will prescribe the terms and conditions of any such agreement.

Further Information on the conditions under which disclosures and exploitation may take place is available from the Head of the Department of Physics and Astronomy.

The Author

The author was educated at Hurworth Comprehensive School, Hurworth, County Durham and at Queen Elizabeth Sixth Form College, Darlington, County Durham, before gaining a first class BSc(Hons) degree from the Department of Physics and Astronomy at the University of Manchester in 1996. The work presented here was undertaken in Manchester and at Fermilab, Illinois in 1999–2003.

Acknowledgements

Working in a large collaboration such as DØ inevitably means a great number of people do a great number of things. Most of these things you don't hear about very often, even if the experiment would no longer work if they stopped. So, it would be impossible to thank everyone who contributed to this thesis, or even just those whom I **know** made a contribution.

I was fortunate enough to work with a few different groups at DØ, and some of the people I'd like to thank include: Ela Barberis and Harald Fox in the SMT group; Herb Greenlee and Valentine Kousnetzov in the tracking group; Tom Diehl and the 'Muon Squad' in the Electroweak and Muon groups. I've had many useful discussions with many other people at Fermilab and in Manchester, so thank you to everyone who has helped me and answered my questions along the way.

I owe a huge debt of gratitude to my supervisor, Terry Wyatt, for helping and saving the analysis on more than one occasion, and for always being thorough, full of ideas and generally being an excellent physicist. Many thanks also to my editor in chief, Dr. Michiel Sanders, without whom I would probably have taken twice as long to produce a thesis of half the quality.

Of course, work was not the only thing that happened at DØ. Thanks to Dave and Sarah for barbies, beer and (too much) pizza; to Simon, Kyle and all the UK and other students for those nights in Quigleys. We also have pubs (and many other things) in Manchester, and fortunately the other HEP students based there (Manchester, not the pub) reminded me of this when I needed a break from writing. Finally, thanks to my parents, for always supporting me in what I do, to Frida, for being Frida, and to Tamsin, for being Tamsin.

Chapter 1

Introduction

One of the most powerful ideas to have emerged from physics is that the world we see is in fact made of microscopic ‘building blocks’. The current guise of this idea is the Standard Model, in which the building blocks are fundamental particles. Nuclei, atoms and molecules are formed from these fundamental particles, as well as many other short lived (composite) particles discovered in high energy physics experiments.

While the Standard Model is hugely successful at describing experimental data, it makes no attempt to explain the origins of the particles or forces observed in nature. Particle physics can be defined as the attempt to understand these origins. Experiments continue to test the Standard Model in new ways, searching for phenomena it cannot explain. Such a discovery would lead to the development of new, more powerful theories which in turn can be tested.

One way to search for new phenomena is to conduct experiments at higher and higher energies, corresponding to testing the theory down to smaller and smaller distance scales. The highest energy is currently achieved at the Tevatron proton anti-proton collider in Illinois, USA. DØ is one of the experiments on the Tevatron (the other being CDF). At the time of writing DØ is a relatively new experiment, having recently undergone a major upgrade, and this thesis describes some work related to the commissioning and understanding of the performance of DØ. There is also a preliminary measurement of the production rate of a certain type of particle, the Z^0 boson. This measurement reveals great deal about the performance of the experiment and our understanding of the underlying physics. Both of these things are vital to interpreting the results of many measurements to be made at DØ.

This introductory chapter is aimed at providing the basic background knowledge to the experiment and the measurement to be made. This necessarily includes a very brief conceptual overview of the Standard Model (section 1.1) and some of the basic principles of a particle physics experiment (section 1.2). Then, an introduction to the particle of interest, the Z^0 is given in section 1.3 and an overview of the production rate measurement is given in section 1.4.

1.1 The Standard Model

This section gives a basic overview of the Standard Model at the level required to understand the work described in this thesis. The interested reader is directed to textbooks such as [1, 2] for a more rigorous treatment.

The Standard Model is based on two of the great theoretical achievements of the 20th century: special relativity and quantum mechanics. It represents the world in terms of twelve fundamental spin 1/2 particles (fermions), each with an associated anti-particle. The fermions are organised in three ‘generations’, each generation containing two quarks (q) and two leptons (l). Particles in successive generations have similar properties but increasing masses. Forces between the fermions are mediated by the exchange of spin 1 particles (bosons). The fermions and bosons are summarised in table 1.1.

To describe the dynamics of the Standard Model, particles are treated as excitations of relativistic quantum fields. Interactions between the fermion and boson fields are introduced through symmetry arguments, known as *local gauge invariance*.

Quarks	charge = 2/3	u	c	t
	charge = -1/3	d	s	b
Leptons	charge = 0	ν_e	ν_μ	ν_τ
	charge = -1	e	μ	τ

Interaction	Boson
Electroweak	photon (γ), $W^{\pm}$, Z^0
Strong	gluons (g)

Table 1.1: The fermions and bosons of the Standard Model. Electric charges are measured in units of $e = -1\times$ the electron charge.

Symmetry plays an important role in physics. For example, rotational symmetry leads to the conservation of angular momentum. Requiring a gauge invariance in the Standard Model leads to the conservation of a ‘charge’ carried by the particle fields, the most familiar example of which is the electric charge.

Each symmetry can be classified by the group of transformations under which the physics is unchanged (rotations, for example). Gauge invariance is based on the groups of unitary transformations denoted by U(1) and SU(n) for $n > 1$, where n is the dimensionality of the gauge charge space. Each group has $n^2 - 1$ *generators* which change the configuration of the fields in the charge space.

The Standard Model is represented by the groups SU(3)×SU(2)×U(1), which are explained in sections 1.1.1 and 1.1.2.

1.1.1 Electroweak Theory

The first gauge invariant field theory was quantum electrodynamics (QED), which is based on U(1) group (invariance under a phase change). This leads to interactions between the photon and charged fermion fields and the conservation of electric charge. QED is one of the most successful the theories in physics and shows remarkable agreement with experiment.

Modelling the weak interactions proved more challenging. Glashow, Salam and Weinberg (GSW) found that replacing the U(1) group of electromagnetism with the more complex SU(2)×U(1) allows the weak force to be unified with the electromagnetic [3].

In the GSW electroweak theory, the three generators of the SU(2) group are the W^+, W^0 and W^-. The conserved charge is called *weak isospin*, and the fermions are arranged into weak isospin doublets, corresponding to the pairs of quarks and leptons in each generation of fermions in table 1.1. Absorption or emission of a W^+ or W^- changes the state of a doublet, for example:

$$\begin{aligned} \nu_e + \mathrm{W}^- &\rightarrow e^-, \\ t &\rightarrow b + \mathrm{W}^+. \end{aligned} \tag{1.1}$$

However, the SU(2) group has another generator, the W^0, which is not observed in experiments. It also does not explain the existence of the photon or Z^0, which are observed. To solve these problems a U(1) group is introduced, leading to the conservation of a charge known as *hypercharge*. This allows interactions between particles carrying hypercharge and an additional boson, the B^0. Then, the W^0 and B^0 mix, with orthogonal combinations of the two leading to the photon and Z^0. The electric charge is therefore a combination of weak isospin and hypercharge.

The SU(2)×U(1) theory successfully describes the interactions of the weak and electromagnetic bosons with fermions, as well as predicting interactions between the the electroweak bosons themselves, such as $\gamma \rightarrow \mathrm{W}^+\mathrm{W}^-$. The success of this theory has also lead to the hope that all forces can eventually be unified in a similar way.

The Higgs Mechanism

There is still a problem with the electroweak theory as it stands. Gauge invariance leads to massless particles, in contrast with the massive W and Z^0 observed in experiment. Therefore, a mechanism (known as electroweak symmetry breaking) is required to introduce particle masses without breaking the gauge invariance of the theory.

In the Standard Model, this is most simply achieved through the Higgs mechanism [4], which introduces an additional field with an associated particle, the higgs boson. Unlike the other fields, the higgs field has a non-zero vacuum expectation value (around 250 GeV), and other particles can acquire mass through interactions with this field. In fact, the particular combination of the W^0 and B^0 required to give a mass to the Z^0 and keep the photon massless leads to a relationship between the masses of the $\mathrm{W}^\pm$ and Z^0 bosons, which has been tested by experiment. The Higgs mechanism can also be used to generate the masses of the fermions, simply by introducing couplings to the higgs field. The strengths of these couplings then determine the masses of the fermions.

Feynman Diagrams

While the gauge invariant electroweak theory is mathematically beautiful, it is impossible to make a full calculation of an electroweak process. However, due to the small couplings of electroweak bosons, processes can be approximated by a perturbation series. Each term in the perturbation series can be represented by Feynman diagrams, providing a concise visual summary of the mathematics and giving a useful picture of what is actually going on. Figure 1.1 shows the leading order diagrams for the processes given in equation 1.1. Feynman diagrams are widely used in particle physics.

1.1.2 The Strong Force

The strong force is modelled by another gauge invariant theory: QCD (quantum chromodynamics), based on an SU(3) group, leading to the conservation of ‘colour’ charge. The three dimensions of colour space are labelled red, green and blue and the eight generators (gluons) change the colour state of particles. Both quarks and

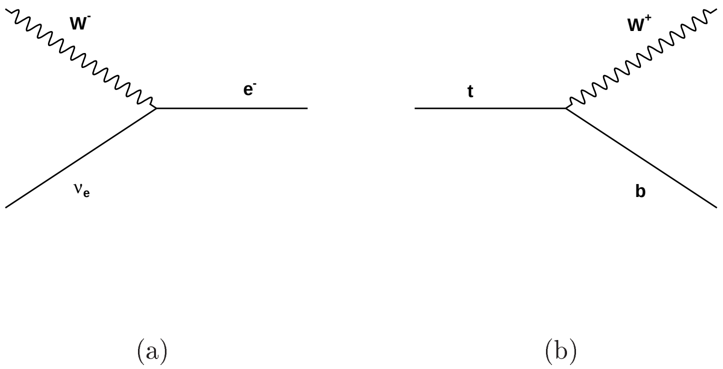

Figure 1.1: Leading order Feynman diagrams for the processes in equation 1.1. Time increases to the right in each diagram.

gluons carry colour, but the leptons are colourless and therefore do not couple to the strong force.

QCD calculations are significantly more complicated than for the electroweak force. At low energies, the QCD coupling is large, bound (colourless) states exist (mesons and hadrons) and a perturbation series cannot be applied. Another consequence of the larger coupling of the strong force is that free (unbound) quarks or gluons are never observed in the way that, for example, free electrons are. However, at higher energies the coupling of the strong force is weaker, so over small distances quarks and gluons can be considered 'free' and interactions approximated by a perturbation series. Eventually, the 'free' quarks and gluons *hadronise*, resulting in colourless bound states. QCD should eventually explain the mechanism of hadronisation but at the moment it is not fully understood.

At a proton anti-proton collider such as the Tevatron, the majority of interactions are due to the strong force. Electroweak processes such as Z^0 production are relatively rare, so one of the challenges facing the Tevatron experiments is to identify such rare events.

1.1.3 The Future of the Standard Model

One of the Standard Model predictions, the existence of the higgs boson, has yet to be confirmed. The search for the higgs boson (or more generally, the mechanism of electroweak symmetry breaking) is one of the main aims of particle physics in the coming years. Precision measurements of other parameters in the Standard Model place constraints on possible higgs masses. Most sensitive are the masses and couplings of particles, which are modified through higher order 'loop' processes, such as those in figure 1.2. As the higgs couples proportionally to mass, the heaviest particles (t, $\mathrm{W}^{\pm}$ and Z^0) reveal the most about the higgs. Currently the top and W masses are known to lowest precision, but over the next few years the Tevatron experiments will be able to improve these measurements. Also, it may be possible to directly produce the higgs boson at the Tevatron. This depends critically on the higgs mass and the amount of data collected, and may take several years [5].

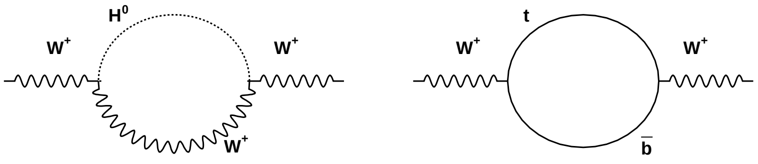

(a) (b)

Figure 1.2: Corrections to the W mass through loop diagrams. The size of the corrections are sensitive to the masses of the particles in the loops.

While the Standard Model is hugely successful, it contains many free parameters, including the field couplings and particle masses. It also makes no attempt to explain *why* the electroweak and strong forces exist, or *why* there are 12 fundamental fermions arranged in three generations.

There have been many attempts to extend the Standard Model and answer those questions, and also to include the fourth force in nature: gravity. A common approach is to follow the success of electroweak unification by incorporating the strong and electroweak forces into a larger gauge group. However, at the moment there is no experimental evidence to support any of these theories.

Two main approaches are used in searching for evidence of physics beyond the Standard Model. Increasing the precision with which parameters are measured may reveal deviations from Standard Model predictions - a sign on new physics. This approach relies upon clever experimental design and collecting large statistics with which to make the measurement. Experiments also continue to push the energy frontier higher and higher, which allows the Standard Model to be tested in completely new ways and may lead to the discovery of the higgs boson or entirely new phenomena. To understand how this is possible, a few words must be said about the basics of a particle physics experiment.

1.2 Basics of Experimental Particle Physics

An excellent introduction to experimental particle physics is given in [6], with some relevant issues reviewed here. The general aim is the study of the fundamental particles of the Standard Model and to search for new phenomenon, which may manifest as unusual interactions or the discovery of entirely new particles.

Most particles have very short lifetimes and must be created in a controlled environment before they can be studied. To do this, experiments use the equivalence of mass (m) and energy (E) predicted by special relativity theory:

$$E = mc^2, \tag{1.2}$$

where c is the speed of light [7]. By colliding particles at high energies, a different particle of larger mass can be created. By increasing the collision energy, previously unknown heavier particles may be discovered. For example the heaviest known particle, the top quark, has only been observed at the highest energy facility in the world, the Tevatron.

Energies in particle physics are usually measured in *electron volts*, eV, where 1 eV = 1.6 $\times 10^{-19}$ Joules. At modern high energy experiments it is more convenient to work in GeV (1 GeV = 10^9 eV) or TeV (1 TeV = 10^3 GeV). For example, the collision energy at the Tevatron is 1.96 TeV. It is also convenient to work in 'natural units', with $\hbar = c = 1$, in which case both momenta and masses can also be measured in electron volts. For example, a proton has a mass of just under 1 GeV and the top quark a mass of around 175 GeV.

To achieve the sort of energies required to produce, for example the top quark, the particles to be collided are accelerated with electromagnetic forces. This limits the choice of collision particles to those that are stable and charged: electrons and protons (as well as positrons and anti-protons). Large numbers of the chosen particle are accelerated in a beam, which can be made to collide with a fixed target or another beam. In the latter case (colliding beams), higher energies can be reached.

To make the most of the accelerated beams, they can be made to circulate in opposite directions around a storage ring, held in place by magnetic fields. This has two advantages: first, the particles can be accelerated over a period of time as they make many orbits of the ring; second, the beams can be made to collide many times at fixed points on the ring, at which the experiments are located.

The energies achievable in such circular accelerators are limited by the size of the ring and the strength of the magnetic fields which hold the beam in place. For example, the Tevatron has a circumference of around 6 km, and can accelerate protons to 0.98 TeV. The Large Hadron Collider (LHC, due to begin data taking in 2007) will operate in a 27 km circumference ring, accelerating protons to 7 TeV [8].

Another factor limits the energies achievable. The LHC tunnel was previously used by the Large Electron Position collider (LEP [9]), which reached a maximum centre of mass energy of around 210 GeV. In this case, bremsstrahlung radiation losses limited the energy that the beams could reach. These losses fall with the fourth power of the mass, so are much less significant for protons than electrons.

While they can reach higher energies, proton colliders (also known as hadron colliders) have one significant disadvantage from the experimental point of view, in that the proton is a composite particle. At the simplest level, it consists of three valence quarks: *uud*. The quarks are bound together by gluons, which carry a significant fraction of the proton momentum. There are also short-lived quantum fluctuations - quark anti-quark pairs, known as the quark sea. The gluons, valence and sea quarks are referred to as ‘partons’.

Proton anti-proton collisions can then be classified in two ways. First, *diffractive* collisions, in which either the proton or anti-proton (or both) remain intact. Diffractive collisions do not contribute to the analysis carried out in this thesis and are not discussed further.

The main type of collision of interest here results in both the proton and anti-proton dissociating. Dissociative collisions contain two processes: the ‘main’ collision or *hard scatter* in such an event, which is in fact a parton-parton collision; the remains of the proton and anti-proton typically continue close to the original beam direction, and form what is known as the *underlying event*.

There is no way to know in advance the fraction of the proton’s momentum carried into the hard scatter by each parton. So while the Tevatron collision energy is 1.96 TeV, each hard scatter contains less than this. The probability to find a parton with a certain momentum fraction is given by the parton distribution functions, which are measured experimentally.

The major advantage of electron positron accelerators is that electrons are (as far as we know) fundamental particles, so carry all of their energy into each collision. Thus, the collision energy can be precisely controlled. So, while electron-positron colliders cannot reach the energies of hadron colliders, they can make detailed studies of a particular particle by running with a collision energy equal to the mass of that particle. The LEP accelerator collected significant amounts of data at and around the Z^0 mass (approximately 91 GeV) and as a result, the Z^0 is one of the best understood particles in the Standard Model.

1.3 Z^0 Bosons at the Tevatron

At the Tevatron collision energy of 1.96 TeV, Z^0 production is dominated by leading order quark anti-quark annihilation (the *Drell-Yan* process [10]), shown in figure 1.3(a). The higher order processes in figures 1.3(b) and 1.3(c) contain an additional gluon or quark in the final state, which will appear as a 'jet' of hadrons.

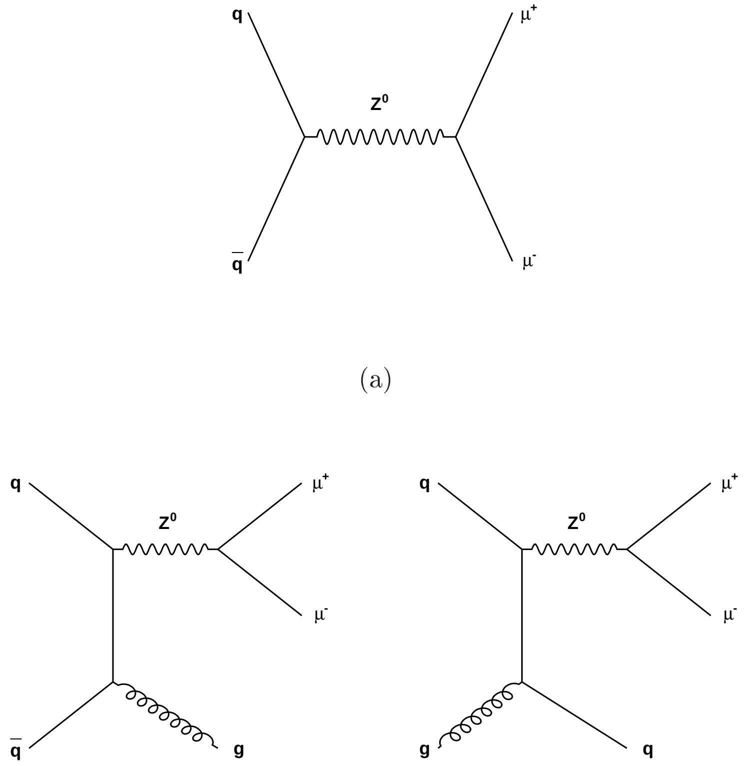

(a)

(b) (c)

Figure 1.3: Feynman diagrams showing (a) the leading order, (b) and (c) two higher order Z^0 production mechanisms in proton anti-proton collisions. The muon decay mode of the Z^0 is shown.

While a *real* Z^0 has a mass just over 91 GeV, the uncertainty principle of quantum mechanics allows the production of a *virtual* Z^0 with higher or lower mass. The probability for virtual Z^0 production falls significantly as the mass differs from 91 GeV and is quantified in terms of the *width*, which refers to the shape of the mass distribution of a particle. This is also related to the lifetime of a particle, with long lived particles only having small fluctuations in mass and therefore a small width.

The Z^0 has a width of around 2.5 GeV, corresponding to a lifetime of around 10^{-24} s in the rest frame, after which the Z^0 decays to a fermion anti-fermion pair. It couples to all of the 12 fermions in the Standard Model and the branching fractions to quarks and leptons have been measured at the LEP experiments (see, for example [11]). Some of the properties of the Z^0 and W bosons are given in table 1.2. Here, the *invisible* mode refers to decays to neutrinos or other undetected particles. The invisible branching fraction of the Z^0 is consistent with the existence of three types of neutrinos, matching the three generations of particles in the Standard Model.

	Z^0	$W^\pm$
Mass (GeV)	91.1876 ± 0.0021	80.423 ± 0.039
Full Width, Γ (GeV)	2.4952 ± 0.0023	2.118 ± 0.042
Partial Widths (%):		
l^+l^- (Z^0), $l\nu_l$ ($W^\pm$)	3.3658 ± 0.0023	10.68 ± 0.12
Hadrons	69.91 ± 0.06	67.96 ± 0.35
Invisible	20.00 ± 0.06	-

Table 1.2: Some properties of the W and Z^0 bosons, taken from [11].

In a hadron collider such as the Tevatron, the electron and muon channels are experimentally the easiest to identify, with significant backgrounds to the quark channels from other (mainly QCD) processes. The muon channel is used in this thesis. In the laboratory rest frame Z^0 bosons will be produced with a range of momenta, determined by the momenta of the colliding partons. In the Z^0 rest frame, each muon will carry away energy equivalent to half of the Z^0 mass, a signal for the production and decay of a Z^0 thus being the presence of two high energy muons. By measuring the 4-momenta of these muons, it is possible to reconstruct the mass of the Z^0 and many of its other properties. Therefore, to study the Z^0 or any short lived particle, DØ must be able to identify and measure its decay products, such as muons.

1.4 Cross Section Measurement and Other Work

This thesis contains a measurement of the production rate of Z^0 bosons in $p\bar{p}$ collisions at 1.96 TeV. This rate is parameterised in terms of a *cross section*, which takes into account the number of collisions to provide a measurement which can be compared with other experiments. The number of collisions is measured in terms of the beam intensity or *luminosity*, determined by the density of particles within the beam (see, for example, [11]). The *instantaneous* luminosity gives a measure of the collision rate at any time. After a period of running, the *integrated* luminosity gives a measure of the total number of collisions that have occurred.

In fact, the cross section multiplied by the branching fraction to a particular channel is measured. In this case the muon channel is used, so the cross section measures the rate of:

$$\mathrm{p\bar{p}} \rightarrow \mathrm{Z}^0 \ + \mathrm{X} \rightarrow \mu^+\mu^- + \mathrm{X}, \tag{1.3}$$

where X represents any other particles which may be produced. A similar analysis has also been carried out in the electron channel at DØ. As the Z^0 branching fractions to electrons and muons are the same (within experimental uncertainties), the electron and muon analyses should yield similar results.

The first stage of the cross section measurement involves identifying the signal of interest in the available data sample. The data available for this thesis were recorded from March–May 2002, during the commissioning phase of the DØ experiment. Chapters 3 to 5 of this thesis focus on technical work related to the detector and reconstruction tools used to identify the Z^0 signal in the muon channel in these data.

The cross section measurement itself was also complicated by the fact that the experiment was still in the commissioning phase. Part of the analysis involves measuring the efficiency with which $Z^0 \rightarrow \mu^+\mu^-$ events are detected, and this proved difficult. Indeed, this analysis contains the first measurement of all of the components of this efficiency at DØ in Run II. The methods that had to be adopted are somewhat complicated, but necessary given the status of the experiment at the time.

The analysis is also severely limited by the statistics available. The integrated luminosity used corresponds to around 0.2 % of the integrated luminosity that DØ hopes to collect over the next 2-3 years. If this integrated luminosity is delivered, DØ should record several hundred thousand $Z^0 \rightarrow \mu^+\mu^-$ events, but for this analysis only around 150 were available.

Although an improved measurement will certainly be made once DØ has collected more luminosity, the Z^0 is actually incredibly useful in the early phase of an experiment. Following the LEP experiments, the Z^0 is such a well understood particle that it can be used as a calibration tool for other experiments, such as DØ. It provides a very 'clean' physics signal (two high energy muons in this case) which can be used to test and improve the performance of the experiment and analysis tools that have been developed.

The precision achieved at LEP also means that DØ will never be able to produce competitive measurements of the properties of the Z^0. However, a measurement of the Z^0 production rate at a hadron collider such as the Tevatron is an important test of our understanding of the strong force and the composition of the proton, in terms of the parton distribution functions.

Normally, the Z^0 cross section is measured together with that of the other massive electroweak boson, the W. Unfortunately it was not possible to identify the W signal in the muon channel in the data used for this thesis. However, as more data are collected, the Tevatron experiments will be able to provide the world's best precision on many of the properties of the W boson, which are currently known to an order of magnitude lower precision than the properties of the Z^0 (see table 1.2). Of particular interest are the mass, which constrains the possible higgs boson mass, and width, which tells us about the decay modes of the W and is sensitive to the existence of non-Standard Model particles. The W width can actually be extracted from the ratio of the Z^0 and W cross sections, as explained in Chapter 6, so it is disappointing that this could not be measured at the time of writing.

The rest of this thesis then falls into the following chapters:

- Experimental Apparatus.

  A brief description of the Tevatron and the DØ experiment, including the basic principles behind a particle detector.

- The Silicon Microstrip Tracking Detector at DØ.

  The silicon microstrip tracker is an important part of the DØ upgrade for Run II. This chapter describes some work carried out developing the monitoring framework for this detector, to ensure the design performance is achieved.

- Particle Tracking and Track Extrapolation.

  This chapter describes some technical work carried out to combine information from different particle detectors at DØ. There is also a review of some of the technical challenges encountered during the commissioning phase of DØ.

- Muon Identification

  Here, the basics of muon identification at DØ are reviewed. This is followed by a description of work carried out to obtain the best possible muon identification in the data available for this thesis, including the identification of the $Z^0 \rightarrow \mu^+\mu^-$ signal.

- Cross Section Measurement

The first Z^0 production cross section multiplied by muon branching fraction measurement at DØ in Run II is presented.

Chapter 2

Experimental Apparatus

DØ is an experiment on a proton anti-proton collider operating at a centre of mass energy of 1.96 TeV, making it the highest energy facility in the world. This chapter gives an overview of the Tevatron, which produces the collisions, and the particle detector used to study them.

In 2001 the Tevatron began Run II, the second major period of data taking. During Run I (1993-1996), a total integrated luminosity of around 100 pb^{-1} was delivered. For Run II the Tevatron has been upgraded, to allow an increase in beam energy (0.8 to 0.98 TeV in each beam) and luminosity. An integrated luminosity of 2 fb^{-1} is expected within a couple of years (Run IIa), representing a factor of 20 increase over the whole of Run I. Then, after further upgrades, the Tevatron will switch to higher luminosity running (Run IIb), continuing data taking until being superseded by the LHC experiments.

2.1 The Tevatron

The Tevatron ring at Fermilab is the final stage in a chain of accelerators which produce high energy beams of protons and anti-protons. The design and operation of this accelerator chain is reviewed in some detail in [12, 13] and only the basics of Tevatron operation is given here. The accelerator chain is shown in figure 2.1.

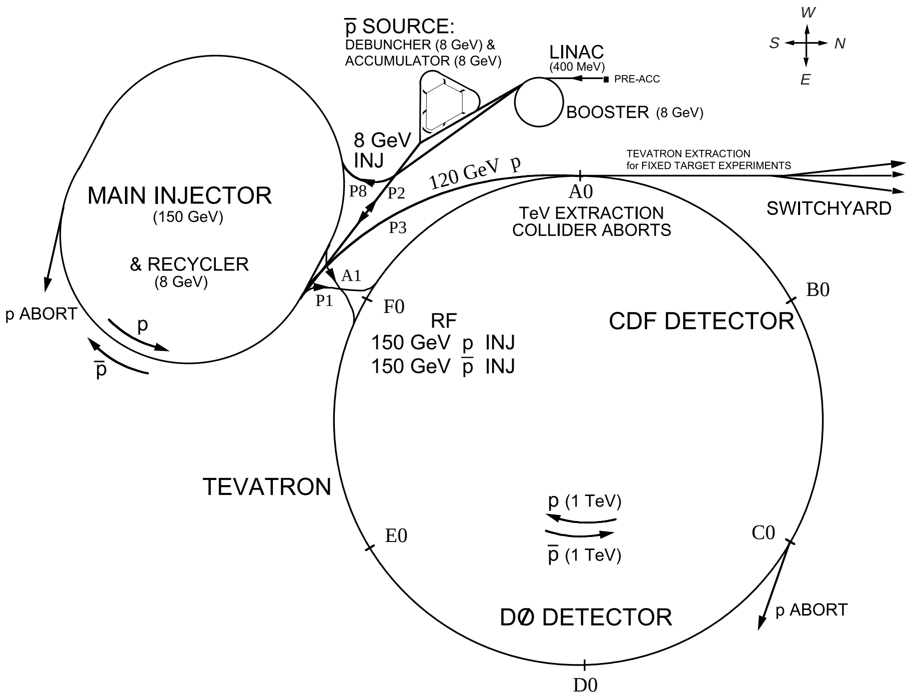

Figure 2.1: The accelerator chain at Fermilab.

The proton beam begins as H^- ions, which are passed through a Cockroft-Walton accelerator and then a 500 ft linear accelerator, reaching energies of 400 MeV. The electrons are then stripped off as the ions pass through carbon fibre foil, giving a beam of protons. The protons are accelerated to 8 GeV in the Booster synchrotron ring before being transferred to the Main Injector, a larger synchrotron ring where they are accelerated to 150 GeV. The Main Injector forms the protons into a bunch structure before delivering them to the Tevatron, where the bunches are accelerated to 0.98 TeV.

Bunches of protons from the Main Injector are also used to produce anti-protons. 120 GeV protons are directed at a nickel/copper target, producing anti-protons with a range of momenta. The anti-protons are collected and moved to the Debuncher storage ring, where they are focused into a coherent beam and accelerated to 8 GeV before being transferred to the Accumulator, another storage ring. Once sufficient numbers of anti-protons have been collected in the Accumulator, they are passed to the Recycler and on to the Main Injector, where they are accelerated to 150 GeV for transfer into the Tevatron, circulating in the opposite direction to the proton beam.

The Tevatron has six possible $p\bar{p}$ collision points, labelled A0 – F0. The two experiments currently on the Tevatron are located at B0 (the CDF experiment [14]) and D0 (the DØ experiment). The Run IIa operating plan has the Tevatron initially delivering 36×36 $p\bar{p}$ bunches, with 396 ns spacing between each bunch (and correspondingly 396 ns between bunch crossings in each experiment). The 36 bunches in each beam are organised into 3 super-bunches of 12, with a longer (around 2 μs) gap between each super-bunch. To achieve higher luminosities later in Run IIb, the number of bunches in each super-bunch can be increased to 36, with the spacing between bunches reduced to 132 ns. This high bunch crossing rate may be necessary to gain sufficient statistics to study the rare processes which form the main aims of Run II.

2.2 The DØ Experiment

DØ is a multi-purpose particle detector designed to study $p\bar{p}$ collisions at 1.96 TeV. To do this, it is necessary to identify and measure the properties of particles produced in those collisions. Many short lived particles decay before it is possible to measure them, so they must be reconstructed from their decay products. Any quarks or gluons produced are not observed directly, as they form jets of hadrons. In general, there are six distinct types of particles with long enough lifetimes to be detected: photons, electrons, muons, neutrinos as well as charged and neutral hadrons. These can be identified and measured by their different interactions with matter. To understand how this is achieved at DØ, a brief description of those interactions is given in section 2.3.

An overview of the DØ detector is given in sections 2.4 to 2.7. This is followed by a description of the event trigger systems used to identify interesting collisions (in section 2.8) and event reconstruction and simulation (in section 2.9).

This discussion is aimed at providing a background to the technical work described in Chapters 3 to 5 and the $Z^0 \rightarrow \mu^+\mu^-$ analysis in Chapter 6. However, some of the relevant details are postponed until those chapters, where they are discussed in more detail.

2.3 Particle Interactions With Matter

The main method used to detect and measure the properties of particles is to look for energy deposited as those particles pass through a layer of material. Energy loss for charged particles through excitation and ionisation is discussed in section 2.3.1. For high energy electrons, however, the dominant form of energy loss is through photon radiation. High energy photons themselves can convert to electron-positron pairs. These effects are discussed in section 2.3.2. Hadrons can also undergo strong force interactions with the nuclei of the medium. This is also discussed in section 2.3.2. The final interaction covered is the scattering of charged particles from the nuclei of a medium, with little energy lost (section 2.3.3).

2.3.1 Ionisation and Excitation

All charged particles passing through a medium undergo electromagnetic interactions. These interactions typically result in energy loss through excitation and ionisation of the atoms in the medium. This energy loss is theoretically described as photon exchange with atomic electrons, with the average rate, $\mathrm{d}E/\mathrm{d}x$, where x is the distance travelled in the medium, is given by the Bethe-Bloch equation (see, for example [11]). Due to the large number of interactions, statistical fluctuations in this rate are small.

The average rate varies with the kinematic variables $\beta\gamma$, where β is the velocity as a fraction of the speed of light, and $\gamma = (1 - \beta^2)^{-1/2}$. This is shown in figure 2.2 for muons incident on copper.

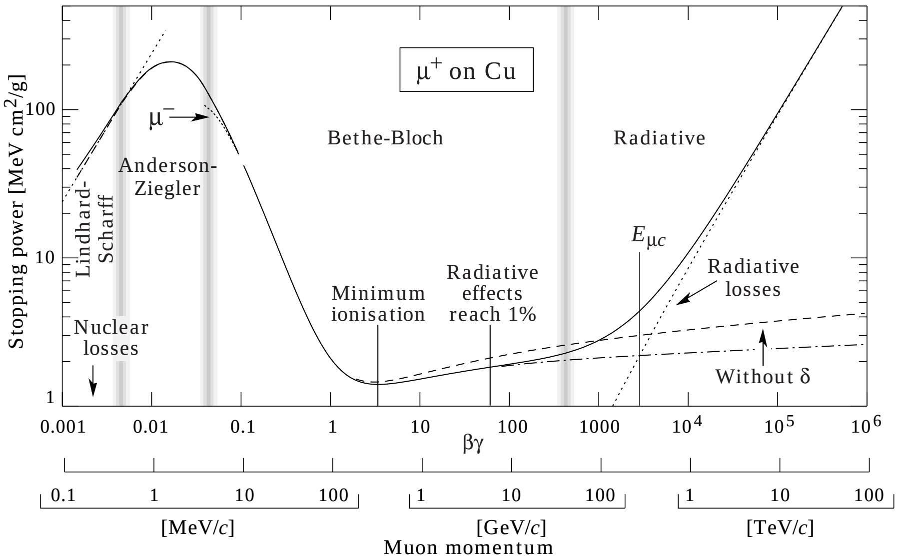

Figure 2.2: The stopping power ($= -\frac{1}{\rho}\frac{\mathrm{d}E}{\mathrm{d}x}$) of copper for incident muons.

It can be seen from figure 2.2 that at low $\beta\gamma$, particles lose energy at a rate proportional to $\beta\gamma$. As $\beta\gamma$ increases, the rate of energy loss falls, reaching a minimum before slowly rising due to radiative effects. The value of $\beta\gamma$ at which this minimum occurs varies little for different particles or different materials.

Energy loss measurements can be used to differentiate between low energy particles. For example, electrons reach the minimum at momenta of a few MeV. Protons reach minimum ionisation at around 3 GeV.

As the rise of the rate of energy loss above the minimum is slow, high energy particles are generally referred to as minimum ionising particles (MIPs). Above a few GeV, most long lived particles are above this minimum and lose energy at approximately the same rate.

So, while the rate of energy loss does not provide particle identification at high energies, the resulting ionisation and excitation can be used to detect particles. Ionisation results in the production of free electrons and ions. Many modern particle detectors use semiconducting devices, in which ionisation produces free electrons and ‘holes’. Excitation results in photon emission as the excited electrons return to lower energy levels. In some materials, photons from certain transitions are in, or close to, the visible range of the spectrum. This is referred to as scintillation light.

Charged particle detection is based upon collecting ionised charge or scintillation light. In tracking detectors, this is used to record the path of charged particles. Calorimeters absorb particles completely, giving a measure of energy.

2.3.2 Shower Formation

Shower formation is the name given to the generation of secondary particles by the interaction of a high energy particle with material. These secondary particles take a fraction of the initial particle’s energy and generally move in approximately the same direction. The showering properties of electromagnetic objects, such as electrons and photons, are different from those of hadrons and so each will be discussed separately. These differences can form the basis of particle identification.

Electromagnetic Showers

High energy photons and electrons produce showers of secondary electrons and photons, called electromagnetic showers. The production mechanisms for such a shower are described below.

Electrons

> The dominant method of energy loss for electrons with energies above a few hundred MeV is photon emission (*bremsstrahlung*). This can be parameterised in terms of the *radiation length,* X_0, the average distance over which an electron will lose all but a fraction e^{-1} of its original energy through bremsstrahlung. The radiation length of a material is given approximately by:

$$X_0 = \frac{716.4\ A}{\rho Z(Z-1)\ \ln(287/\sqrt{Z})}\ \text{cm}. \tag{2.1}$$

Where A is the atomic mass, Z is the atomic number and ρ is the density of the material in question [11].

An electron will continue to emit bremsstrahlung radiation until its energy falls below the critical value, E_c, at which ionisation energy losses begin to dominate. The critical energy is a function of the atomic number of the material and is typically of order 100 MeV. While particles other than electrons can lose energy through bremsstrahlung, the rate falls approximately with the square of the mass of the particle in question. For muons, the critical energy is typically around a TeV and for hadrons even higher. Thus for the energies reached at the Tevatron, bremsstrahlung losses can be neglected for all particles except electrons.

Photons

In the presence of an external electromagnetic field, such as that of the nuclei of a material, high energy photons convert to electron-positron pairs. This process can also be parameterised in terms of the radiation length of the material the photon is traversing. The mean distance travelled by a photon before converting to an e^+e^- pair is given by $\frac{7}{9}X_0$. The e^+e^- pair will then produce more photons through bremsstrahlung until dropping below the critical energy. For photons of lower energy, Compton scattering and photoelectric effects dominate, producing atomic excitations and, in certain materials, scintillation light.

An electromagnetic shower thus develops through bremsstrahlung and pair production. The number of particles in the shower will depend on the energy of the initial particle. A calorimeter essentially counts the number of particles produced, thus measuring the energy.

Hadronic Showers

While hadrons lose energy primarily through ionisation rather than bremsstrahlung, they can also undergo strong force interactions with the nuclei of the material. These strong force interactions are typically inelastic, involving the production of secondary quarks or gluons which then hadronise, leading to the development of a hadronic shower.

The length scale for hadronic showering is the nuclear interaction length, given approximately by [11]:

$$\lambda_I \;=\; \frac{35\ A^{\frac{1}{3}}}{\rho}\ \text{cm.} \tag{2.2}$$

The nuclear interaction length is typically an order of magnitude larger than the radiation length of a particular material. This gives rise to the significantly different character of electromagnetic and hadronic showers.

Neutral hadrons, such as neutrons and K^0_L do not ionise directly, but become detectable through hadronic interactions producing charged particles. Neutral pions decay rapidly to two photons and can produce an electromagnetic component in a hadronic shower.

2.3.3 Coulomb Scattering

As well as transferring energy to electrons as described in section 2.3.1, a charged particle can also scatter off the nuclei in a material. This Coulomb scattering is well described by the theory of Molière [15] and generally results in a small deflection of the path of a particle, with almost no loss of energy. The total effect on the path of a particle through a layer of material is the result of many such individual (mostly small angle) scatters. As with Rutherford scattering, small impact parameters can produce large scattering angles.

The mean scattering angle falls with increasing particle momentum and radiation length of the material in question [11]. From the point of view of tracking, it is desirable to build detectors which minimise this scattering. This is achieved by using thin layers of material, or a material with a large radiation length, such as a gas. Multiple scattering is discussed in more detail in section 4.3.2.

2.4 An Overview of the DØ Detector

The DØ detector combines tracking, calorimetry and muon detection over a wide angular range. A cross section view of DØ is shown in figure 2.3, followed by a review of the coordinates and parameters used at DØ and a brief overview of each detector subsystem. A more detailed description of the DØ detector is given in [16].

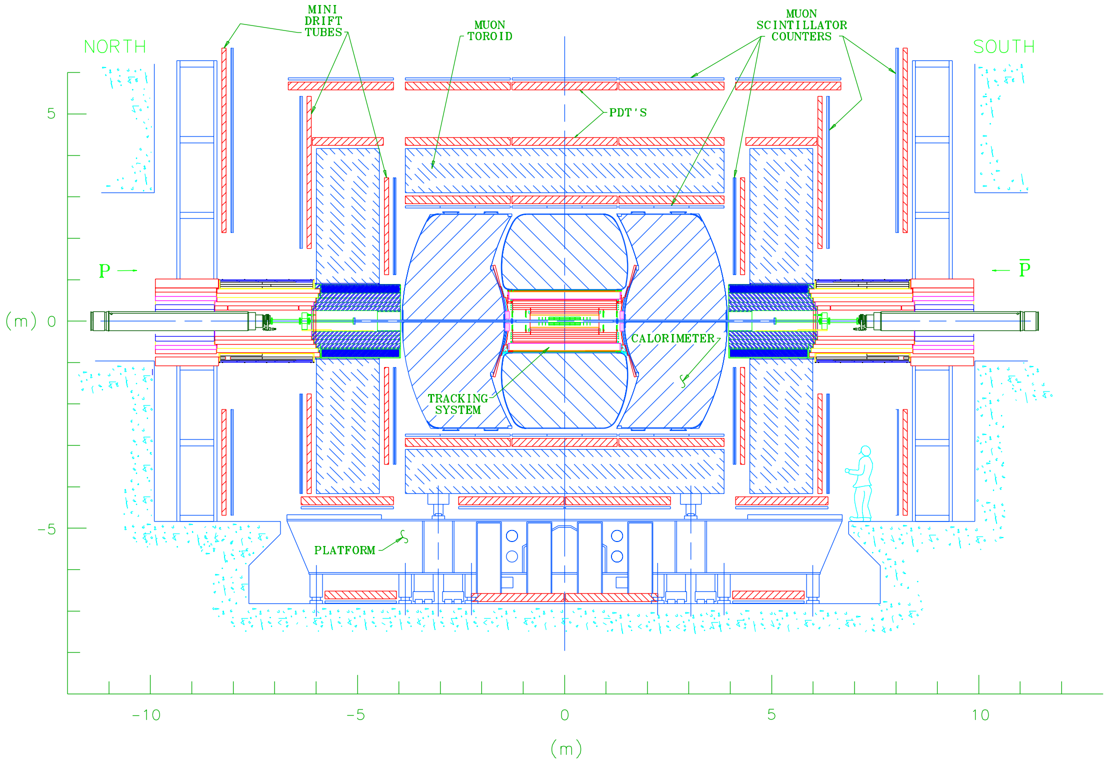

Figure 2.3: A cross section view of the DØ detector.

2.4.1 DØ Coordinates

When measuring positions and directions at DØ, a right-handed co-ordinate system is used. The proton beam defines the z axis, with the anti-proton beam thus travelling in the negative z direction. The x axis points toward the centre of the Tevatron ring and y points vertically. The DØ detector is centred at (0,0,0) in these co-ordinates. The interaction region has a Gaussian distribution in z, centred at $z = 0$ with an RMS of around 25 cm.

The usual azimuthal angle, $\phi = \tan(\mathrm{y}/\mathrm{x})$, is used. However, as DØ is generally not in the centre of mass frame of each collision, the polar angle θ is replaced by *pseudo-rapidity*, η, defined by:

$$\eta = -\ln(\tan(\theta/2)). \tag{2.3}$$

Pseudo-rapidity is derived from *rapidity*, defined by:

$$y = \frac{1}{2}\ln\left(\frac{E + p_z}{E - p_z}\right) = \tanh^{-1}\left(\frac{p_z}{E}\right), \tag{2.4}$$

where E is the energy and p_z the z momentum component of a particle. Rapidity has the advantage that the multiplicity of high energy particles ($\mathrm{d}N/\mathrm{d}y$) is covariant under Lorentz transformations along the z axis. Pseudo-rapidity is approximately equal to rapidity for relativistic particles (i.e. most particles observed at DØ). The η co-ordinate is used in two ways: *detector* η refers to the position of a particle relative $z = 0$; *physics* η refers to the position of a particle relative to the actual z position of the interation from which it came. For an un-deflected particle originating at $z = 0$ physics η and detector η are identical.

While the z momentum components of the colliding partons is not known, the transverse components are generally small (approximately zero). Thus the transverse momentum is a useful parameter, defined by:

$$p_T = \sqrt{p_x^2 + p_y^2}. \tag{2.5}$$

Similarly, the total transverse energy of the particles produced in a collision will sum to zero. Any undetected particles, such as neutrinos, then become apparent as *missing transverse energy*, an imbalance in the total transverse energy in an event.

2.4.2 Detector Subsystems

Tracking System

The paths of charged particles are recorded by the DØ tracking system. This consists of two components: the silicon microstrip tracker (SMT) and the central fibre tracker (CFT) which are described in section 2.5. The tracking system is surrounded by a solenoid magnet providing a magnetic field of 2 T in the z direction.

Calorimetry

The DØ calorimetry system provides particle identification and energy measurements by completely absorbing most particles. It consists of the pre-shower detectors, immediately outside the solenoid magnet, and the main calorimeter. These are described in section 2.6

Muon Detectors

High energy muons penetrate inner detectors and are identified in a second tracking system located outside the calorimeter. This includes a toroid magnet, allowing another measurement of momentum. The muon system is described in section 2.7

Shielding

Iron shielding surrounds the beam pipe outside the DØ calorimeter. This significantly reduces beam remnant activity in the muon system at large η.

Luminosity Monitors

In an inelastic p$\bar{\text{p}}$ collision, the remnants of the proton and anti-proton will typically be detected by the luminosity monitors [17], consisting of scintillating material placed around the beam pipe at $z = \pm 140$ cm. When there is a coincidence of hits in the monitors on either side of the interaction region, the relative hit times also give a measurement of the z position of the collision, to within approximately 6 cm. Hit coincidences can be used to trigger on inelastic collisions and are also summed over one minute periods. Then, with the total inelastic p$\bar{\text{p}}$ cross section, these are used to measure the total luminosity seen by DØ (see section 2.8.1).

2.5 Central Tracking Detectors

The two detector components located inside the DØ solenoid magnet are referred to as the central tracking detectors. These are the silicon microstrip tracker and scintillating fibre tracker. The solenoid magnet itself is discussed in some detail in [18].

The basic idea of the central tracking system is to make accurate position measurements along the paths of charged particles. In the presence of the magnetic field provided by the solenoid, these paths will be curved. By measuring the radius of this curve, the component of the particle momentum perpendicular to the magnetic field can be extracted. The accuracy of this measurement is affected by the individual position measurement resolutions and by the amount of multiple scattering. The desire to maximise the first and minimise the second of these factors places requirements on the design and construction of the central tracking system.

2.5.1 Silicon Microstrip Tracker (SMT)

The SMT is a high precision device surrounding the beam pipe in the centre of DØ. Tracking information from the SMT significantly improves the momentum resolution and vertex reconstruction capabilities of DØ.

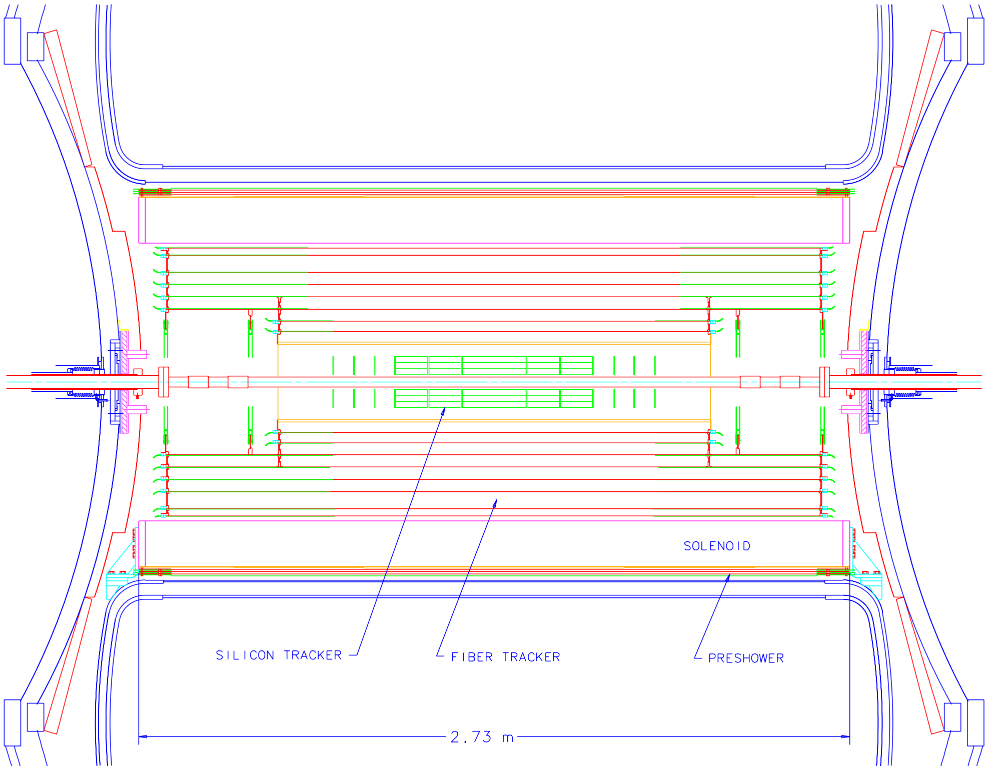

Figure 2.4: The central tracking detectors at DØ.

The sensitive devices in the SMT are wafers of n-type silicon, which is ionised by the passage of charge particles. The ionised charge is collected and used to measure the position of the passing particle.

Wafers are arranged parallel to the beam direction in four layers covering the region $|z| < 40$ cm to provide the best tracking for particles at small η. The layers are evenly spaced between radii of 2.5 and 10 cm. There are also 16 layers of wafers perpendicular to the beam, extending to $|z| = 250$ cm, to improve tracking for particles at large η. The design, operation and readout of the SMT are discussed in detail in Chapter 3 and in [19].

2.5.2 Central Fibre Tracker (CFT)

The CFT consists of eight carbon fibre cylinders holding layers of scintillating fibres arranged in radial doublets [20]. The outer fibre in each doublet is offset by half a fibre width, improving the angular coverage. The fibres themselves, double clad to improve light transmission, are 835 μm in diameter, giving a position resolution per doublet of 100 μm.

Even numbered cylinders hold one layer of doublets running parallel to the beam (*axial*), providing a measurement of ϕ at a known radius. Odd numbered cylinders hold an additional doublet offset at alternating angles of $\pm 3^\circ$ (*stereo*). When the information from the axial and stereo doublets is combined, a measurement of z is also possible.

The inner two cylinders, at radii of 19.5 and 23.4 cm, extend to ± 83 cm in z, with each fibre running the full length of the cylinder. The outer six cylinders, at radii of 28.1, 32.8, 37.5, 42.1 48.8 and 51.5 cm extend to ± 128.5 cm in z. In total there are 71,680 fibres in the CFT.

The passage of charged particles through a fibre causes scintillation. The scintillation light will travel along the fibre in both directions. At one end, an aluminium mirror reflects the light back down the fibre. At the other end, the fibre is joined to a wavelength shifting waveguide which transmits the light to a solid state device called a Visible Light Photon Counter (VLPCs) [21], located below the DØ calorimeter, which converts the light into an electronic signal. The VLPCs have an optimum operating efficiency at 6–15 K, so are held in a liquid helium cryostat.

The readout of the CFT is then very similar to that of the SMT, which is described in section 3.2.

2.5.3 Momentum Resolution

For a magnetic field (B) in the z direction, the curvature of the path of a charged particle, (κ), is given by [11]:

$$\kappa = \frac{1}{R} = 0.3B\frac{q}{p_T}. \tag{2.6}$$

Where R is the radius of curvature in metres, q is the charge of the particle in units of e, and p_T, measured in GeV, is the component of its momentum perpendicular to the magnetic field. The factor of 0.3 is due to the choice of units. So by measuring R, the value of q/p_T can be found.

The uncertainty on the measured curvature has two components: one from the multiple scattering of particles as they pass through the material of the detector; the other is from the measurement resolution, which is determined by the individual hit resolution and the square of the measured track length. Thus tracks measured in the SMT and CFT have significantly better momentum resolution than tracks measured in the SMT or CFT alone.

The momentum resolution expected for the DØ tracking system is shown in figure 2.5 and can be parameterised for tracks at $\eta = 0$ by:

$$\frac{\Delta p_T}{p_T} = \sqrt{0.015^2 + (0.0014 p_T)^2}, \tag{2.7}$$

where, again, p_T is measured in GeV [20]. The decrease in resolution above $|\eta| = 1.6$ is caused by the limit of the CFT coverage. The subsequent increase in resolution above $|\eta| = 2.1$ is where the coverage of the forward SMT disks begins.

2.6 DØ Calorimetry

The DØ calorimeter uses a sampling approach. A layer of dense material is included to induce the formation of 'showers' of secondary, lower energy particles (see section 2.3.2). This dense material is followed by an 'active' layer, which is ionised by the shower.

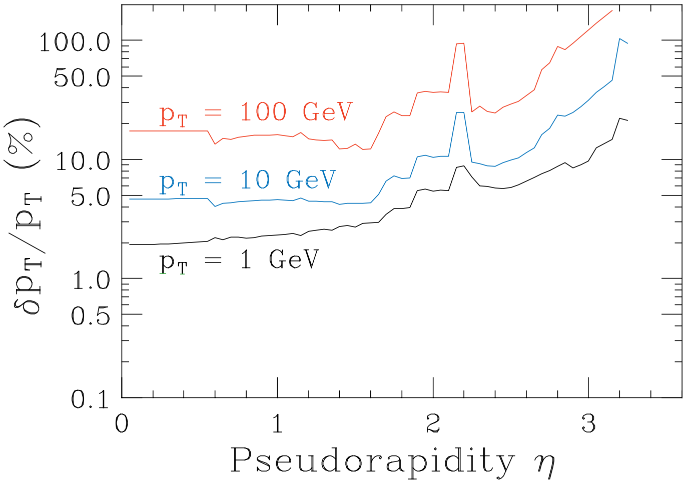

Figure 2.5: The expected fractional p_T resolution for the DØ central tracking system [16]. The resolution is shown as a function of pseudo-rapidity for tracks of three different transverse momenta originating at $z = 0$.

2.6.1 Pre-shower Detectors

The pre-shower detectors use a mixture of tracking and calorimetry. The basic principle is to introduce some material before the pre-shower detectors to induce electromagnetic, but not hadronic, shower formation. Then, with sufficient detector resolution, it is possible to separate electromagnetic objects from hadrons.

At DØ, the pre-shower detectors are made of three thin layers of scintillating material on the inner edge of the calorimeter. To induce showering, thin layers of lead are placed before the scintillators. In the central angular region ($|\eta| < 1.2$), the lead is added to the outer edge of the solenoid, giving a combined thickness of 2 radiation lengths. The scintillating material then fits inside the 51 mm gap between the lead layer and the calorimeter. In the forward angular regions ($1.4 < |\eta| < 2.5$), where there is no solenoid coverage and partial tracker coverage, the lead is placed between the first and second layers of the pre-shower detectors. The first layer is then used to locate individual particles and the layers after the lead are used to identify showers.

The scintillating material is arranged in small interlocking wedges in each layer. In the central region, the pre-shower has a cylindrical design, with the wedges of scintillator extending over its full length of 280 cm. The forward pre-shower detectors are circular in design, being subdivided into octants.

The scintillation light is collected in wavelength shifting light guides embedded in the scintillator wedges. Then, as for the CFT, the light is transmitted to VLPCs located below the DØ calorimeter. The pre-shower detectors are discussed in more detail in [22, 23].

2.6.2 Calorimeter

The DØ calorimeter is designed to measure the total energy of most particles produced in $p\bar{p}$ collisions [24]. The basic unit of the calorimeter is a cell, consisting of layers of absorber, to induce particle showers, and an active layer of liquid argon, which is ionised by the charged particles within the shower. The ionised charge represents a fraction of the energy of the shower and is collected on a copper plate within each cell. The total charge in all the cells along the path of a shower can then be related to the total energy of the incoming particle.

The calorimeter itself is divided into central and forward regions. The central calorimeter lies outside the central pre-shower detector, extending from a radius of 72 cm to 220 cm. The forward, 'end-cap' calorimeters lie beyond the forward pre-shower detectors in z and extend to $z = \pm 400$ cm. They have an inner radius of 3 cm and an outer radius of 220 cm.

Both the central and end-cap calorimeters are divided into three layers. In increasing distance from the interaction region, these are the *electromagnetic*, *fine hadronic* and *coarse hadronic*. The cells in all three layers are arranged in 'towers' of η and ϕ, as shown in figure 2.6.

The position resolution is determined by the size of the cells in each layer, which cover a region of 0.1×0.1 in η and ϕ. The third layer of the electromagnetic calorime-

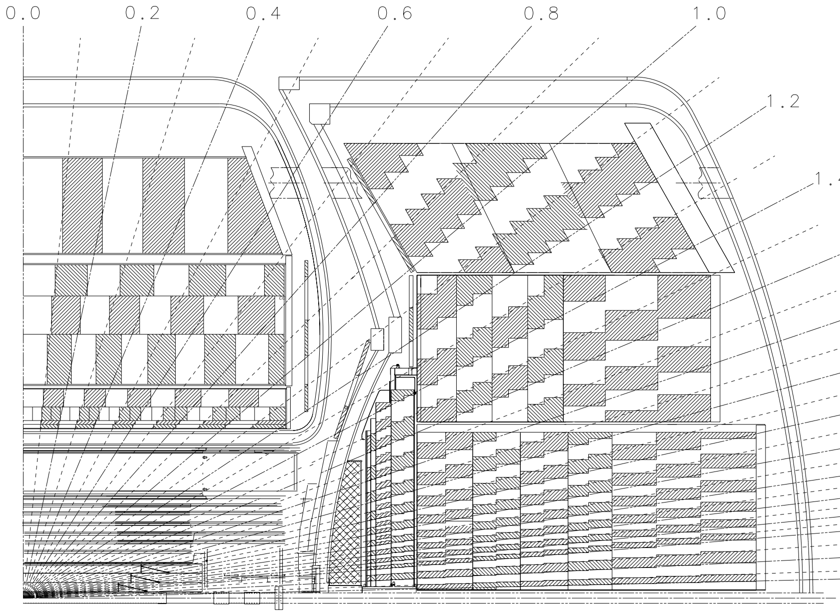

Figure 2.6: A cross section of one quarter of the DØ calorimeter. The longitudinal and η segmentation of the cells is visible.

ter is more finely segmented at 0.05×0.05 to give improved resolution for electromagnetic showers. The electromagnetic calorimeter is four cells deep, with the absorber in each cell being a plate of uranium 3-4 mm thick. The total thickness of the electromagnetic calorimeter corresponds to approximately 20 radiation lengths, so most electromagnetic showers are contained within these layers. The fine segmentation of the cells also gives excellent longitudinal and transverse shower shape resolution, allowing improved particle identification.

Hadronic showers develop over longer distances and will extend into the fine and coarse hadronic layers. In the fine hadronic layer, the cells are larger and hold thicker (6 mm) uranium plates. The cell segmentation is again 0.1×0.1 in η and ϕ and the layer is 3 cells deep, corresponding to approximately 2.2 nuclear interaction lengths. This allows the measurement of any electromagnetic shower which penetrates through the electromagnetic layer and covers the region where hadronic showers deposit most of their energy. The coarse hadronic layer holds larger cells again, with thick (46.5 mm) copper or stainless steel absorber plates, corresponding to a further 5-7 nuclear interaction lengths.

The expected energy resolution of the calorimeter is $\sigma(E)/E = 15\%/\sqrt{E} + 0.4\%$ for electrons and $\sigma(E)/E = 80\%/\sqrt{E}$ for jets (E / GeV)[24].

2.7 Muon Detectors

High energy muons lose energy primarily through ionisation. As a result, they pass through all of the inner detectors and calorimeter at DØ, losing only around 2.5 GeV. Thus to detect muons, a second tracking system is located outside the calorimeter. This has three layers of detectors giving position measurements, with a toroid magnet giving a 1.8 T field located between the first and second layer, allowing a measurement of momentum.

Position measurements in the muon detectors are provided by drift chambers. These collect charge ionised in a gas by the passage of a charged particle. The gas is held in a sealed volume, with the charge collected on high voltage sense wires running through this volume. The chambers are arranged in planes, giving the muon detectors a cuboid rather than cylindrical geometry. Four planes make up the *central* muon system, surrounding the calorimeter and providing coverage up to $|\eta| < 1$. There is a gap in the bottom of the central region, where the support structure for the calorimeter is located. Two further planes of detectors are located at either end of the calorimeter in z, making up the *forward* muon system. These extend the detector coverage out to $|\eta| < 2.2$.

The drift chambers provide an accurate (to within 0.5 mm) measurement of the co-ordinate perpendicular to the sense wires (corresponding to η). This has been chosen to match the bending direction in the toroid field.

The muon detectors also have layers of scintillating material arranged in pixels. These provide the best measurement of the other co-ordinate (corresponding to ϕ). The size of the pixels varies, but each pixel covers a region in ϕ corresponding to

4.5°.

The muon detectors are discussed in more detail in Chapter 5 and [25, 26, 27].

2.7.1 Momentum Resolution

For comparison with the central tracking system (see section 2.5.3), the momentum resolution of the muon system can be parameterised as [25]:

$$\frac{\sigma_{1/p}}{1/p} \;=\; 0.18 \;+\; 0.005p. \tag{2.8}$$

with p measured in GeV.

For the regions with CFT coverage, the central tracking detectors provide a much better measurement of momentum. However in the forward region, with only SMT coverage, the muon system measurement is comparable in resolution.

2.8 DØ Trigger System

The rate of p$\bar{\text{p}}$ collisions at the Tevatron is significantly higher that the rate at which events can be read out and stored for offline analysis. So, one of the major challenges involved in running an experiment such as DØ is to select which collisions to store.

To do this, *event triggers* are used. DØ uses a three tier trigger system, with each tier rejecting some events and passing others. The event selection is based on identifying physics objects (such as particles or tracks), with each level of the trigger system applying more detailed criteria. The overall aim of the trigger system is to accept events at the rate of collisions (2.5 MHz at the time of writing, to be increased to 7.6 MHz later in Run II) and output events at the rate they can be written to storage tapes (around 50 Hz). The three trigger levels are described briefly in sections 2.8.1 to 2.8.3.

2.8.1 Level 1 Trigger

The first trigger level is based on specialised fast readout, which gives approximate measurements to make a decision on each bunch crossing. All detector systems other than the silicon tracker provide some information for the Level 1 trigger [28].

The fibre tracker uses axial fibres in 4.5° wedges to give a track trigger [29]. Hit fibres within each wedge are matched to pre-defined hit maps, which contain track definitions with different curvatures. The hit maps allow an approximate momentum measurement in the following bins: 1.5 – 3 GeV, 3–5 GeV, 5–10 GeV and $>$ 10 GeV. For the data used in this thesis, the Level 1 fibre tracker trigger was not operational.

The calorimeter trigger for electrons, photons and hadrons is based on an approximate energy measurement from a tower of cells in η and ϕ [30]. The transverse energy in each tower can be determined to within four ranges: 3 – 5 GeV, 5–7 GeV, 7–10 GeV and $>$ 10 GeV.

At the time of writing, the Level 1 muon trigger was based on the scintillating pixels only, requiring co-incidence of hits in two layers [25, 27].

There is also a *minimum bias* or *fast-z* inelastic collision trigger [28], based on the coincidence of hits in the luminosity monitors, with no requirement on any other sub-detector trigger (fast-z refers to the approximate z measurement of the collision from the relative hit times). The fast-z trigger can be run stand-alone, but is typically used in combination with another trigger, such as the muon trigger, to reduce non-collision backgrounds.

Level 1 triggers can also be built from combinations of different sub-detector triggers, such as a muon+jet trigger. When the data used in this thesis was recorded, the event rate out of Level 1 was around 100 Hz. The design for Level 1 is to pass events to Level 2 at 5 kHz.

2.8.2 Level 2 Trigger

The Level 2 trigger also uses specialised fast readout, combining information from all detector components at improved resolutions [31]. The silicon and fibre tracking detectors provide triggers for particle tracks with different momentum requirements [29, 32]. The pre-shower and calorimeter triggers refine the energy measurement from Level 1 [33] and the muon system uses information from both the scintillators and drift chambers, allowing an approximate momentum determination [34]. However, for the data used in this thesis, no Level 2 trigger was operational. As a result, events were passed from Level 1 directly to Level 3. The aim for Level 2 is to pass events to Level 3 at 1 kHz.

2.8.3 Level 3 Trigger

The Level 3 trigger is software based, with a farm of processors carrying out partial event reconstruction [35]. Unlike the previous trigger levels, Level 3 uses the full precision readout of the detector.

The Level 3 event reconstruction is steered by the Level 1 and Level 2 triggers passed by the event. For example, if an event passes a Level 2 electron trigger, information from the calorimeter will be reconstructed in Level 3. The software reconstruction allows more rigorous requirements to select events. Events passing Level 3 are written to storage tapes for full offline event reconstruction.

For the data used in this thesis, Level 3 was operating in a limited capacity. No muon triggers were operational, so events passing Level 1 muon triggers were written directly to the storage tapes. In total, Level 3 was passing events at a rate of around 30 Hz. At the time of writing, this has been increased to the design rate of 50 Hz.

2.9 Offline Event Reconstruction

Events written to the storage tapes are later processed on a dedicated computer farm. This farm runs the event reconstruction code for all the detector components and outputs the data in a physics oriented format.

Particle tracking and muon reconstruction form the foundations to the work described in Chapters 4 and 5 respectively, so are described in some detail in there.

Vertex reconstruction is based on particle tracks reconstructed in the SMT, the detector component closest to the beam [36]. Tracks are extrapolated back toward the beam, with any point of overlap (within errors) forming a potential vertex. A momentum-weighted sum of the tracks meeting at a vertex is used to select the primary (collision) vertex. Remaining vertexes are stored as potential candidates for the decay points of long lived particles. If no primary vertex is reconstructed, a default position of (0,0,0) is taken.

Reconstruction of showers in the calorimeter is based on 'clusters' of neighbouring cells containing energy deposits. Starting from a cluster, a cone is defined in $\eta - \phi$, with an opening angle of 0.5 originating at the primary vertex. The total energy within the cone is summed, with the fraction in the electromagnetic and hadronic layers used to separate electromagnetic and hadronic showers.

The energy distribution in the calorimeter is also used to identify missing transverse energy in events, the signal for neutrino production. This missing transverse energy must also be corrected for the presence of any muons in the event, as muons deposit only a fraction of their energy in the calorimeter.

2.9.1 Simulated Data

Simulation of events (also known as 'Monte Carlo' simulation) and the detector response to those events is crucial to any physics measurement.

The generation of simulated data is carried out in three stages. First, the $p\bar{p}$ collision is simulated, and short lived particles are allowed to decay. This stage is typically handled by an event generator, such as Pythia [37] or Herwig [38]. It is possible to require specific processes in this collision, such as Z^0 production, or more specifically Z^0 decay to muons. It is also possible to produce more artificial situations, such as producing single particles without an associated $p\bar{p}$ collision.

The next stage is to hadronise any quarks and gluons produced. Hadronisation can also be handled by many event generations (including Pythia and Herwig), but it is also possible to generate the events with one package and carry out the hadronisation with another.

Then, the particles produced by the previous stage are passed through a model of the DØ detector. For this stage, the GEANT package is used, which calculates the effects on the particles of the magnetic fields and material in DØ, producing ionisation and showers where appropriate [39].

Finally, the expected response of the various DØ detectors to these particles is simulated. The output of this stage is digitised data, as is produced by the real detector during a collision. Then the standard event reconstruction, as used for real data, can be run on the simulated data.

DØ also has a ‘fast’ event simulator, PMCS (Parameterised Monte Carlo Simulation) [40]. Rather than simulating the response of the detector to a generated event and then running the full event reconstruction, PMCS simply ‘smears’ the various physics objects (tracks, electrons/photons, jets, missing transverse energy and muons) to match the resolution seen in data. PMCS has been tuned to match the data used in this thesis and is used in the analysis described in Chapter 6.

Chapter 3

The DØ Silicon Microstrip Tracker (SMT)

An important part of the DØ upgrade for Run II has been the installation of the silicon microstrip tracking detector (SMT), part of the central tracking system (see section 2.5). The SMT surrounds the beam pipe in the centre of DØ and provides high resolution position measurements for charged particles, significantly improving both the momentum resolution and vertexing capabilities of DØ.

This chapter provides an overview of the design and operation of the SMT, with particular emphasis on the on-line monitoring of data quality. A brief description of the construction and readout systems is given in sections 3.1 and 3.2. This is followed by an overview of the data structure from the SMT in section 3.3. Finally, the two packages developed to carry out this monitoring are described. These are a histogramming package, covered in section 3.5, and a graphical event display covered in section 3.6. A fuller description of all aspects of the SMT can be found in [19].

3.1 SMT Design

The sensitive devices in the SMT are wafers of n-type silicon 300 μm thick. Position measurements are made by collecting the electron-hole pairs produced in these wafers by the passage of charged particles. This ionised charge is collected on strips of n^+ or p type silicon implanted on the wafer surfaces. The position measurement resolution is then determined by the strip separation, or *pitch*. However, the optimum resolution is only achieved for particles travelling perpendicularly to the wafers, when the ionisation is localised to the smallest area. The layout of the silicon detector was chosen to achieve the best resolution for particles in all regions.

Two other factors affected the choice of design for the DØ silicon detector. First, many of the physics aims for Run II require the reconstruction of the paths of particles over a wide range in pseudo-rapidity, η. Second, the interaction region at DØ is centred at $z = 0$, but has a Gaussian distribution with a spread of around 25 cm. To achieve the best resolution for particles in all regions, a mixed barrel and disk design was chosen, as shown in figure 3.1.

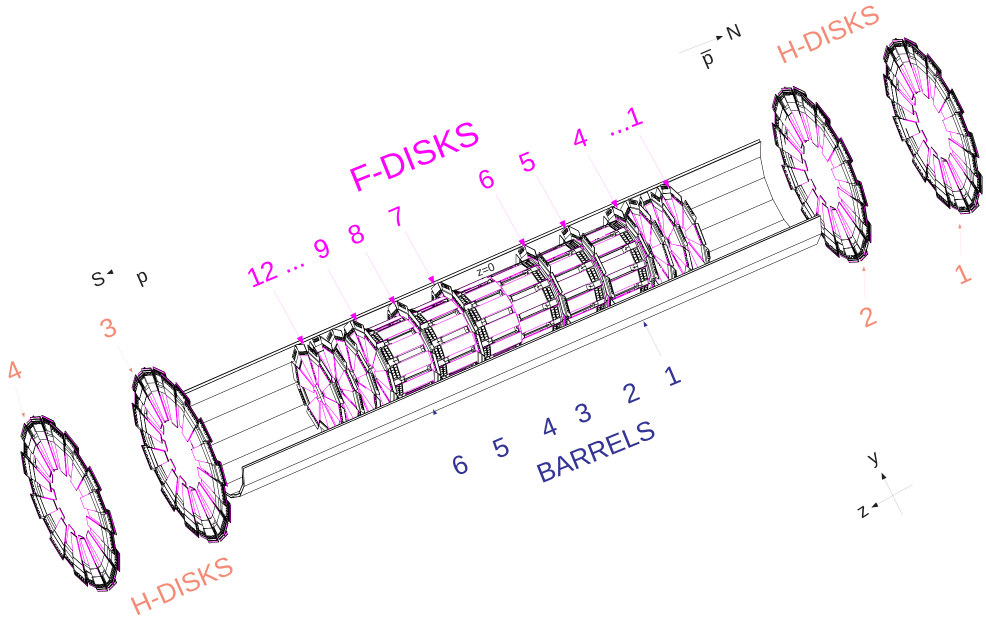

Figure 3.1: The DØ SMT detector, showing the mixed barrel and disk design and the carbon fibre support cylinder.

Six 12 cm long barrels, holding wafers parallel to the beam direction, give the best resolution for tracks at low η. Disks of silicon perpendicular to the beam direction give better resolution for particles at large η. The inclusion of larger disks at each end significantly improves the tracking performance for $|\eta| > 3$ (as shown in figure 2.5). The SMT has a total of over 792,000 readout strips, with over 387,000 in the barrels and 405,000 in the disks.

3.1.1 Silicon Barrels

The basic unit in the barrels is the *ladder*, holding a silicon wafer extending 12 cm in z, with SVXIIe readout chips (described in section 3.2.1) located at one end. The wafers hold strip implants in multiples of 128, the number of readout channels on each SVXIIe chip. A more technical review of the ladders is given in [41].

The barrels consist of four super-layers, each consisting of two sub-layers of ladders, offset in ϕ to provide 2π coverage (see figure 3.2). There are 12 ladders in each of the inner two super-layers, with the first sub-layer lying at a mean radius of 2.5 cm around the beam. The outer two super-layers hold 24 ladders, with the outermost sub-layer at a mean radius of 12 cm.

All silicon wafers in the barrel assemblies have p-type strip implants lying parallel to the beam direction (*axial* strips), allowing measurement of the r-ϕ co-ordinates. These axial strips have a pitch of 50 μm.

In super-layers one and three, each wafer is approximately 1.9 cm wide, holding 384 axial strips. In the four central barrels, the other side of these wafers is implanted with 768 n^+ type strips lying perpendicular to the beam direction (*stereo* strips), giving measurements of the r-z co-ordinates. These stereo strips have a larger pitch of 156 μm, to cover the entire 12 cm length of the ladder. To reduce the electronics needed on the stereo side, there is joint readout of the n^{th} and $(n + 384)^{th}$ strip, giving a total of 384 readout channels.

In super-layers two and four of all barrels, larger wafers approximately 3.2 cm wide hold 640 axial strips. The other side of these wafers is implanted with 512 n^+ type strips at a pitch of 62.5 μm. These stereo strips lie at an angle of 2° to

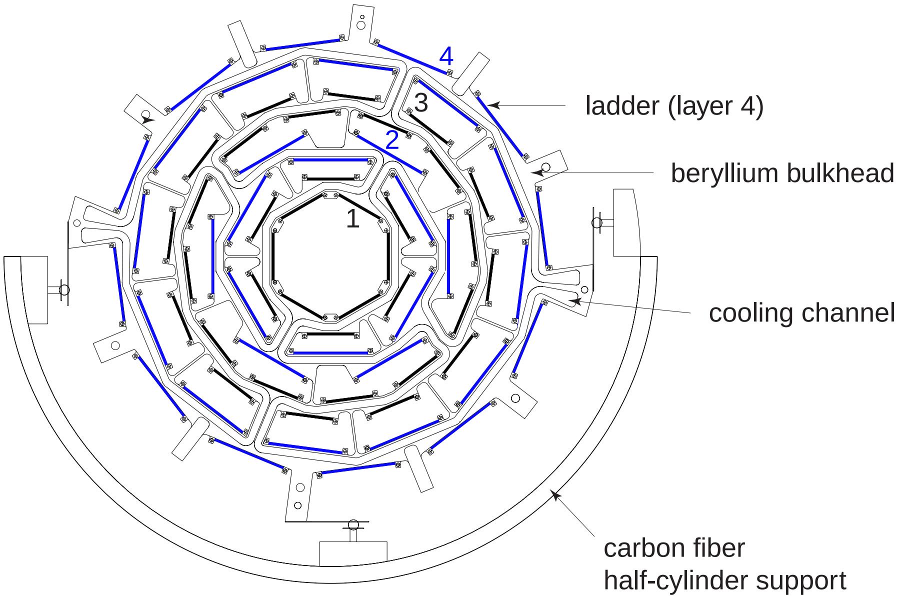

Figure 3.2: An x-y view of a silicon barrel. The super-layers are numbered and the beryllium bulkhead and support structure are also shown.

the axial strips to provide information on the r-z co-ordinates. The use of these 2° wafers was motivated by the prohibitive cost of the 90° design.

The ladders themselves are supported on carbon fibre rods, with barrel assemblies held together by bulkheads of beryllium, chosen for its rigidity and large radiation length, to minimise scattering of charged particles. The bulkheads also carry the coolant water to control the temperature in the SMT.

3.1.2 Silicon Disks

Associated with each barrel is an *F-disk* assembly, shown in figure 3.3. These disks are made from 12 *wedges* of a similar basic design to the ladders, holding a silicon wafer and readout electronics.

Each wedge holds 1024 p-type strip implants at a pitch of 52 μm. These strips lie parallel to one edge of the tapered silicon wafer. The other side of these wafers is implanted with 768 n^+-type strips at a pitch of 65 μm. These strips lie parallel

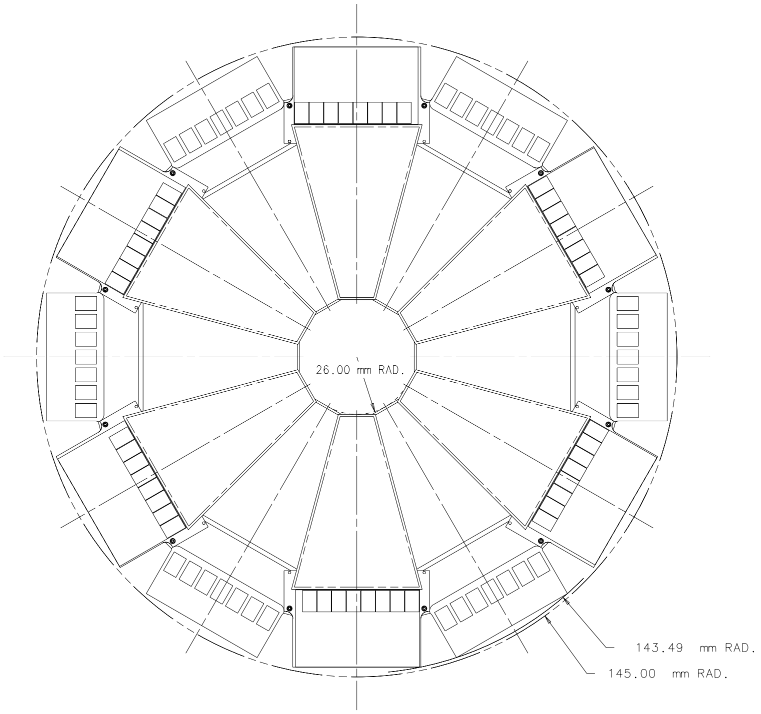

Figure 3.3: An x-y view of an F-disk. Each wedge consists of a double-sided silicon wafer, with the readout electronics located at the outer edge.

to the other edge of the wafer, making an angle of 30° with the strips on the other side. The combination of strips on both sides allows a measurement of r-z and r-ϕ co-ordinates.

Along with the F-disk associated with each barrel, three more are placed after the outer barrel.

Further out in z are the large *H Disks*. These are constructed from two disks of 24 single sided wedges, attached back-to-back. Each wedge has 768 p-type strip implants on one side of the silicon wafer, with a pitch of 80.7 μm. Attaching two disks back-to-back gives an angle of 15° between the strips on overlapping wedges.

Both F and H-disks are supported by beryllium rings. The barrels and disks are mounted in a carbon fibre half cylinder to provide structural support, as illustrated in figure 3.1. The F and H-disks are described in more detail in [42].

3.1.3 SMT Numbering Scheme

To identify specific ladders or wedges within the SMT, a numbering scheme is used [43]. The barrels are numbered 1–6, starting at the North (negative z) end of the SMT. The super(sub)-layers are numbered 1–4(8) with increasing distance from the beam. The ladders in each sub-layer are numbered 1–6 or 1–12, starting at $\phi = 0$ and increasing with ϕ. A ladder can then be identified by the barrel, sub-layer and ladder number.

F-disks are numbered 1–12, again starting from the North end of the SMT. Wedges are numbered 1–12, with the wedge 1 closest to $\phi = 0$. The H-disks follow the same numbering scheme as the F-disks. Individual wedges are then identified by the disk and wedge number.

The sides of the ladders and wedges are also numbered, with side 1 holding the axial strips and side 2 the stereo strips (where present). On each side, the strips are numbered sequentially, starting on the right hand edge (when viewed from above with the readout electronics at the top).

3.2 SMT Readout

To reconstruct the paths of charged particles, the positions of energy depositions are used. These correspond to the positions in the detector of the strip implants ‘hit’ by passing particles.

The required information exists initially as charge collected on the strip implants. This charge is converted to a digital *pulse height* signal by SVXIIe chips (described in section 3.2.1) located on each ladder and wedge. The rest of the hardware readout chain, described in section 3.2.2, collects and orders the information from all the SVXIIe chips (6,192 are used in the SMT).

3.2.1 SVXIIe Chips

The first stage of readout for the SMT is the SVXIIe chip [44]. The SVXIIe chip has 128 input channels, each one wire bonded to a strip on a silicon wafer.

The chips have two main cycles of operation: acquisition and readout, described briefly below. Both are controlled by a digital 'clock' signal operating at different frequencies.

Data Acquisition

> During acquisition mode, the SVXIIe chips operate at a clock speed corresponding to the minimum time between bunch crossings planned for Run II - 132 ns, or 7.58 MHz. During each clock cycle, the charge collected on each strip is sampled by a capacitor. The SVXIIe input channels each hold a pipeline of 32 capacitors, allowing 32 events to be stored at any time. When the Tevatron is operating with a bunch crossing every 396 ns, only every third clock cycle will correspond to a bunch crossing.
>
> The SMT detector is not used in Level 1 trigger decisions, so until a Level 1 trigger passes an event, the SVXIIe chips continue to acquire data without transmitting any information to the rest of the readout chain. The pipeline of capacitors allows 4.2 μs for a Level 1 decision before an event is overwritten.

Data Readout

> Once a Level 1 trigger has fired, the SVXIIe chips switch to readout mode, in which the stored charges from the relevant event are digitised into a 'pulse height' and passed to the rest of the readout framework.
>
> The chips switch to a clock speed of 106 MHz and use an analogue to digital converter (ADC) to digitise the charge. A stepping voltage, increasing once every clock cycle, is compared to the voltage stored on each capacitor. The steps are referred to as 'ADC counts' and the number of counts required to surpass the voltage across a capacitor gives a measurement of the charge. The

> SVXIIe chips have a range of 0-256 and if, after 256 counts, the capacitor still holds a higher charge, a pulse height of 256 is returned.
>
> This range also gives the approximate readout time for the SMT, with 256 steps at a rate of 106 MHz corresponding to approximately 2.4 μs, which is the same as the gap between super-bunches in the Tevatron (see section 2.1). As the SVXIIe chips can store no new events while in readout mode, DØ can effectively read out a maximum of one event per super-bunch crossing. After digitisation, the chips switch back to acquisition mode.

SVXIIe chips are also used to digitise the signals from the VLPCs in the readout of the scintillating fibre tracker and pre-shower. The rest of the readout chain is similar for these detectors.

3.2.2 The SMT Readout Chain

The readout chain for the SMT is described in detail in [19], with a brief overview given here. The SVXIIe chips are connected by cables to interface boards located just outside the DØ calorimeter. The interface boards control the voltages and clock signals for the silicon wafers and SVXIIe chips. However, the connection between the SMT and the rest of DØ is a set of sequencers, located below the calorimeter. These are connected to the trigger framework and pass the Level 1 decisions to the interface boards, which switch clock speeds as appropriate. The sequencers also collect the pulse heights from the SMT and transmit them, via optical fibre links, to twelve readout crates located outside the DØ collision hall.

Signals from the barrels are also passed to six Level 2 processor crates, which look for tracks as part of the Level 2 trigger. Each crate is connected to a wedge of ladders covering a ϕ region of $\pi/3$ in either the $+z$ or $-z$ half of the detector, which form the trigger regions.

If an event passes a Level 2, it goes to the Level 3 processor farm. Here, the information from all the readout crates of each sub-detector system is combined and partially reconstructed. The Level 3 processors pass triggered events to the data acquisition (DAQ) system [45], which sends them to the storage tapes. Copies of events from the DAQ are also passed to a separate output system, the *Data Distributor* [46]. This is used for on-line monitoring purposes.

3.3 SMT Data

At the most basic level, the data from the SMT consist of charge collected on each strip implant, digitised by the SVXIIe chips. However the zero-point, or *pedestal*, of each strip is not at zero ADC counts, but varies from strip to strip with typical values of between 30 and 50 ADC counts. Electronic and thermal noise also produce fluctuations in the pedestal of around 1-2 ADC counts from event to event.

Pedestals must be subtracted from the total signal to measure the charge ionised by passing particles. This 'signal' charge is usually around 20-30 ADC counts.

In a typical collision, of order 1,000 (less than 0.2%) of the strips in the SMT will contain 'signal'. So rather than reading out every strip in the event, only those which are significantly above pedestal are selected. This significantly reduced the event size and processing time and is made possible by the different operating modes of the SVXIIe chips.

3.3.1 SVXIIe Readout Modes

The two main readout modes for the SVXIIe chips are *all readout mode* and *sparse mode* , described below. In both cases, the chips digitise the charges from every strip, but can then handle the pulse heights in different ways.

All Readout Mode

In this mode, the SVXIIe chips pass the pulse heights from all strips on through the readout chain. This is mainly used to measure the pedestal of each strip, but has also been used extensively during the commissioning of the SMT for testing the readout hardware and software.

Sparse Mode

This mode is used during normal data taking. Each SVXIIe chip stores a readout threshold (in ADC counts) and only those pulse heights above this threshold are passed on to the readout chain. This should correspond to strips which hold charge created by the passage of a particle.

However, this charge can be distributed over a number of strips, not all of which may be above the readout threshold. So, there is an extension to sparse mode called *nearest neighbour mode*, in which the two below threshold strips nearest to an above threshold strip are also read out. This mode is currently not used, but may be activated as the SMT performance is more fully understood.

3.3.2 Setting the Readout Thresholds

Before the SMT can be run in sparse mode, the readout thresholds must be set. Each SVXIIe chip uses one threshold for all 128 strips, derived from the average pedestal of those strips.

The thresholds are calculated during special calibration runs [47], typically between stores at the Tevatron (when there is no beam). During such a run, the SVXIIe chips are switched to all readout mode and automatic Level 1 triggers are passed, so every event is read out. Then, rather than following the standard data path, events are collected by processors connected directly to the readout crates. These calculate the mean and standard deviation of the pedestal for each strip and store these values in a database.

Then, to calculate the average pedestal for a chip, the highest and lowest 15% of the pedestals on that chip are ignored and the remaining 70% are averaged. This is to avoid incorrect thresholds caused by a few high or low pedestal strips.

For the data used in this thesis, the thresholds were set at the average chip pedestal + 6 ADC counts (about 3 times the pedestal RMS for a normal strip).

3.3.3 SMT Data Format

Data flowing out of the readout crates are in a packed hexadecimal form, as described in [48]. This consists simply of an ordered list of strip numbers and ADC counts. A header is added to the data identifying each different chip and readout crate as they occur.

For this data to be used by the offline reconstruction it must be unpacked into a format corresponding to the ladders and wedges in the SMT. The unpacking code uses a hardware map, which consists of an ordered list of detector components connected to each readout channel.

Also, the unpacker can access the database containing strip-by-strip average pedestals from the last calibration run and subtract these from the signal of each strip.

After unpacking, the strip signals are in a format representing the physical structure of the detector (barrels and ladders, disks and wedges). After pedestal subtraction during the unpacking stage, these signals should correspond just to the signals created by the passage of charged particles through the detector, as well as noise fluctuations.

3.3.4 Event Reconstruction in the SMT

The first stage of the event reconstruction looks for clusters of strips on each side of the ladders and wedges. This clustering is carried out by a simple algorithm based on two thresholds: an individual strip threshold of 6 ADC counts above pedestal and a total cluster threshold of 12 ADC counts above pedestal [49].

Working along one side of a ladder or wedge, the algorithm looks for pulse heights above the strip threshold. At the first such strip, a cluster is formed. Then, if the next strip is also above threshold, it is added to the cluster. This continues until a below threshold strip is reached, at which point the cluster is finished. If the total pulse height in this cluster is above the cluster threshold, it is kept. Otherwise, it is discarded.

This stage of reconstruction forms one dimensional clusters, containing the position along the relevant ladder or wedge, from a weighted average of the constituent strip positions, and an energy measurement in the form of the total cluster pulse height. Next, the one dimensional clusters on each side of the double sided ladders and wedges are combined to give a two dimensional cluster in the plane of the ladder or wedge. Finally, the clusters are converted to three dimensional hits in global detector co-ordinates using the spatial position of the relevant ladder or wedge. The list of three dimensional clusters is then used in track finding, described in Chapter 4.

3.4 Aims of SMT On-line Monitoring

To meet the physics aims of Run II, DØ needs to record data at a high rate. As a result, even short lived problems with the detector can result in a large amounts of compromised data. So a vital part of running an experiment as large and complicated as DØ is the real time monitoring of all the detector components.

The rest of this chapter describes the on-line data monitoring framework for the SMT. Two packages are used to ensure the SMT is operating as expected, or to isolate problems when they occur. The main package is *SMT-Examine*, a histogramming tool which allows detailed studies over a period of time. SMT-Examine is described in section 3.5, together with the main problems encountered in the SMT. The second package is an on-line event display. This provides an instant graphical picture of the activity in the entire SMT on an event-by-event basis and is described in section 3.6

Both SMT-Examine and the event display are run at all times during data taking.

They collect events from the data distributor (see section 3.2.2) to study the quality of data being passed by the data acquisition system. Other, more basic monitoring is also in place, for example, to monitor the voltages, currents and temperatures on the individual ladders and wedges in the SMT.

The other DØ sub-detectors use a similar on-line monitoring framework, each with an Examine package. In each case, the Examine is designed to monitor specific parameters for each sub-detector system [50].

3.5 SMT-Examine

SMT-Examine collects data from the SMT over a period of several hours, continually updating histograms designed to monitor the main issues encountered during data taking, as well as providing enough information to identify unexpected problems. This section gives an overview of SMT-Examine, with more technical information available from [51].

The operation of the SMT is most transparent in all readout mode, which was used extensively during detector commissioning. Section 3.5.1 describes the most common problems and the all readout mode histograms filled by SMT-Examine to monitor them.

In sparse mode, the same problems must be identified in different ways. The details of how this is achieved are in section 3.5.2.

3.5.1 SMT Monitoring in All Readout Mode

One device has been chosen as an example of the monitoring possible in all readout mode: barrel 2, sub-layer 4, ladder 4 side 1 (ladder 2,4,4,1). This is the axial side of a double sided, 2° ladder, with 640 strips (5 SVXIIe chips). SMT-Examine was run over 476 events to produce the histograms, which are also displayed together for reference at the end of this section. The device chosen shows most of the problems encountered in the SMT and is not typical of ladder performance.

The main problem in the SMT is related to noise, which causes pulse height fluctuations in the strips. Noisy strips can frequently appear over the readout threshold used in sparse mode, even without the passage of a charged particle.

The total noise in the SMT has two components: coherent and random. Random noise affects individual strips and can be caused by problems with the voltage supply or readout electronics associated with that strip. Coherent noise affects groups of strips or, in some cases, all 128 strips associated with individual SVXIIe chips. The cause of coherent noise is not yet fully understood.

If the problem causing the noise cannot be solved, noisy strips must be identified and ignored during readout in sparse mode.

Total Noise

The total noise, both random and coherent, will affect the standard deviation of the pulse height on a strip. In all readout mode, SMT-Examine fills histograms of this standard deviation against strip number for each side of every ladder and wedge. Figure 3.4 shows this histogram for ladder 2,4,4,1.

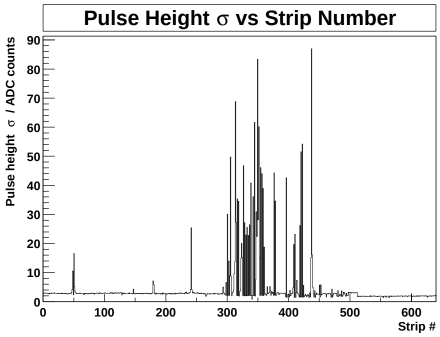

Figure 3.4: A histogram showing the pulse height standard deviation (σ) against strip number for ladder 2,4,4,1. The peaks represent noisy strips.

The standard deviation for a normal strip is expected to be around 2 ADC counts, coming entirely from random noise. Figure 3.4 shows this level of noise in most strips, but with many peaks representing noisy strips. With the sparse mode readout thresholds typically set at 6 ADC counts above the average pedestal, strips with standard deviations of around 50 ADC counts will appear in many events.

Random Noise

To isolate the random noise contribution to the total noise, the D-noise parameter, D is calculated for each strip. D-noise is defined by:

$$\text{D–noise}_{\text{strip n}} = \text{pulse height}_{\text{strip n}} - \text{pulse height}_{\text{strip n+1}}. \tag{3.1}$$

Taking the pulse height difference between neighbouring strips, the coherent noise contribution to total noise cancels from the D-noise. Histograms of the average value and standard deviation of D-noise against strip number are filled for each side of every ladder and wedge. Examples are shown in figure 3.5 for ladder 2,4,4,1.

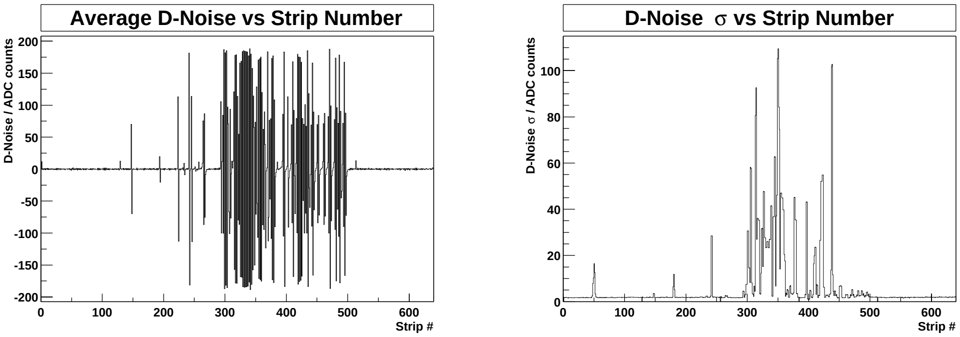

(a) (b)

Figure 3.5: Histograms showing (a) the average D-noise and (b) the D-noise standard deviation (σ) against strip number for ladder 2,4,4,1.

The D-noise standard deviation distribution in figure 3.5 shows significant random noise in the same strips showing the total noise in figure 3.4, suggesting the total noise is dominated by the random component.

However, the distribution of average D-noise suggests other problems as well. Peaks at strip numbers 128, 256, 384 and 512 indicate a feature seen on most devices. The first strip connected to each SVXIIe chip tends to have a pedestal around 10-50 ADC counts lower than every other strip, resulting in a constantly large D-noise value. While the reason for this is not understood, it results in a small inefficiency during readout in sparse mode. As a common readout threshold is set for each chip, this first strip lies well below the threshold and is unlikely to be readout even when hit by a passing particle. This may be solved by operating the chips in nearest neighbour mode (see section 3.3.1), when the strip would automatically be readout if its neighbour is also above threshold.

Coherent Noise

Coherent noise causes event-by-event jumps in the pedestals of groups of strips. While this is more difficult to isolate than random noise, it is apparent in the pulse height distribution for strips associated with each chip. SMT-Examine fills cumulative pulse height histograms for each SVXIIe chip, with one entry for each strip in each event. Figure 3.6 shows examples of this histogram, from ladder 2,4,4,1. Two chips are shown: chip 1, which is connected to strips 1-128; and chip 3 (strips 257-384).

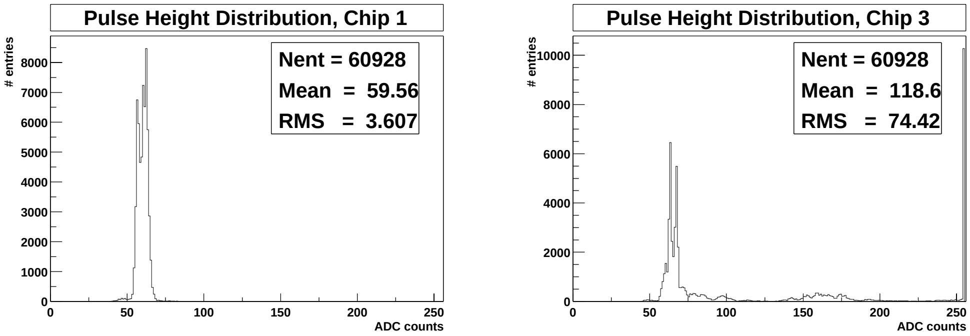

(a) (b)

Figure 3.6: Histograms showing the pulse height distribution for (a) chip 1 and (b) chip 3 on ladder 2,4,4,1. Chip 1 shows some evidence of coherent noise, while chip 3 has several problems.

For a normal chip a single peak is visible, representing the average pedestal and total noise distributions. For a chip suffering coherent noise, entries at a different value will be visible. If the coherent noise causes regular pedestal jumps of a similar size, a second peak will be apparent on the pulse height distribution histogram.

There is some evidence of this behaviour in chip 1 in figure 3.6(a), with peaks at 55 and 60 ADC counts. Chip 3 is reading out many noisy strips between strip numbers 257 and 384 (see the D-noise distributions in figure 3.5), so the pulse height distribution is rather messy. The peak at 256 ADC counts suggests the presence of dead strips, the other main problem in the SMT.

Dead Strips

Dead strips do not respond to the passage of particles and generally remain at a fixed pulse height, sometimes at the maximum of 256 ADC counts. This is usually caused by faulty electronics or a problem in the connection between the strip and SVXIIe chip. Such dead strips need to be identified and ignored during readout in sparse mode.

Strips with high pedestal can easily be identified on histograms of the average pulse height against strip number. SMT-Examine fills these histograms for each side of every ladder and wedge, with an example shown in figure 3.7, again for ladder 2,4,4,1.

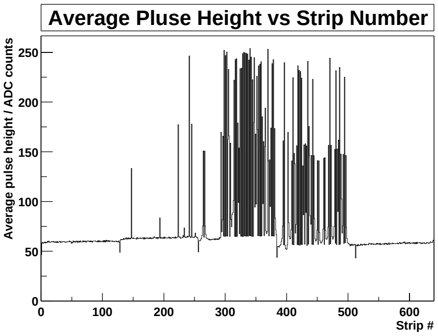

Figure 3.7: The average pulse height against strip number for ladder 2,4,4,1.

Here it is also possible to see the low pedestal of the first strip connected to each chip. Chips 3 and 4 can be seen to have significant problems.

All Readout Mode Histograms

For convenience and to allow easier cross referencing, the histograms shown in this section are displayed together in figure 3.8.

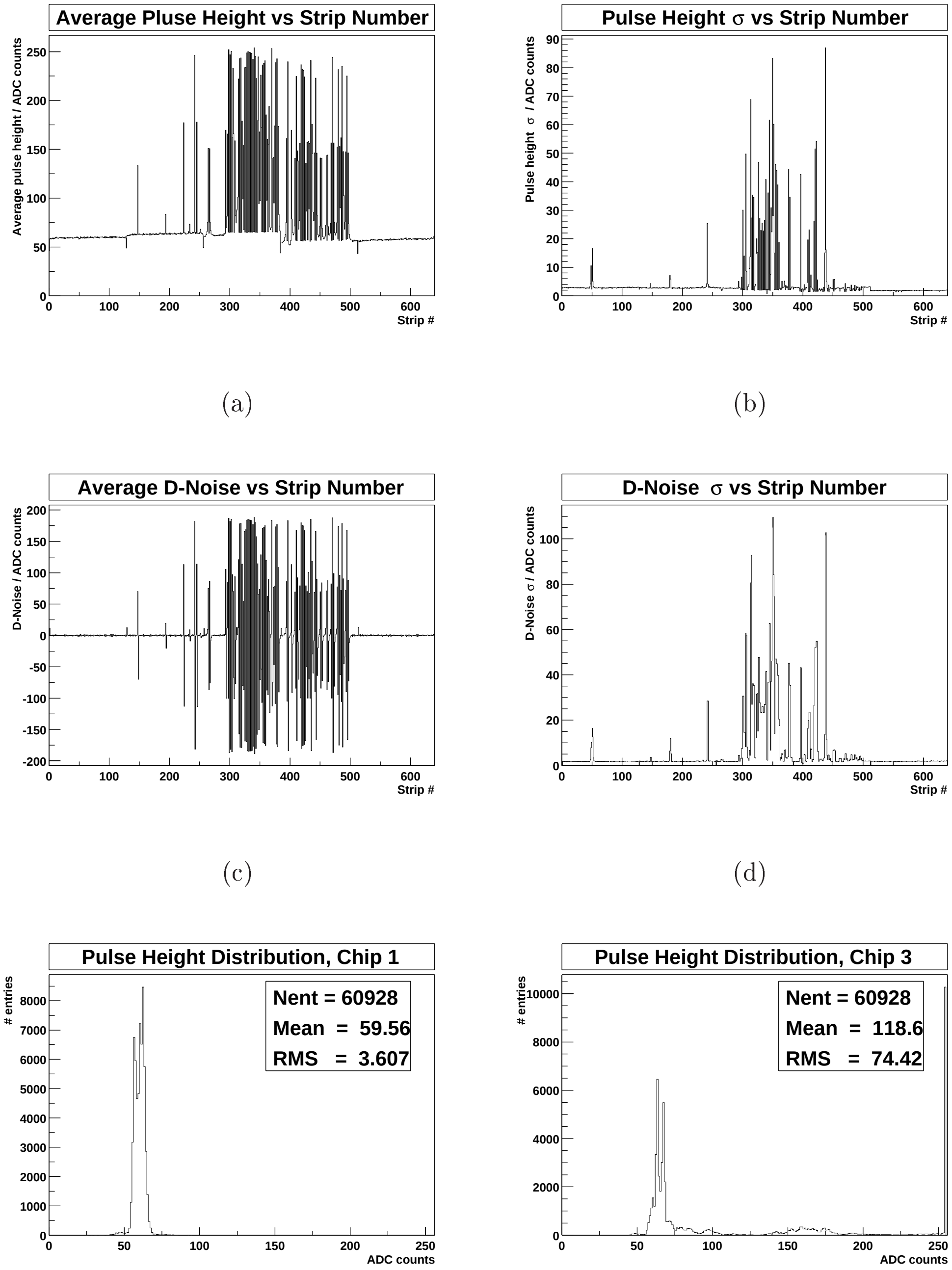

(a) (b)

(c) (d)

(e) (f)

Figure 3.8: The combined all readout mode histograms for ladder 2,4,4,1.

3.5.2 SMT Monitoring in Sparse Mode

When the SMT is operating in sparse mode, it is no longer possible to monitor D-noise, average or standard deviation of the pulse height for each strip. So, different histograms must be used to identify the problems isolated in the previous section.

To illustrate the monitoring possible in sparse mode, example histograms are shown for one device: barrel 6, sub-layer 4, ladder 6, side 2 (ladder 6,4,6,2). This is the stereo side of a 2° ladder, with 512 strips and 4 SVXIIe chips. Histograms are shown for 400 events from a run during which this ladder performed as expected, and 500 events from a run in which this ladder suffered some noise problems.

Total Noise and Dead Strips

It is possible to identify noisy strips from the frequency with which they appear in the sparse mode readout. This depends on the standard deviation of the pulse height fluctuations in the strip, and so the total noise.

SMT-Examine fills histograms of the number of times a strip has been read out against strip number for each side of every ladder and wedge to allow noisy strips to be identified. Examples are shown in figure 3.9.

For a device without noisy strips, this histogram should have a flat distribution. Random hits from particles spread evenly over a device will lead to every strip being over threshold approximately the same number of times. Noisy strips will appear as spikes, as they fluctuate over threshold unnaturally many times. Similarly, dead strips with constant pedestal above the threshold will appear in many events and so also be visible on this histogram.

In figure 3.9(a), three noisy strips (numbers 289, 290 and 291) are visible. They are also visible in figure 3.9(b), along with many other noisy strips. Any noisy or dead strips which cannot be recovered (such as strips 289, 290 and 291) will be excluded from the normal readout of the SMT. SMT-Examine has been used to make a full survey of the SMT performance, isolating around 8000 noisy and 3000

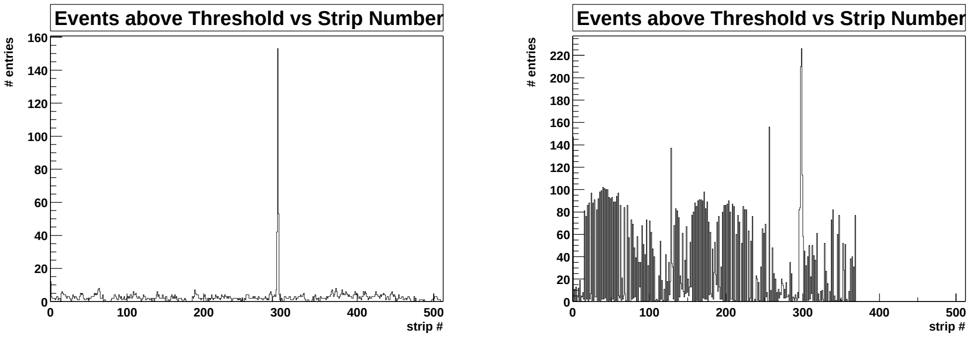

(a)

(b)

Figure 3.9: Histograms showing the number of times each strip has been read out, against strip number for ladder 6,4,6,2. Figure (a) is for 400 events, figure (b) for 500 events from a different run.

dead strips (out of a total of over 792,000), which are now excluded from data taking runs.

Isolating Coherent Noise

Coherent noise can cause groups of strips to jump over the readout threshold without the presence of a particle. This can be monitored on a histogram of the number of strips above threshold in each event, as shown in figure 3.10. SMT-Examine fills such a histogram for each side of every ladder and wedge.

Coherent noise is visible in figure 3.10(b), where around 110 strips have appeared above threshold on several occasions. This problem is not present in the other run, shown in figure 3.10(a). Note that when no strips are above threshold on a device, it does not appear in the event and so the sparse mode histograms are not filled. Thus the zero strips bin in the histograms in figure 3.10 is not filled. Some care must then be applied when interpreting the mean and RMS values.

SMT-Examine also fills histograms of the ‘occupancy’ (percentage of strips on one side of a device above threshold) against event number. Examples are shown in

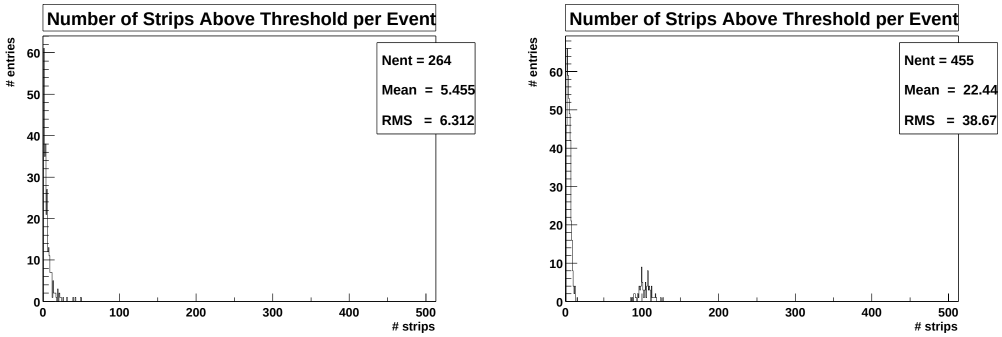

(a)

(b)

Figure 3.10: Histograms showing the number of strips above threshold in each event for ladder 6,4,6,2 for two different runs.

figure 3.11 for ladder 6,4,6,2 from the same two runs.

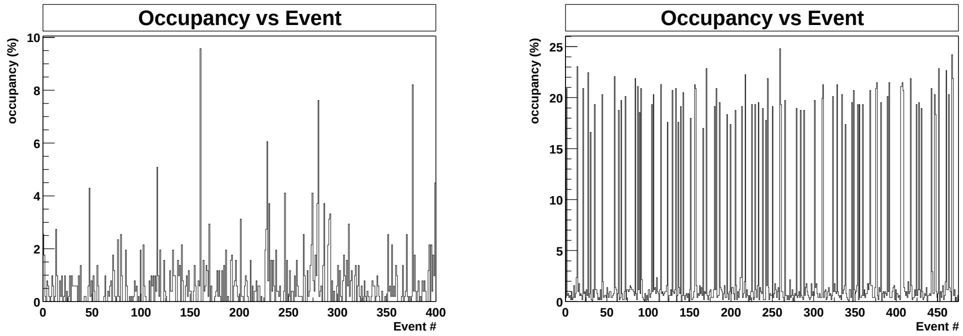

(a)

(b)

Figure 3.11: Histograms showing the occupancy against event number for ladder 6,4,4,2 from two different runs.

In figure 3.11(b), occupancies of around 20% (corresponding to the 110 strips seen in figure 3.10(b)) occur regularly. Again, this suggests a regular coherent noise problem. In the other run, shown in figure 3.11(a), this problem is not seen.

3.5.3 Cluster Monitoring in Sparse Mode

Reconstructed one dimensional clusters contain information on the location and total charge produced by a passing particle. These parameters can be used to check the performance of the readout thresholds and clustering algorithm as well as the noise levels in the SMT.

When running in sparse mode, SMT-Examine fills two types of cluster histogram for each side of every ladder and wedge. Examples are shown for both sides of wedge 3 in F-disk 4. Side 1 holds 1024 strips (8 readout chips), side 2 holds 768 strips (6 readout chips).

Total Cluster Charge

The total charge in a cluster is proportional to the energy lost by a particle when passing through the silicon wafer. This is expected to have a Landau distribution, with most particles losing approximately the same amount of energy, but with a tail to higher values [52]. Examples are shown in figure 3.12.

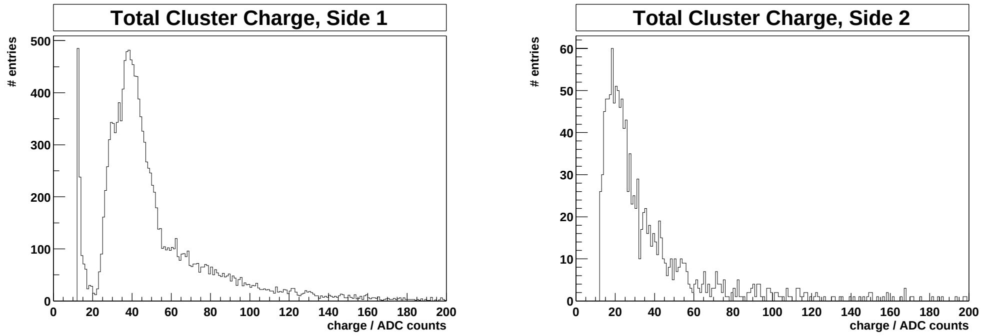

(a)

(b)

Figure 3.12: Histograms showing the total cluster charge for (a) side 1 and (b) side 2 of wedge 3 on F-disk 4.

On side 1 of the wedge the Landau distribution is visible, but there is also a second peak at 12 ADC counts. This is the result of individual noisy strips fluctuating above clustering threshold (12 ADC counts), forming a 'fake' cluster of one strip. This problem does not occur on side 2 of the wedge, where a clean Landau distribution is visible.

As well as noise, the cluster charge histograms can be used to study the efficiency of the readout thresholds. If the Landau distribution is truncated at the lower edge, the thresholds may be too high, leading to the loss of lower energy clusters.

Cluster Position

SMT-Examine also fills histograms of the cluster position in terms of the first strip in a cluster. The number of times a strip forms the start of a cluster is plotted against strip number. This can reveal the location of noisy or dead strips, which may frequently have such high pulse heights that they form a cluster unnaturally many times. Alternatively, a flat distribution indicates the device in question has no problems. Example histograms are shown in figure 3.13.

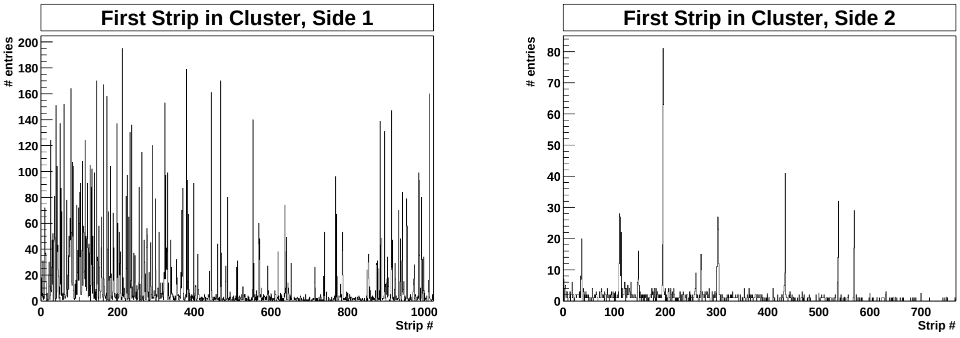

(a) (b)

Figure 3.13: Histograms showing the number of times each strip is the first in a cluster for both sides of wedge 3 on F-disk 4.

These reveal the noise clusters visible on side 1 in figure 3.12 as mostly to be found in the first half of the wedge. Also, it can be seen that side 2 has some noisy strips frequently forming clusters.

This is the only cluster monitoring carried out in SMT-Examine. The later reconstruction stages (3-D clustering and particle tracking) are monitored elsewhere, as part of an overall ‘physics’ Examine package.

3.5.4 Summary Histograms in Sparse Mode

The histograms described in the previous sections represent a huge amount of information, with more than 2,000 histograms produced by the SMT-Examine package. This makes the actual monitoring task difficult and problems may go unnoticed. So, when the SMT is running in sparse mode (the normal mode during data taking), some of the information from the detailed histograms is condensed into twelve summary histograms.

Separately for the barrels, F-disks and H-disks, histograms of the average occupancy (in terms of both strips and clusters) and average cluster size in terms of strips against device number are filled. The device numbering follows from the numbering scheme described in section 3.1.3. The ladders are numbered 1-432, starting with ladder 1 in sub-layer 1 of barrel 1, through to ladder 12 in sub-layer 8 of barrel 6. Similarly, the wedges are numbered from 1 to 144 (96), starting with wedge 1 in F(H) disk 1 through to wedge 12 (24) in F(H) disk 12 (4).

Figure 3.14 shows examples of the average cluster size and number of clusters against ladder number from 500 events.

Bins with zero entries on these histograms indicate ladders that were not operational during this run. At the time of writing, there are 17 ladders with serious problems which are permanently disabled, 11 F-disk wedge sides disabled and 14 H-disk wedge sides disabled. In any run, other devices suffering short term problems may be disabled as well.

The peaks in figure 3.14(a) correspond to the inner sub-layers of the six barrels, where each ladder covers a larger ϕ region, and so has a higher average occupancy, than each ladder in the outermost sub-layer. Also, the ladders in the central two

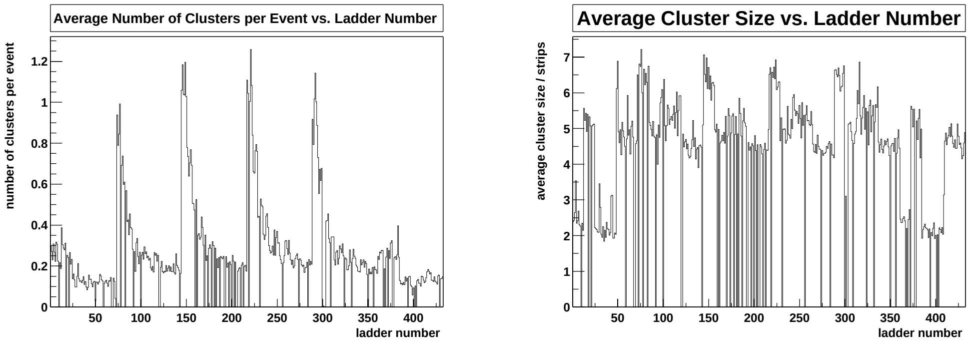

(a) (b)

Figure 3.14: Summary histograms for the SMT barrels, showing (a) the average number of clusters and (b) cluster size against ladder number.

barrels will have a higher average occupancy than the ladders in the outermost two barrels, due to the p$\bar{\text{p}}$ collision point being centred at $z = 0$. The two outer barrels have single sided ladders in the super-layers 1 and 3 (ladders 1-12, 25-48, 361-372 and 385-408), where the occupancy is effectively halved (clusters are detected on only one, instead of both, sides of these ladders).

The average cluster size histogram in figure 3.14(b) shows a slightly different structure. In the outer two barrels, it can be seen that the single sided ladders in super-layers 1 and 3 have an average cluster size of around 2 strips. This is significantly smaller than the clusters in the double sided, 2° ladders in super-layers 2 and 4, which average at around 5 strips.

In the other barrels, the double sided 2° ladders again average at around 5 strips per cluster. However, the double sided, 90° ladders contain on average 6 strips per cluster in super-layer 1 and 5.5 strips per cluster in super-layer 3.

Ladders with unusually large clusters, such as ladder 30, or unusually high occupancies, such as ladder 383, can then be monitored more closely using the detailed histograms.

3.6 Event Display

The SMT-Examine package is generally used for detailed studies of the SMT. The summary histograms described in section 3.5.4 provide an overall picture of the SMT status during a run to aid these studies. To give a more instant picture, a graphical event display is also available.

The idea behind this event display is to draw the strips read out in an individual event on a graphical representation of the detector. The display updates with a new event every 5 seconds, quickly showing noisy regions in the SMT, or regions which are not being read out at all.

There are some technical problems with representing over 792,000 strips in a concise and informative display. As a result, parts of the display are not physically realistic, but are provided for diagnostic purposes. However, where possible it is desirable to give an accurate representation of the SMT. The display itself uses 8 windows, as shown in figure 3.15. The following sections describe the features of the different window displays. A more detailed description of the design and operation of the event display can be found in [53].

3.6.1 Barrel Display

The six barrels are each represented in an x-y view, as shown in figures 3.16 and 3.17, which can be compared with figure 3.2.

Ladders are shown end on, represented by black or yellow lines. The different colours represent different readout crates, which also correspond to the Level 2 silicon track trigger regions. Crate reference numbers are given around the edge of the display, making it easy to identify a crate which is absent from one or several events.

Active strips are represented as lines extending from the ladders, with the length of the line representing the pulse height. Axial strips are shown in red extending

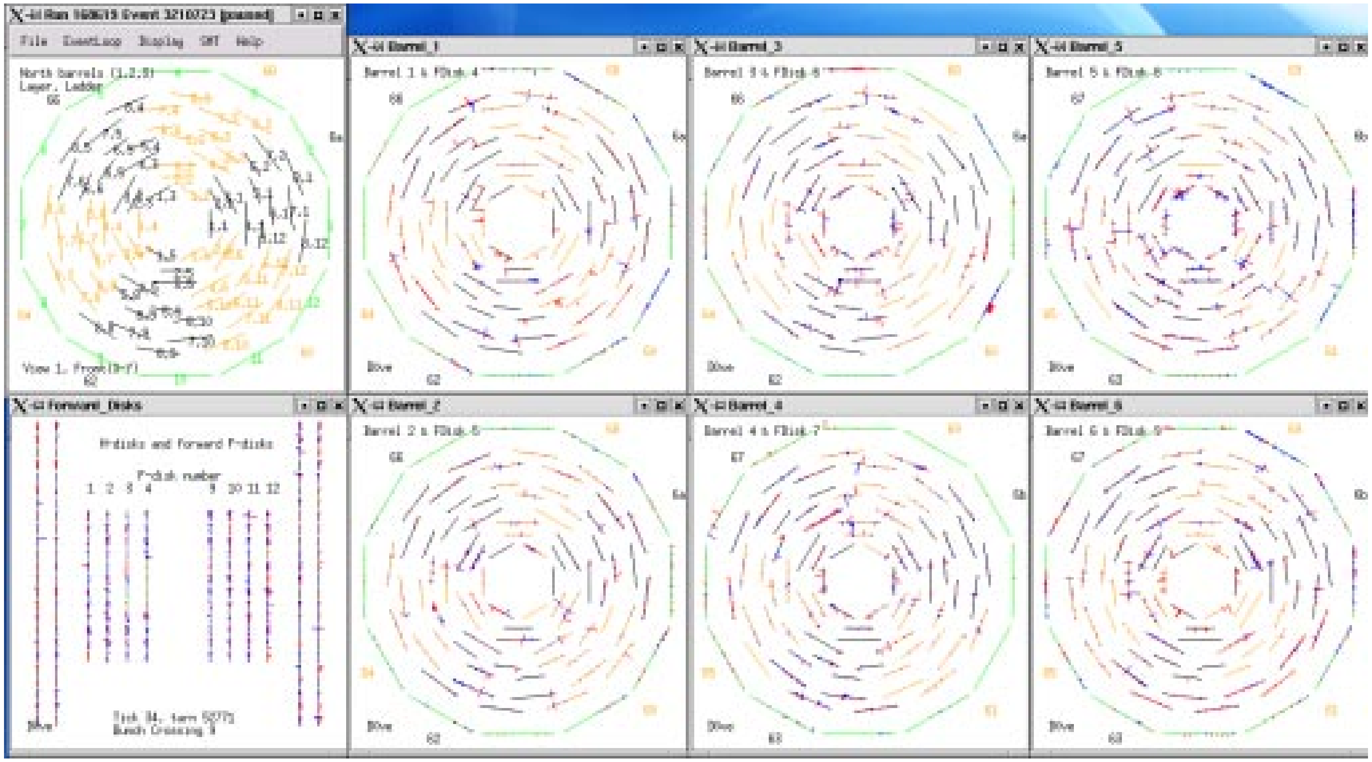

Figure 3.15: The SMT event display

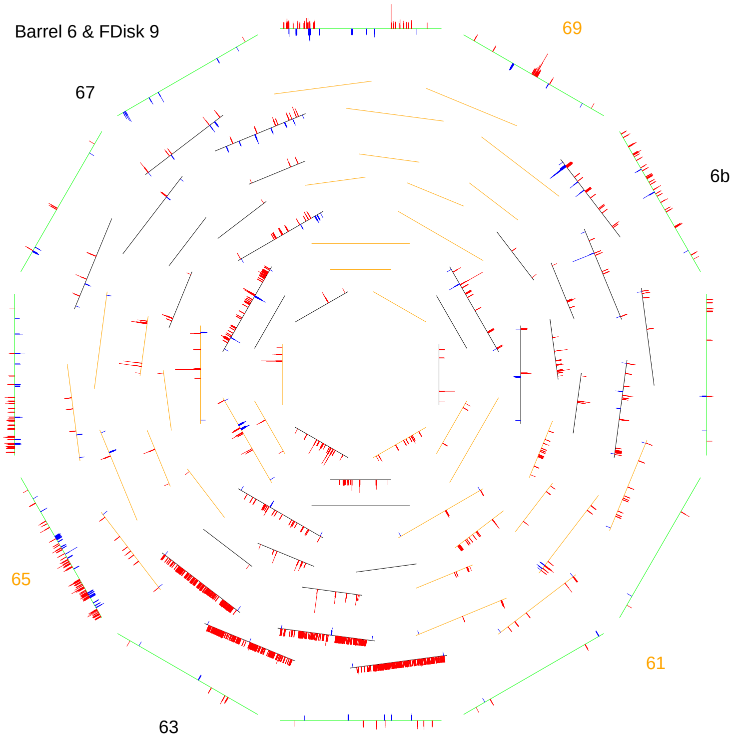

Figure 3.16: An example of a barrel and F-disk display. Here, crate 69 is missing from the event.

away from the centre of the detector. These strips are drawn in a physically accurate manner, so can also reveal the paths of particles through the SMT.

The stereo strips cannot be correctly represented in the x-y plane. Instead, they are displayed at their readout points - the point of connection to the SVXIIe chips at one end of a ladder. In the case of the 2° ladders, this does not represent a significant rotation. However, the 90° strips are shown for diagnostic purposes only and their positions on the display cannot be interpreted as positions along the ladders in the actual detector.

Representing the associated F-disk in this view is also problematic. Rather than showing a physically accurate picture of the disk, the 12 wedges are displayed in green as an extra layer around the outside of the barrel. Again, the active strips are

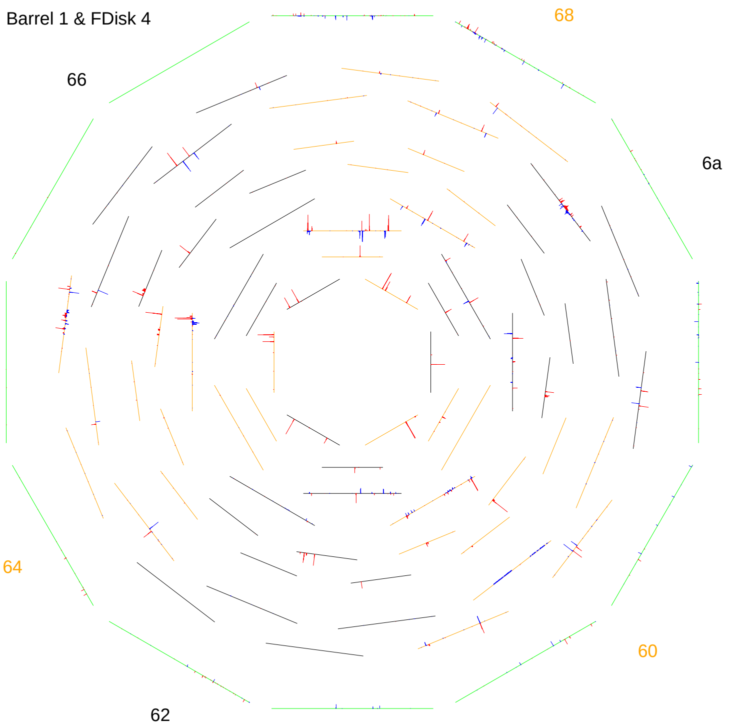

Figure 3.17: Another example of a barrel and F-disk display, with several particle tracks visible.

drawn in red and blue and are shown for diagnostic purposes only.

Figure 3.16 shows an example event in which crate 69 is missing. Four ladders toward the bottom of the display also show signs of coherent noise on side 1, with many axial strips appearing on each ladder.

3.6.2 Disk Display

The remaining forward F and H-disks are represented in a single compact display window. The disks are represented simply as columns of wedges, as shown in figure 3.18.

This provides information for diagnostic purposes rather than physical accuracy.

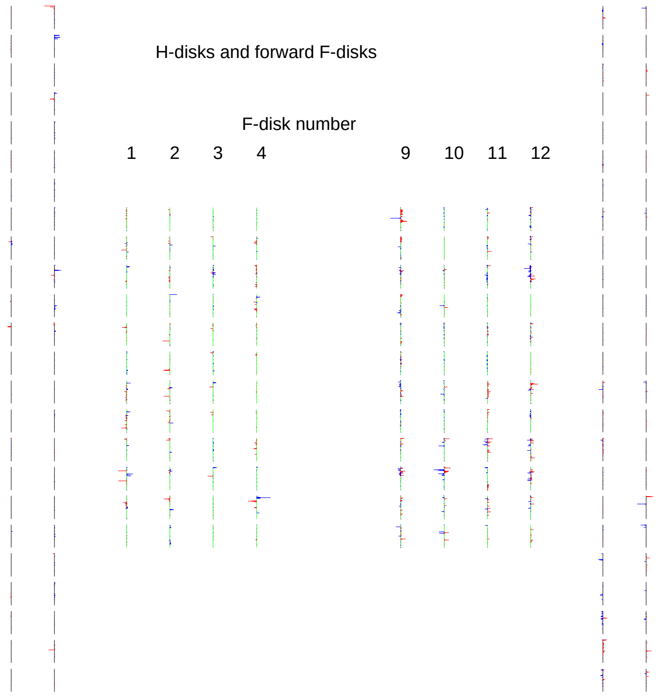

Figure 3.18: The forward F and H-disk event display window.

3.6.3 Additional Features

In addition to the active barrel and disk displays, another window is used to display an empty barrel. This barrel has all ladders numbered, using the numbering scheme described in section 3.1.3, to simplify cross-checking between the event display and SMT-Examine. Alternatively, the empty barrel display can be replaced by a superposition of any or all of the six active barrel displays. In doing so, it becomes easier to follow particle tracks which cross two or more barrels.

It is also possible to control the pedestal subtraction carried out by the data unpacking code (see section 3.3.3). Either the pedestals stored in the database (the default used in event reconstruction) or a constant, user defined pedestal (which can be set to zero) can be used. By setting the pedestal to zero, it is possible to see every strip that has been read out. This is the most useful option for diagnosing problems in the SMT, so is the default option for the event display. As in figure 3.16, noisy regions of the detector are easily visible without pedestal subtraction.

In general, the event display can be used to identify both random and coherent noise, as well as readout crate problems. It can also be used to see the paths of charged particles through the detector to give an idea of the physics performance of the SMT.

Chapter 4

Particle Tracking and Track Extrapolation

The central tracking system at DØ, consisting of the silicon and fibre tracking detectors (as described in section 2.5), provides an accurate measurement of the paths and momenta of charged particles. However, it has limited particle identification capabilities - for example, it is difficult to separate muons from electrons. For this, information from the other detector components, such as the pre-shower, calorimeter and muon system must be combined with tracking information.

In this chapter, a method for combining the information from the different sub-detectors is described. The approach adopted is to start with particle tracks reconstructed in the central tracking system. These tracks are extrapolated to any part of the detector, where they can be associated with information from the other sub-detectors.

At DØ there are several algorithms used to reconstruct particle tracks in the central tracking system. While the track extrapolation can be done with any of these, it is written within the framework of the default algorithm, GTR (Global TRacking) [54]. For this reason a brief description of GTR is useful and forms section 4.1. This also provides the background required for a brief discussion in section 4.1.2 of some of the problems GTR encountered with the data recorded during the commissioning of DØ, which impacts the rest of this thesis. Finally, the track extrapolation is described in the remaining sections of this chapter, with a discussion of the method itself and some results.

4.1 The GTR Track Finding Algorithm

As described in Chapter 2, charged particles can be detected by the ionisation and scintillation resulting from energy loss. In the central tracking detectors, this is used to accurately measure the position of particles as they pass through successive layers of material.

Reconstruction of the signals from each layer of the central tracking detectors yields 'clusters', which contain a position measurement (with an error) and a measurement of the energy deposited by the passing particle. Tracking algorithms use the clusters to reconstruct the trajectory of charged particles.

The basic GTR components needed to carry out this track finding are described below.

- Surfaces

  First of all, GTR builds a model of the tracking detectors using abstract *surfaces*. The specific types of surface needed to describe the DØ detector are cylinders, for the fibre tracker, and x-y and z planes for the silicon detector. Track parameters and errors can be calculated for each surface.

- Paths

  The actual track finding is controlled by *paths*. The paths are an ordered list of the surfaces that a particle coming from a $p\bar{p}$ collision would cross. The first few surfaces are used to build a 'seed' track with approximate parameters and errors.

- Propagators

  To extrapolate the seed tracks between the remaining surfaces, *propagators* are used. A track propagator solves the equation of motion for a track, including the effects of magnetic fields. The propagator also updates the track errors for the effects of multiple scattering and energy lost in any material crossed while reaching the target surface. For this reason, the propagators must hold an accurate model of the actual material in each of the detector regions.

- Fitters

  Once the track reaches a new surface *fitters* attempt to add a new cluster to the track. The fitters combine the track and cluster errors into a *match* χ^2 and reject the cluster if the χ^2 is too high. If the cluster is added to the track, the fitters update the track parameters and errors.

  It is also possible for a track not to find a cluster on a particular surface, because of detector gaps or inefficiencies. GTR can store such missed surfaces and the probability for this miss to occur.

- Filters

  After moving through all the surfaces in a particular path, a number of filters are applied to clean the list of candidate tracks. These filters reject tracks based on the overall χ^2 of their fit and the number of missed surfaces (based on the miss probability). Tracks may also be rejected if they share 4 or more clusters with another track. The decision of which track to keep is based on the fit χ^2 of the two tracks.

The final output of each GTR path is then a list of tracks. These tracks may then be put through another path, representing another part of the detector they may cross. Alternatively, the tracks can be used to build the final list of tracks reconstructed in this event.

The tracks themselves store a list of surfaces used and the track parameters at each surface. Normally six parameters are needed: three position coordinates, two direction parameters and a curvature (rather, $\frac{q}{p_T}$). However, when bound to a surface, one parameter is fixed and a track has five free parameters. The form of the parameters depends on the type of surface. These are shown in figure 4.1 and summarised in table 4.1 for the surfaces used in GTR.

Surface	Cylinder	x-y plane	z plane
Fixed Parameters	radius, r	u, ϕ	z
Position Parameters	ϕ, z	v, z	x, y
Direction Parameters	α, tanλ	dv/du, dz/du	dx/dz, dy/dz
Curvature	q/p_{T}	q/p	q/p

Table 4.1: The track parameters used in GTR.

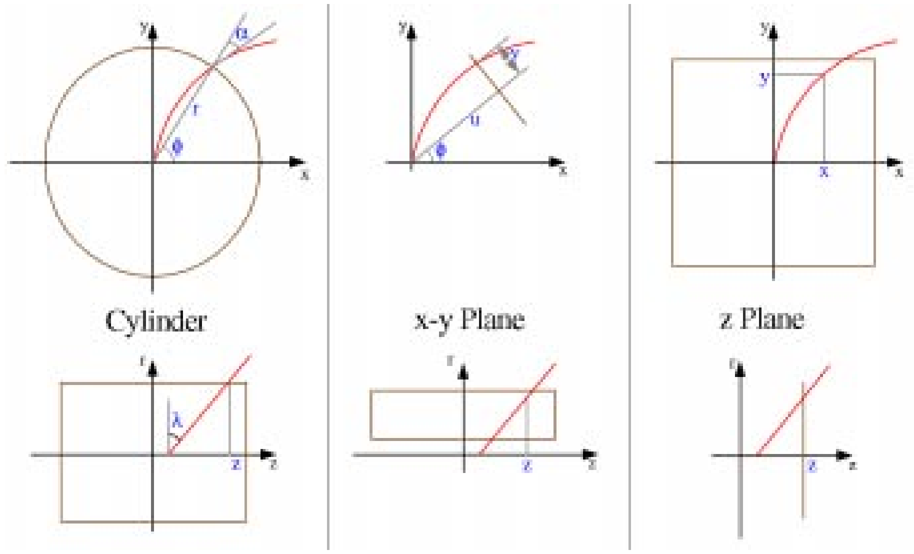

Figure 4.1: The track parameters used in GTR. The track is shown in red, with the surface in brown and track parameters in blue.

Cylindrical surfaces are always defined coaxially with the z axis. The parameter

ϕ is then simply atan(y/x), the position ϕ of the track on the cylinder. The angle α is the track direction in x-y space, defined by $\phi_{position} - \phi_{direction}$. The angle λ is $\pi/2 - \theta$, where θ is the normal polar angle.

An x-y plane is always defined to lie perpendicularly to a radial line in x-y space, a distance u from the origin, with ϕ defining the angle of the radial line. The parameter v is then distance along the plane, which corresponds to y when $\phi = 0$, $-x$ when $\phi = \pi/2$.

For z planes, the normal position coordinates x, y and z are used.

4.1.1 GTR In Practice

By default, GTR uses four different paths, each covering a different angular region illustrated in figure 4.2. These regions are: *central*, covered by the silicon detector and all layers of the fibre tracker; *overlap*, where a particle can cross at least 5 fibre layers; *gap*, which has coverage by less than five fibre layers; and *forward*, which has additional coverage by the forward silicon H-disks.

This section contains a description of track finding in these different regions, with the emphasis on the central. Tracks found in this region are used for the analysis in Chapter 6.

Track Finding in the Central Region

GTR handles this region in three steps: axial fibre tracking; stereo fibre tracking; and silicon extension.

The first step is to build a track in the $r-\phi$ plane from axial fibre clusters. Such a track will have only three parameters, which on a cylindrical surface are ϕ, α and $\frac{q}{p_T}$. Three measurements, required to come from clusters in the outer three fibre layers, are needed to measure these track parameters and associated error matrix. Seed tracks are made from combinations of clusters in these layers, with the requirement that the tracks come from the interaction region and have curvatures corresponding

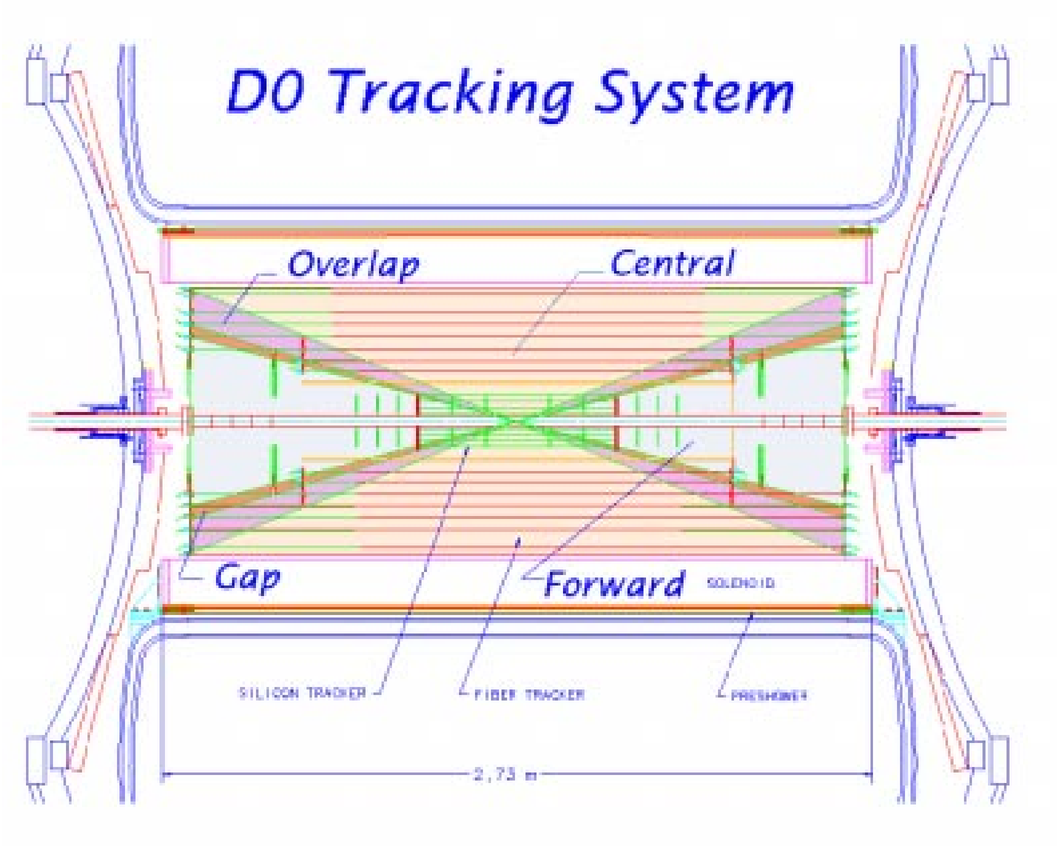

Figure 4.2: The angular regions used in GTR. For each region, a different track finding method is used.

to transverse momenta above 0.4 GeV.

A propagator can now use the track parameters to extrapolate the track through the remaining five axial fibre layers, with fitters adding clusters at each layer. If more than one cluster has a reasonable match χ^2 value, multiple tracks are produced, one for each cluster.

After passing all eight axial fibre layers, the list of tracks is filtered to remove duplicate tracks. The remaining tracks are then passed to the next stage of the path, which looks for clusters in the stereo layers of the fibre tracker.

Two hits are needed to measure the two stereo track parameters (z and $\tan\lambda$). These measurements are required to come from clusters in the outer two stereo fibre layers. Then track finding proceeds as before, with propagators and fitters used to build the tracks, which are filtered after reaching the innermost fibre layer.

The final step then takes the remaining tracks and attempts to add clusters in the silicon detector. Unlike in the fibre tracker, a track is allowed to 'miss' any silicon layer. That is, a track is allowed to pass a silicon wedge or ladder without picking up a cluster. The only requirement is that tracks pick up a total of 4 clusters in the silicon detector.

Track Finding in the Other Regions

Overlap Region

For the overlap region, where there is partial fibre tracker coverage, track finding also begins in the fibre tracker. However, clusters from axial and stereo fibres in each layer are combined to speed up the process. The combined clusters are required to have a z position consistent with a track which exited the edge of the fibre tracker. Tracks can then begin in the fifth, sixth or seventh layers of fibres, but are not allowed to miss any of the other layers.

Gap and Forward Regions

For the gap and forward regions, with partial or no fibre tracker coverage, track finding begins in the silicon barrels and F-Disks. Track finding begins in the outer sub-layers of the barrels and works inward. A section of the F-disks is also included in each step, covering the radial gap between the sub-layers.

As with the silicon extension to the central path, tracks are allowed to 'miss' any ladder or wedge they cross, with the requirement that at least 4 matching clusters are found in total.

For the forward region, candidate tracks are extended to the H-Disks, where they can pick up more clusters. The H-Disks are not currently used in track finding.

GTR Output

The four GTR paths each produce a list of candidate tracks. These are then merged into the final list of tracks for the event.

During the merging, the four lists are checked for duplicate tracks. Again, tracks sharing more than 4 hits are considered to be duplicates. A decision based originally on χ^2 selects the 'best' track (the track with the lowest χ^2). However, this caused some problems in early Run II data (see section 4.1.2), so was modified to take the longest track. If two tracks are the same length, then the track with the lowest χ^2 is preferred. The remaining tracks form the output of GTR and the original track lists from each path are dropped.

4.1.2 Modifications to GTR for Early Run II Data

During the commissioning of DØ at the beginning of Run II the silicon detector was operational before the fibre tracker. So for the early data, the silicon-only track finding intended for use in the gap region was used everywhere.

During the fibre tracker commissioning, the axial layers were read out before the stereo layers (most of the data used in this thesis has few stereo fibres active). The default central path was therefore modified to include tracks made only from axial fibres in the final list of tracks, rather than requiring the stereo fibres and silicon clusters which normally form part of the central path.

To gain a reasonable efficiency for finding tracks with both silicon and fibre clusters, which by default require all axial and stereo layers, another path was introduced. Tracks found in the silicon detector were also extended into the fibre tracker, picking up axial fibre clusters. These tracks were also allowed to miss one axial fibre layer and all stereo fibre layers, giving a significant increase in efficiency for early data.

As the understanding of the performance and alignment of the tracking detectors improves, these alternative paths will be turned off.

So, the final list of tracks in the data for this thesis consists of the following:

- silicon only tracks in all angular regions (at least 4 clusters).
- tracks found in the silicon and extended into the fibre tracker, picking up at least 7 more (axial) clusters.
- 8 cluster axial fibre only tracks.
- 16 cluster axial + stereo fibre tracks.
- axial+stereo fibre tracks extended into the silicon detector, adding at least 4 more clusters.

From the above list, it can be seen that the same track can be found in several ways, starting in either the silicon or fibre tracker. So when building the list of final tracks the filter had to remove these possible duplicates. In the original implementation, the decision was taken based on the χ^2 of the track fit. This means that a short track with few hits may often be taken in preference to a long track with many hits. Thus, a silicon only track would be kept in preference to the equivalent combined silicon and fibre tracker track, which would have significantly better momentum resolution.

For this reason, it was decided to make the 5 track types available to the end user, as well as the less optimal list of final tracks. This filter problem has been fixed for more recent versions of GTR, by taking into account the track length as well as χ^2. However, it limited the track extrapolation studies possible in the data available for this thesis (see section 4.5.5).

4.2 Track Extrapolation

To associate particle tracks with information from other detector subsystems, the approach used in GTR is adopted. The idea, then, is to propagate the tracks to the same surface as, for example, a pre-shower cluster and then see if the track and cluster are consistent (within errors).

Within the GTR framework, new surfaces are defined to describe the DØ detector outside the central tracking region. The existing surface types within GTR are sufficient for the central pre-shower (cylinders), central calorimeter (cylinders) and muon system (x-y and z planes). However, the forward pre-shower detectors, having a curved shape, are more problematic. At the time of writing, a z plane is used as an approximation, but this is inadequate for precision measurements.

Next, new propagators have been developed to extrapolate tracks to these surfaces. While part of the propagators already exists (the solving of the equations of motion and updating the track parameters and error matrix for motion through a magnetic field) a realistic definition of the material in those parts of the detector did not exist. These propagators are described in detail in section 4.3.

Finally, new fitters could be used for the pre-shower and muon systems, to update the tracks for the information from the clusters in these detectors. The default fitters used by GTR are sufficient for this purpose. However, at the time of writing this final step has not yet been implemented. Also, it is not clear that the addition of muon system information gives any improvement to the track momentum resolution. The current status of the track extrapolation code is also summarised in [55].

4.3 Track Propagators

Track propagators have to accurately model the interactions of particles with thick layers of material. In particular, tracks are extrapolated through the solenoid to the pre-shower detectors and through the calorimeter to the muon system. The propagators take into account the effects of energy loss (see section 4.3.1) and multiple scattering (see section 4.3.2). However, the propagators are not intended to model the formation of showers of secondary particles. As such, they cannot accurately predict the passage of most particles through the DØ calorimeter. However, they are of particular use for muons (which generally do not form showers) and can also be used to match most particle tracks to pre-shower clusters.

4.3.1 Energy Loss

As discussed in section 2.3.1, high energy particles generally lose energy at approximately the same rate. As the track propagators are mostly to be used for high energy tracks (for example, a muon requires around 2.5 GeV to penetrate the calorimeter), it is possible to assume all tracks correspond to MIPs. So, rather than reproducing the full Bethe-Bloch equation shown in figure 2.2, the energy loss is modelled by a simple constant term and a small rise with energy. The energy loss correction thus takes this form:

$$\Delta E = (-1.66 - 0.0138 \times E)\rho x, \tag{4.1}$$

where the change in energy, ΔE, is measured in MeV, the material density, ρ, in gcm^{-3}, and the distance travelled in the material, x, in cm. The value of 1.66 MeVcm^{2}g^{-1} is an average value of the minimum rate of energy loss for particles in different materials. The energy dependent factor has been tuned to the GEANT simulation of energy loss in the DØ detector.

For a charged particle moving in a magnetic field, its trajectory is determined by its momentum. Low momentum particles curve more than higher momentum particles and, for this reason, the energy loss must be applied with some care. To apply it at the entrance or exit of a medium would result in inaccuracies in the final position of a particle. The ideal solution would be to calculate the energy loss as the particle progresses. However, a working approximation has been achieved by subtracting the total energy loss at the half way point through the layer. This minimises the correlations between the uncertainty in energy loss and final position of the particle and also reduces the calculation time.

4.3.2 Multiple Scattering Through Small Angles

As discussed in section 2.3.3, charged particles are scattered as they pass through a material. The total scattering is the result of multiple scatters along the path of the particle. Most of the individual scatters produce small angle deflections, with occasional larger angle deflections. The effect of multiple scattering on a particle passing through a thick layer of material is shown in figure 4.3.

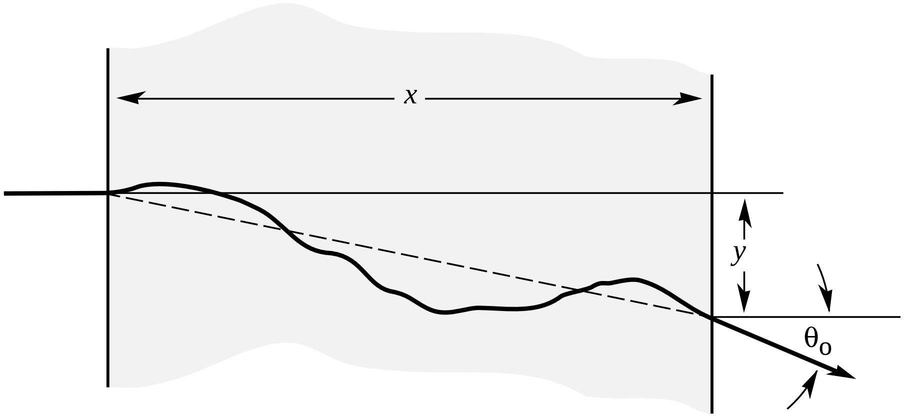

Figure 4.3: The effect of multiple scattering on the passage of a particle through a layer of material x cm thick. The parameters y and θ_0 are defined in the text.

Ignoring the larger angle scatters, a Gaussian fit to the central 98% of scattering angle has a width given by [11]:

$$\theta_0 \;=\; \frac{13.6\ \mathrm{MeV}}{\beta p}\; z\,\sqrt{\frac{x}{X_0}}\;[1 \;+\; 0.038\ \ln(x/X_0)] \tag{4.2}$$

where p, β and z are the momentum (in units of MeV), velocity (as a fraction of the speed of light) and charge (in units of e) of the incident particle, x is the thickness of the material, in cm, and X_0 is the radiation length (as defined in section 2.3.2).

In DØ it is often the case that the scattering is caused by several layers of different material. In this case, the scattering angles from each layer could simply be added in quadrature, but because of the non-Gaussian tails to the distribution, this yields a combined result which is systematically too small [11]. A more accurate result is obtained by calculating a single θ_0 from the combined x and X_0 of all the material.

The parameter, y_{rms}, describes the mean effect of the scattering on the position of a particle. It is related to θ_0 by this equation:

$$y_{rms} = \frac{1}{\sqrt{3}} x\theta_0 \tag{4.3}$$

For a thin layer, x can be small, and y_{rms} negligible. The GTR propagators for the silicon and fibre trackers assume that all the material is in thin layers. For the thick layers of the solenoid and calorimeter, the position scattering parameter, y_{rms}, must be included.

The parameters θ_0 and y_{rms} represent uncertainties in the position and direction of a particle having passed through a layer of material. These uncertainties must therefore be converted to errors on the five parameters used to describe tracks on different surfaces. These conversions are given in Appendix A.

It is then possible to add these mean values to the error matrix of a track that is exiting a thick layer of material.

However, the particle will have lost energy while traversing the medium. So to simply use the final energy when calculating the multiple scattering would result in an overestimate of the errors. Instead, the average of the incoming and outgoing energy is used.

4.4 Material Model for the Track Propagators

Four track propagators cover the regions outside the central tracking system. These are a solenoid propagator, central calorimeter propagator and two end cap calorimeter propagators. In this section, a brief description is given of the material model used for each of these. Figure 4.4 shows the regions covered by the propagators.

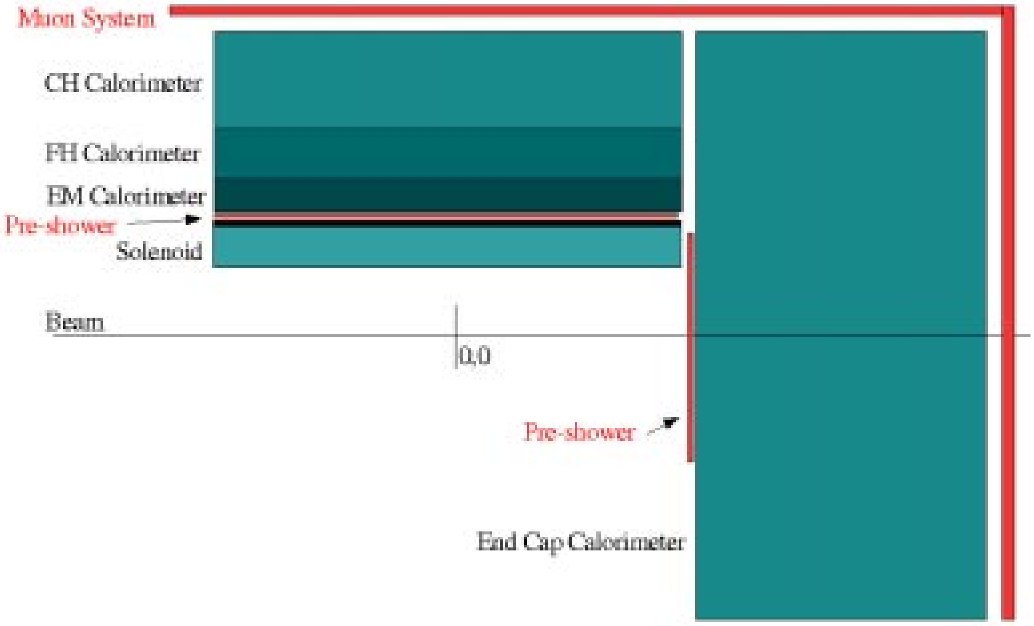

Figure 4.4: A cut away view showing the regions covered by the propagators. There is an additional end-cap calorimeter at negative z, and all regions give full 2π coverage in ϕ.

4.4.1 Solenoid and Lead Absorber

The solenoid magnet at DØ has a superconducting coil held in a cryostat. Liquid helium is used to maintain an operating temperature of around 4 K. The cryostat walls and coils are made of aluminium, chosen for its large radiation length. The solenoid extends between $|z| < 140$ cm and from a radius of 52 cm to 71 cm. It has a total thickness of 0.88 radiation lengths [18].

As the multiple scattering is treated as a correction to a track error matrix upon exiting a layer of material, the solenoid is treated as a solid cylinder of uniform density, 19 cm thick. Thus, the average radiation length is taken as $19/0.88 = 21.6$ cm. This approach leads to small inaccuracies when only part of the solenoid is traversed. In such cases a more accurate method may be devised in the future.

On the outer radius of the solenoid is a layer of lead associated with the central pre-shower detectors. This lead is 0.556 cm (approximately 1 radiation length) thick, bringing the total amount of material in the solenoid to just under two radiation lengths. As this lead contains a significant amount of material compared to the rest of the solenoid, it is treated as a separate thin layer.

4.4.2 Calorimeter

The calorimeter is divided into three volumes, each with its own propagator.

Central Calorimeter

The central calorimeter is treated as a thick cylinder, with an inner radius of 75 cm, an outer radius of 220 cm and extending between $|z| < 140$ cm. The central calorimeter is divided into three sub-volumes, matching the electromagnetic, fine hadronic and coarse hadronic layers. For each layer the average density and radiation length were calculated from the densities and amounts of the different materials present [24]. Each layer is then treated as a uniformly dense cylinder, with the average density,ρ, and radiation length,X_0, (given in table 4.2) used for the multiple scattering and energy loss calculations in the propagator.

Layer	Electromagnetic	Fine Hadronic	Coarse Hadronic
ρ / gcm^{-3}	8.85	13.4	3.1
X_0 / cm	0.86	0.67	2.69

Table 4.2: The average densities (ρ) and radiation lengths (X_0) for the central calorimeter.

As with the solenoid layer, the energy loss is calculated in the middle of each layer. The multiple scattering is calculated at the exit using the average energy.

Calorimeter End Caps

The end-cap calorimeters are also divided into three regions: electromagnetic, fine hadronic and coarse hadronic. However, unlike the central calorimeter, the boundaries between these regions are difficult to describe with the existing surfaces in GTR (see figure 2.6).

For this reason, the end cap units are simply modified as one thick cylinder, with an inner radius of 3 cm (surrounding the beam), an outer radius of 220 cm and extending between ± 140 and ± 200 cm in z.

Again, the average density (8.2 gcm^{-3}) and radiation length (0.9 cm) used in the multiple scattering and energy loss calculations are derived from information on the materials in the end cap calorimeters [24].

4.5 Testing the Track Extrapolation

The track extrapolation can be tested by comparing the extrapolated tracks with the actual parameters of particles at the pre-shower and muon detectors. Because of the random nature of multiple scattering and energy loss, the extrapolated tracks will not give the correct parameter values for each individual particle, but the discrepancies should be within the errors on the extrapolated tracks. In other words, the spread in positions and directions seen with the real particles should be reflected in the error matrix on the extrapolated tracks.

As the track propagators were being developed, no real data were available. So, simulation events, as described in section 2.9.1, was used to test the algorithms. This has the advantage that the effects of detector resolution in, for example, the muon system do not need to be taken into account, as the exact position of the simulated particles is given. However, it is dependant upon the accuracy of the detector description used in the event simulation.

4.5.1 Comparing Extrapolated Tracks With Simulation

High energy muons, which generally pass through the entire DØ detector without forming a shower of secondary particles, provide the best test for the track extrapolation. So, four samples of 7500 simulated events, each containing a single muon, were generated. These samples contained:

1. 5 GeV muons with $|\eta| < 1$ ('central').
2. 40 GeV muons with $|\eta| < 1$ ('central').
3. 5 GeV muons with $1 < \eta < 3$ ('forward').
4. 40 GeV muons with $1 < \eta < 3$ ('forward').

As multiple scattering decreases with energy, the 5 GeV samples will provide the most thorough check of the extrapolation performance. As muons with less than approximately 4 GeV will be unlikely to penetrate the calorimeter and muon system toroid magnet, the 5 GeV sample is also close to the lower energy limit that will be used at DØ. At 40 GeV, the effects of multiple scattering are small, so these samples are used to check the energy dependence of the error calculations.

For all samples, cuts were placed on each event, requiring a reconstructed track and muon that reached the central or forward muon system, for the central and forward samples respectively. For this reason, not all of the 7500 events in each sample were used.

The simulation provides the position of each muon at various points of the DØ detector. Combined with the extrapolated track parameters, it is possible to form *residuals*, defined by:

$$\Delta x \;=\; x_{GTR} \;-\; x_{MC} \tag{4.4}$$

where x_{GTR} is a track parameter reconstructed by the GTR algorithm and propagator and x_{MC} is the same parameter for the simulated muon. The effects of energy loss are apparent in the residuals. If too much or too little energy loss is calculated, the curvature residual (q/p or q/p_T, depending on the surface type) will have a non-zero mean value. Such an effect would shift the mean of the curvature for opposite charges in opposite directions, so the residuals for the two charges are shown separately in the following sections. Generally, the residuals should be approximately Gaussian and give a quantitative measure of the spread in the track parameters.

This spread should be reflected in the track error matrix, which can be tested by forming the *pulls*, defined by:

$$x_{Pull} = \frac{x_{GTR} - x_{MC}}{\sigma_{x_{GTR}}} = \frac{\Delta x}{\sigma_{x_{GTR}}} \tag{4.5}$$

which is the x residual divided by the reconstructed error on parameter x. If the errors are correctly reflecting the uncertainty in the track reconstruction and the interactions of particles as they pass through the DØ detector, these pulls should have unit width. Each pull distribution in the following sections is fitted with a Gaussian distribution, to remove the effect of any tails caused by large angle scatters.

4.5.2 Fibre Tracker Results

Using the information from the simulated muon positions in the fibre tracker it is possible to test the track reconstruction. As the cluster of deposited energy in this fibre layer is actually used to reconstruct the muon's track, such studies give an estimate of the default tracking algorithm performance.

Residuals and pulls for the tracks at the outermost fibre layer are shown in figures 4.5 to 4.8 for the central 5 and 40 GeV samples. The outer fibre layer is represented by a cylinder, so the cylindrical track parameters are used.

The ϕ residual has an RMS of approximately 70 μrad. At the radius of the outer fibre layer (52 cm) this corresponds to a spread of 36 μm. Residuals of the other position coordinate, z, have an RMS of approximately 590 μm. The pull distributions all have RMS values between 1 and 1.1, indicating that the calculated

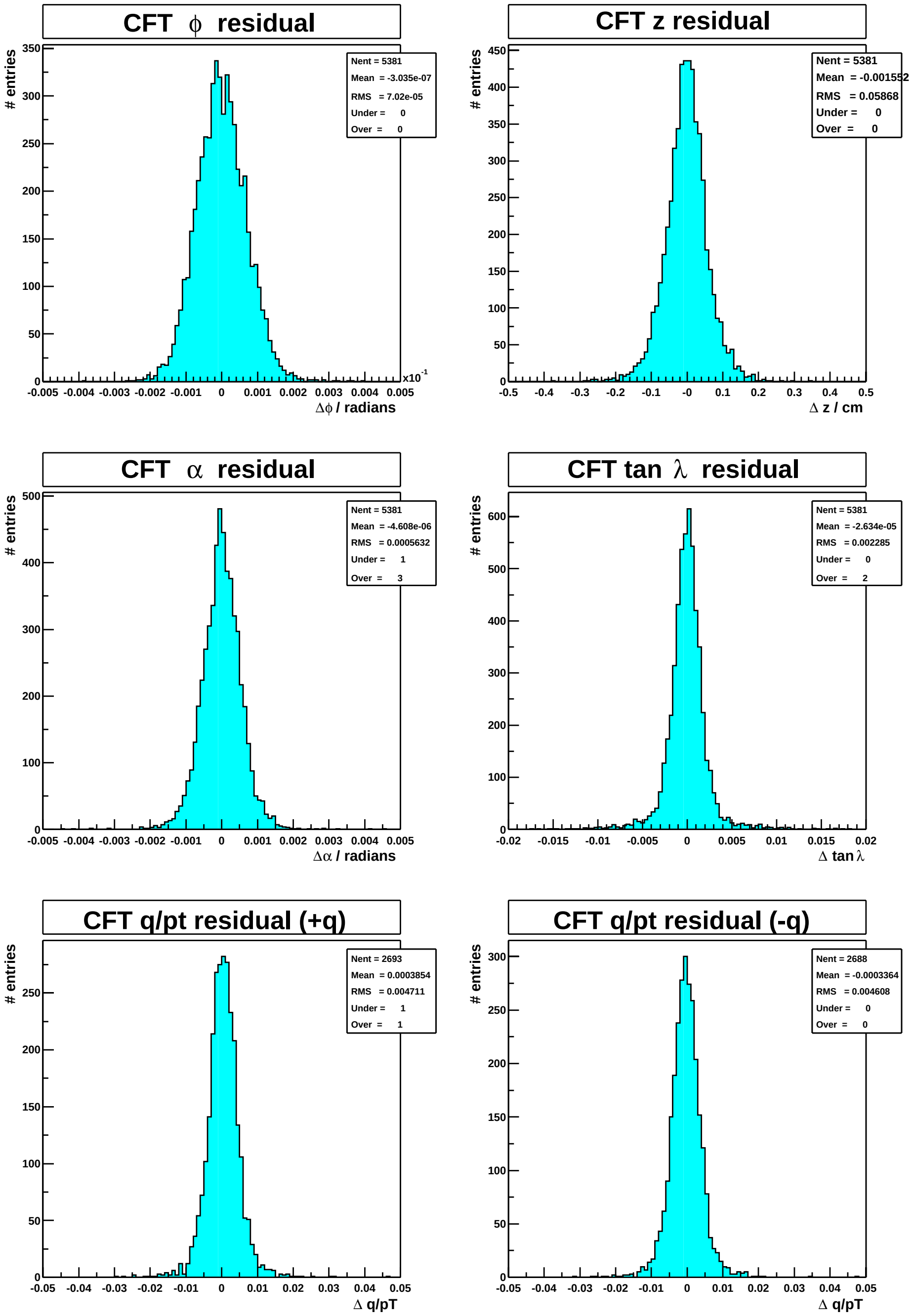

Figure 4.5: Track residuals at the outer CFT fibre layer for the central 5 GeV sample. Clusters in this layer are used to build tracks, so these residuals give an indication of GTR performance.

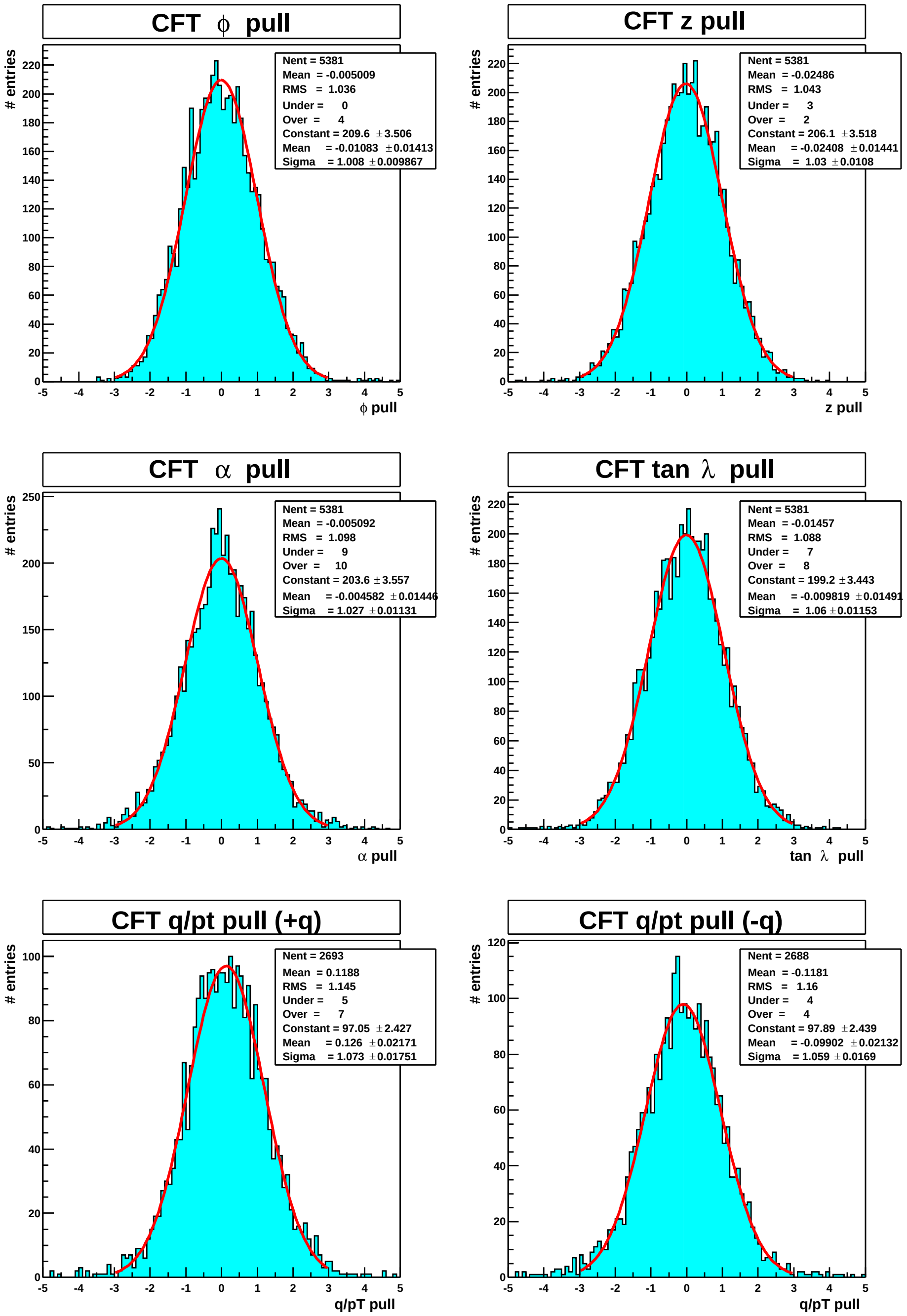

Figure 4.6: Track pulls at the outer CFT fibre layer for the central 5 GeV sample, fitted with a Gaussian distribution. The unitary widths show that the reconstructed tracks have correctly calculated error matrices

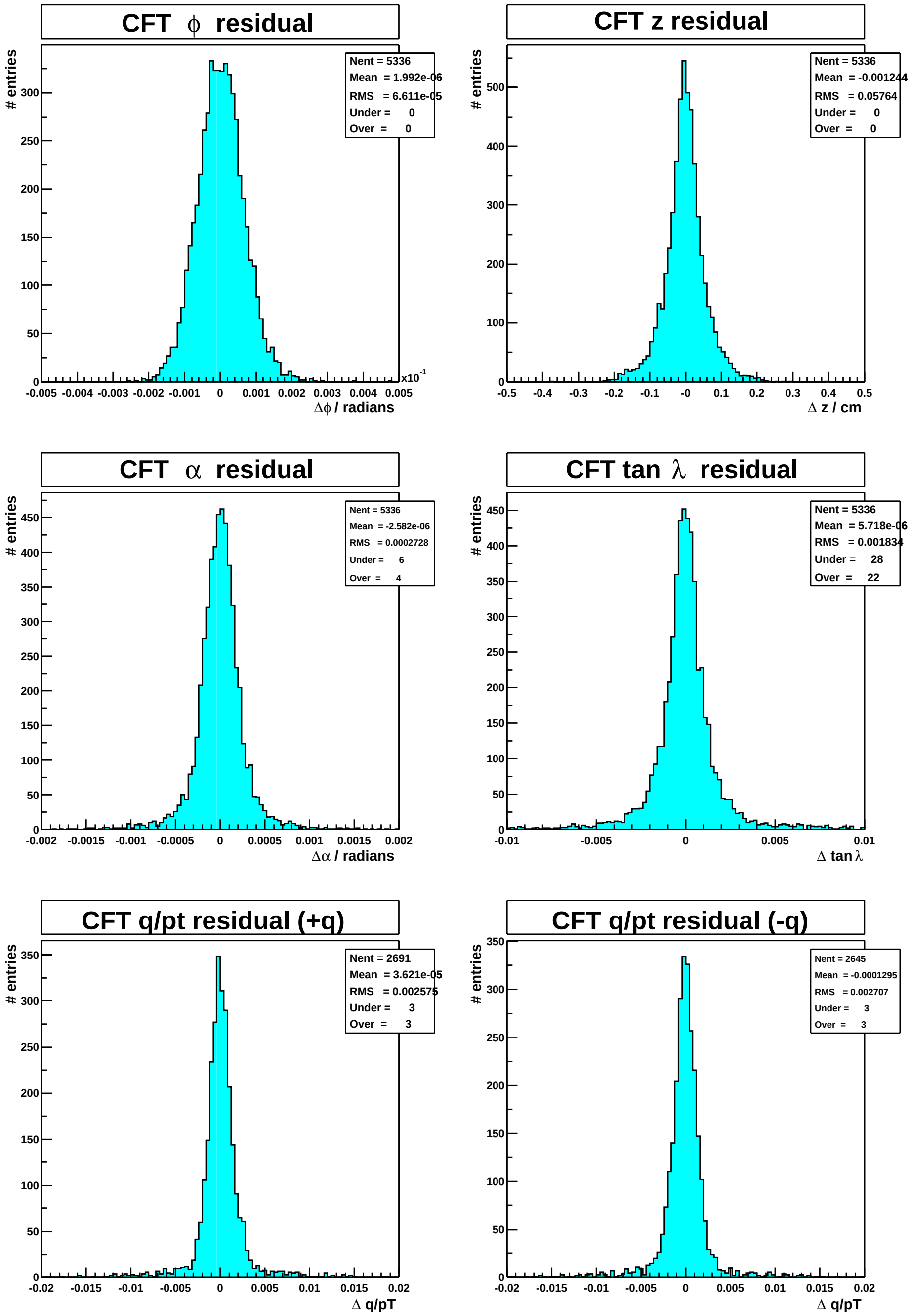

Figure 4.7: Track residuals at the outer CFT fibre layer for the central 40 GeV sample.

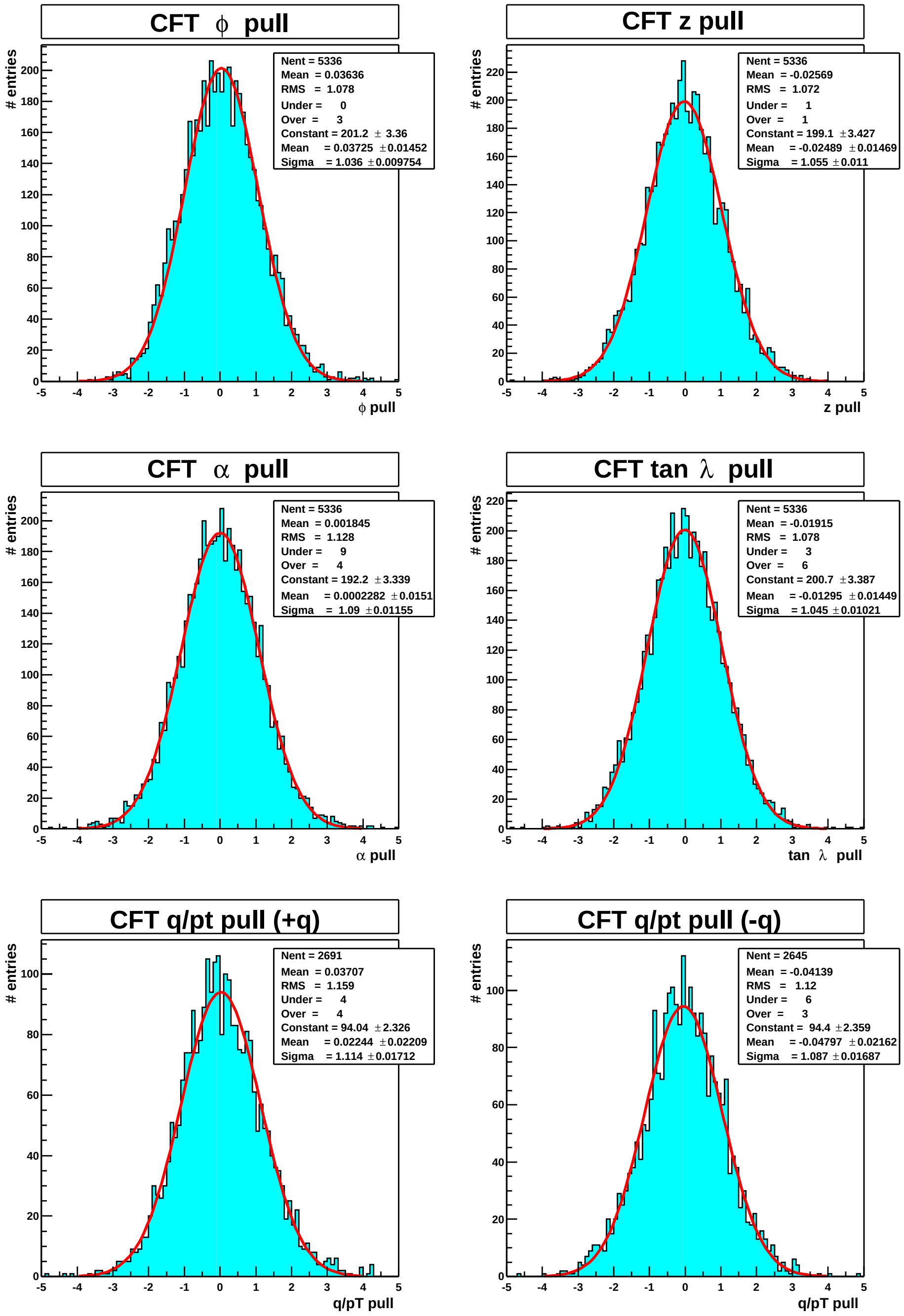

Figure 4.8: Track pulls at the outer CFT fibre layer, fitted with a Gaussian distribution for the central 40 GeV sample.

errors are correct.

The means of the q/p_T pulls for the different charges in figures 4.6 and 4.8 are shifted in opposite directions away from zero. The direction of the shift indicates that the reconstructed p_T is lower than the actual p_T. This effect has been observed in the GTR algorithm, when a slightly underestimated momentum allows larger track errors (due to overestimating the amount of multiple scattering) and thus a lower fit χ^2.

4.5.3 Pre-shower Results

The first test of the propagators is to extrapolate these track to the central pre-shower detectors and compare to the parameters of the muons at this point.

A cylinder is defined with the radius of the first layer of the central pre-shower detectors (71 cm), and tracks are extrapolated to this cylinder using the solenoid propagator. The residual and pull distributions are shown in figures 4.9 to 4.12 for the 5 and 40 GeV samples.

By comparing the residuals at the fibre tracker and pre-shower, the effects of the multiple scattering in the solenoid can be seen. For example, in the 5 GeV sample, the ϕ residual increases by a factor of around 7, and the $\tan\lambda$ residual by a factor of around 3. In the 40 GeV sample, where multiple scattering is less significant, the ϕ residual increases by a factor of around 2.4, and the $\tan\lambda$ residual by a factor of around 1.06.

The q/p_T residuals for both charges in the 5 and 40 GeV samples are centred at zero, indicating that the energy loss has been calculated correctly.

The pull distributions in figures 4.10 and 4.12 show that the scattering and uncertainty in energy loss are correctly reflected in the updated track error matrices. The error matrices are correct for both the 5 and 40 GeV samples, indicating that the energy dependence of these effects is also correctly calculated.

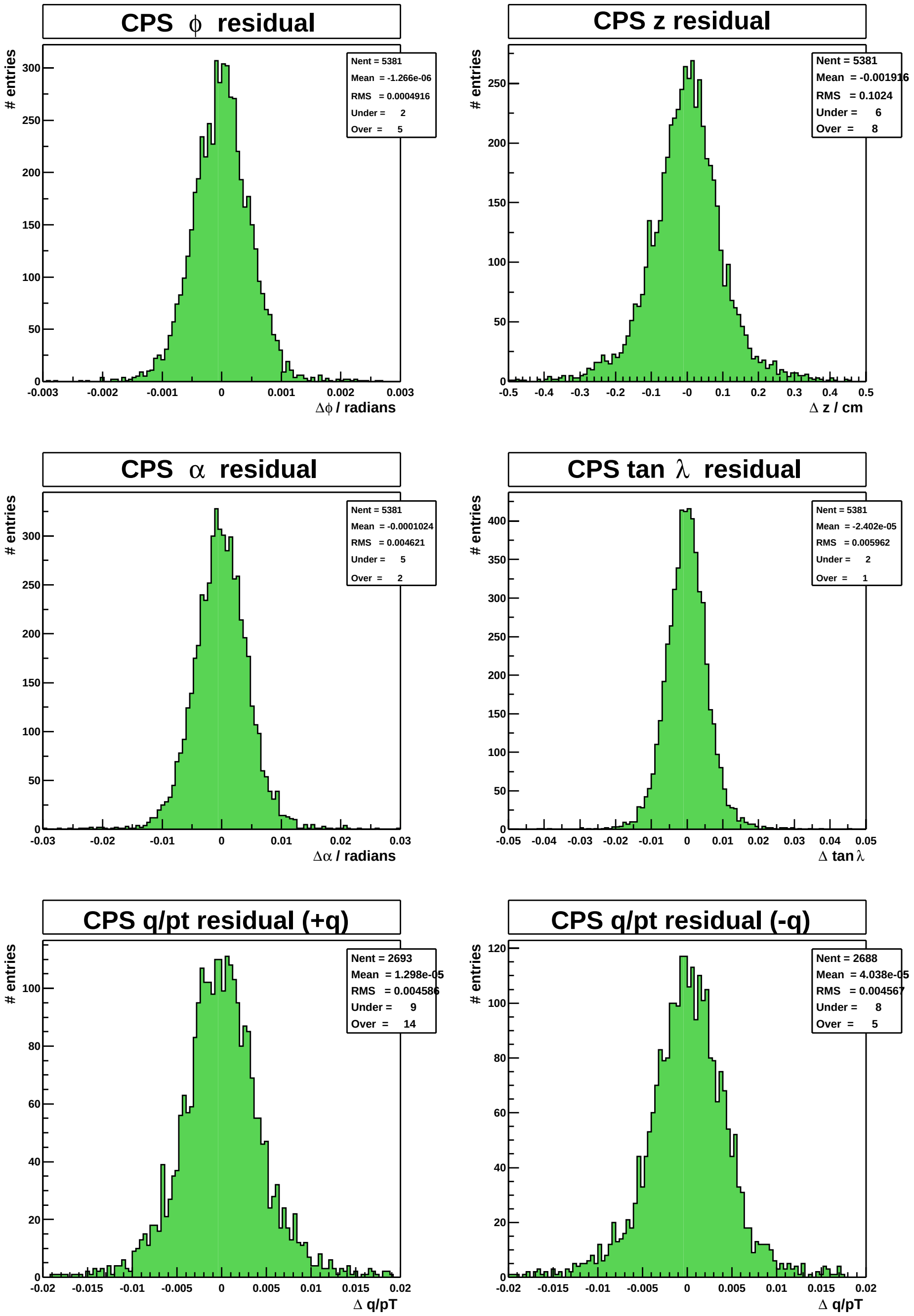

Figure 4.9: Track residuals at the central pre-shower for the central 5 GeV sample.

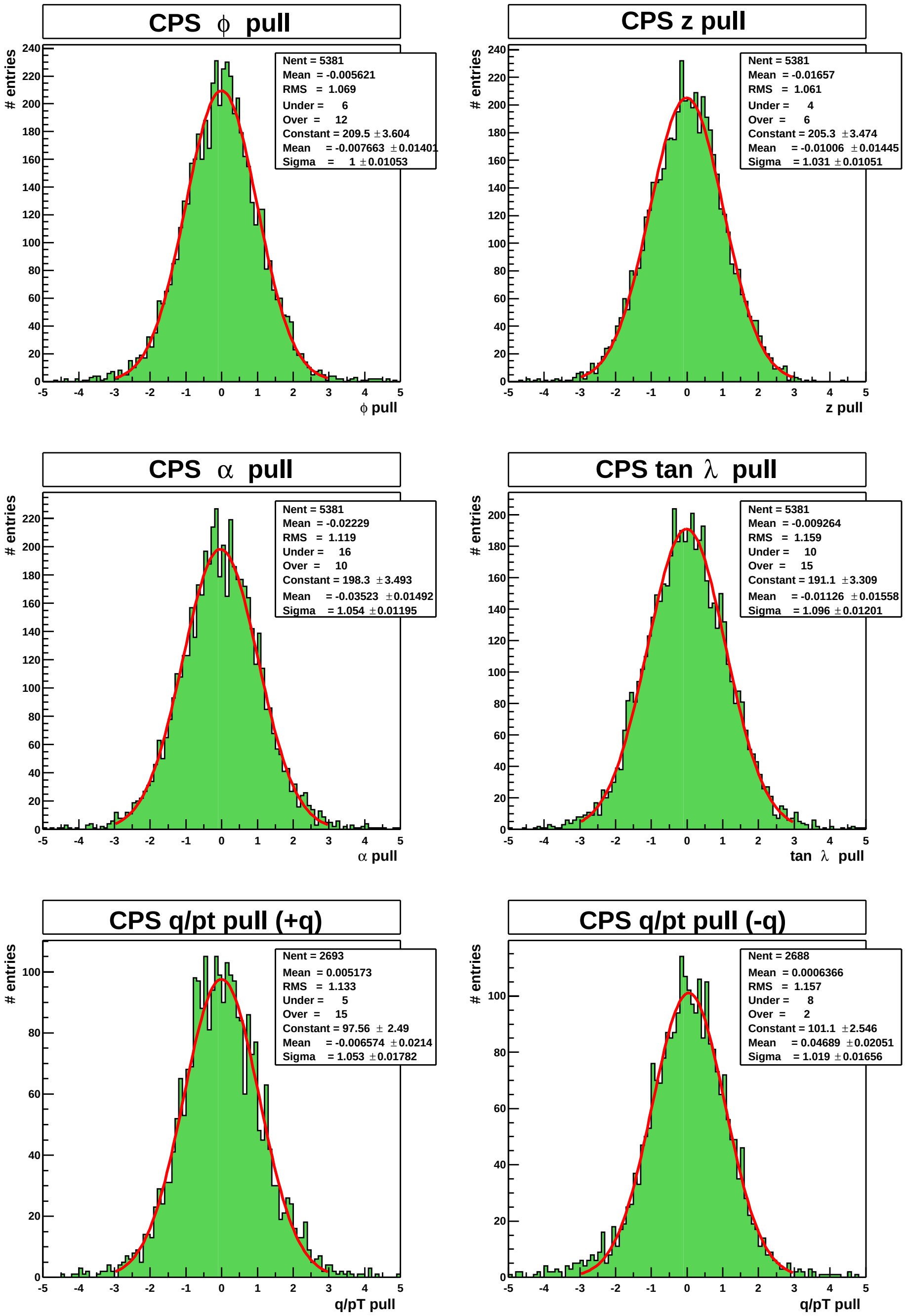

Figure 4.10: Track pulls at the central pre-shower for the central 5 GeV sample. Unitary widths show the track errors correctly reflect the multiple scattering and energy loss.

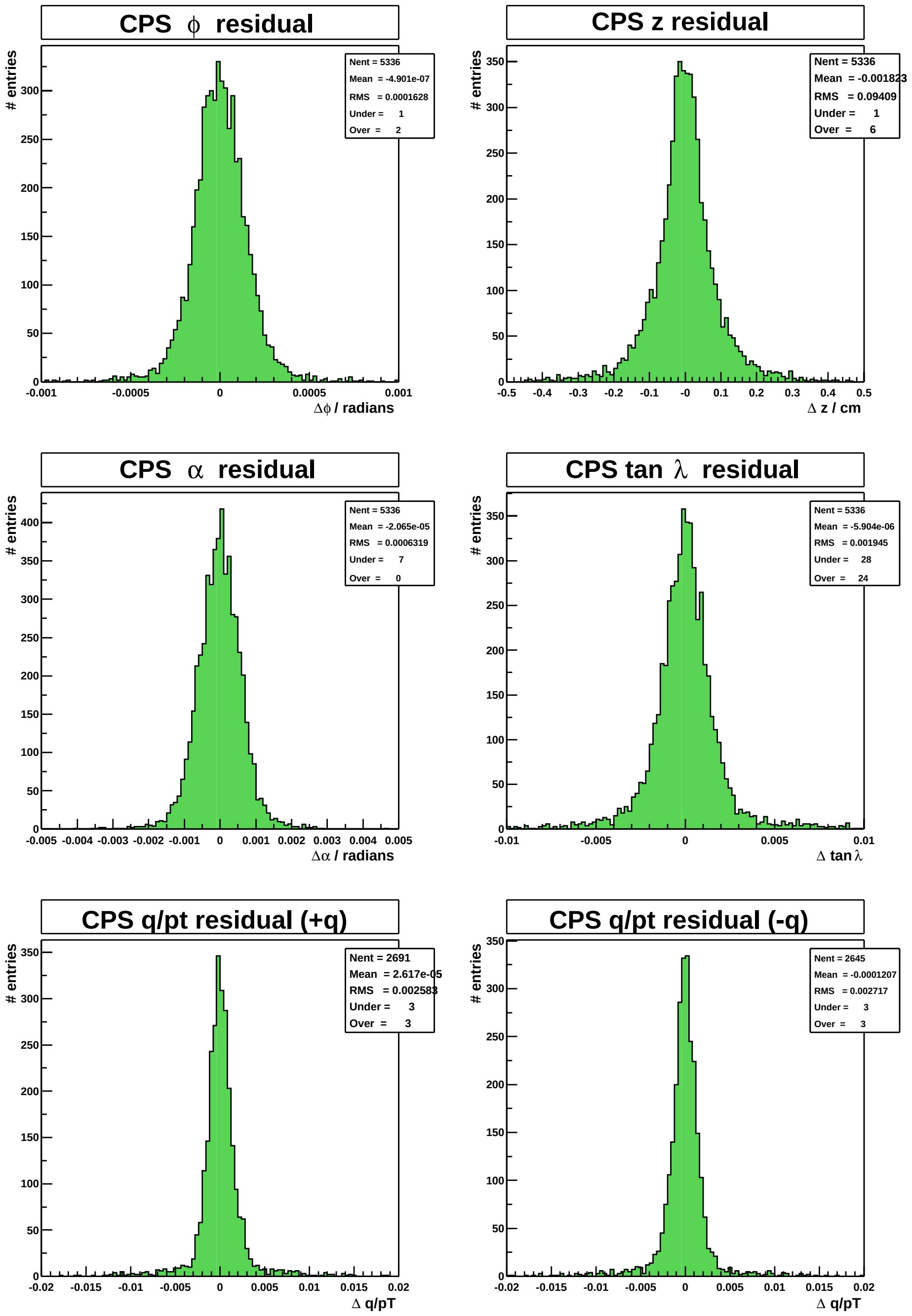

Figure 4.11: Track residuals at the central pre-shower for the central 40 GeV sample.

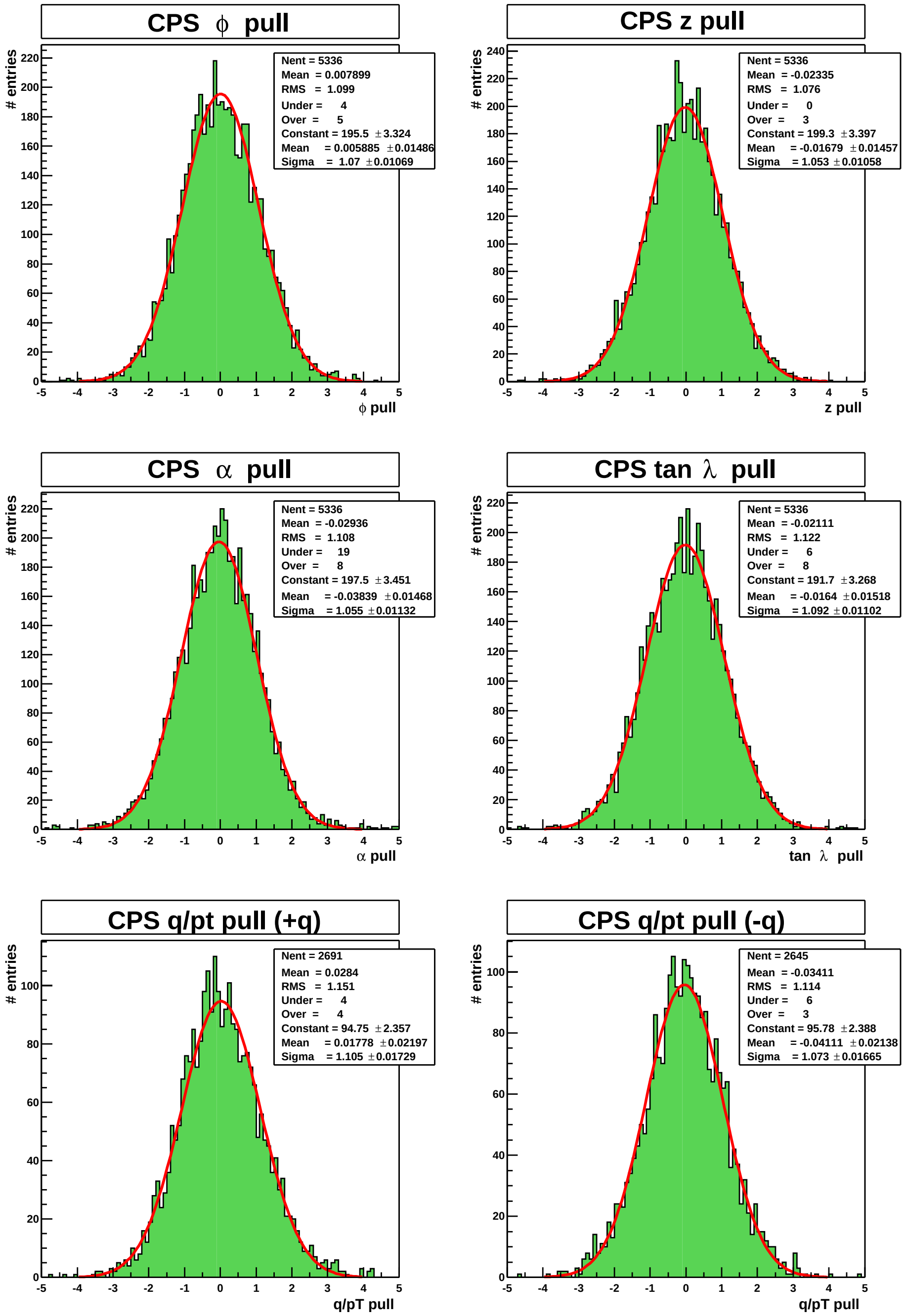

Figure 4.12: Track pulls at the central pre-shower for the central 40 GeV sample. Unitary widths show the track errors correctly reflect the multiple scattering and energy loss.

4.5.4 Muon System Results

Finally, to test the calorimeter propagators, the tracks were extrapolated to the muon system and compared to the simulated muons at this point. To approximately model the muon system, six planes were used to define a box - four x-y planes for the central muon system and two z planes for the forward. The planes were located to match the positions of the first layer of drift detectors in each region (the muon system design is discussed in more detail in Chapter 5). This corresponds to ±297 cm in x and y, and ±427 cm in z.

Central Muon System

The central muon samples are required to reach the central muon system, defined as the $x - y$ planes of scintillators and drift chambers extending to $|z| < 370$ cm. As the tracks were extrapolated to x-y planes rather than cylinders, different track parameters are used. Residuals and pulls for the 5 and 40 GeV central samples are shown in figures 4.13 to 4.16

In the 5 GeV sample, the position residuals Δv and Δz have a spread of around 12 cm, indicating significant scattering effects. For the 40 GeV sample, this is reduced to around 1.5 cm, highlighting the strong momentum dependence of multiple scattering. An approximate 'rule of thumb' derived from these samples is that the spread in position due to multiple scattering is approximately $\frac{60}{p}$ cm, with the momentum (p) measured in GeV.

The position and direction parameter pull distributions in both samples have values close to, but slightly below 1. This indicates that the scattering is being slightly overestimated, but overall handled well.

The q/p pulls in the 5 GeV sample show tails, with the position of the tail indicating that some muons are losing more energy than that calculated by the propagator. For these muons, the 2.5 GeV deposited in the calorimeter represents a significant amount, so it is possible that the simplifying assumptions used when

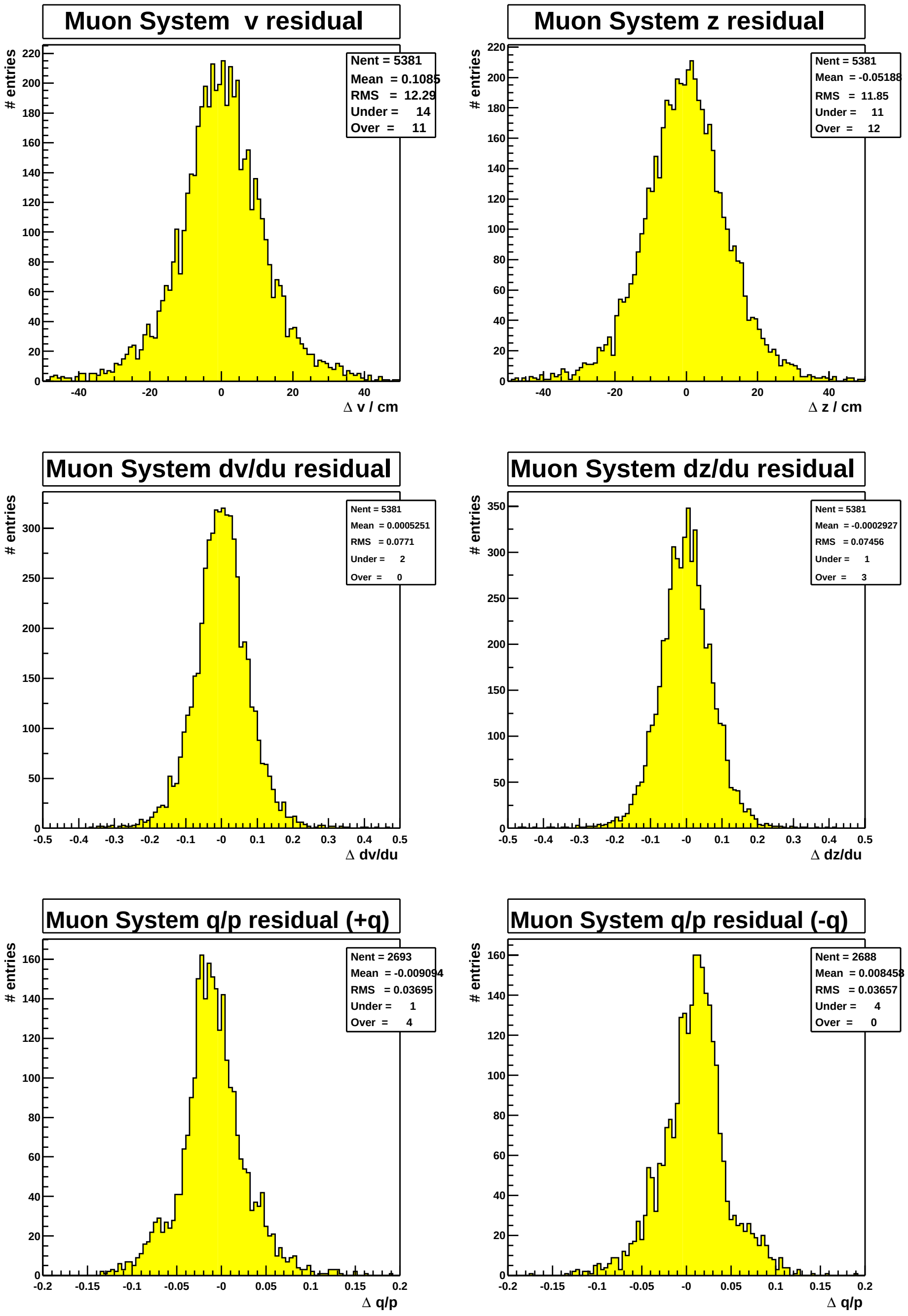

Figure 4.13: Track residuals at the central muon system for the central 5 GeV sample.

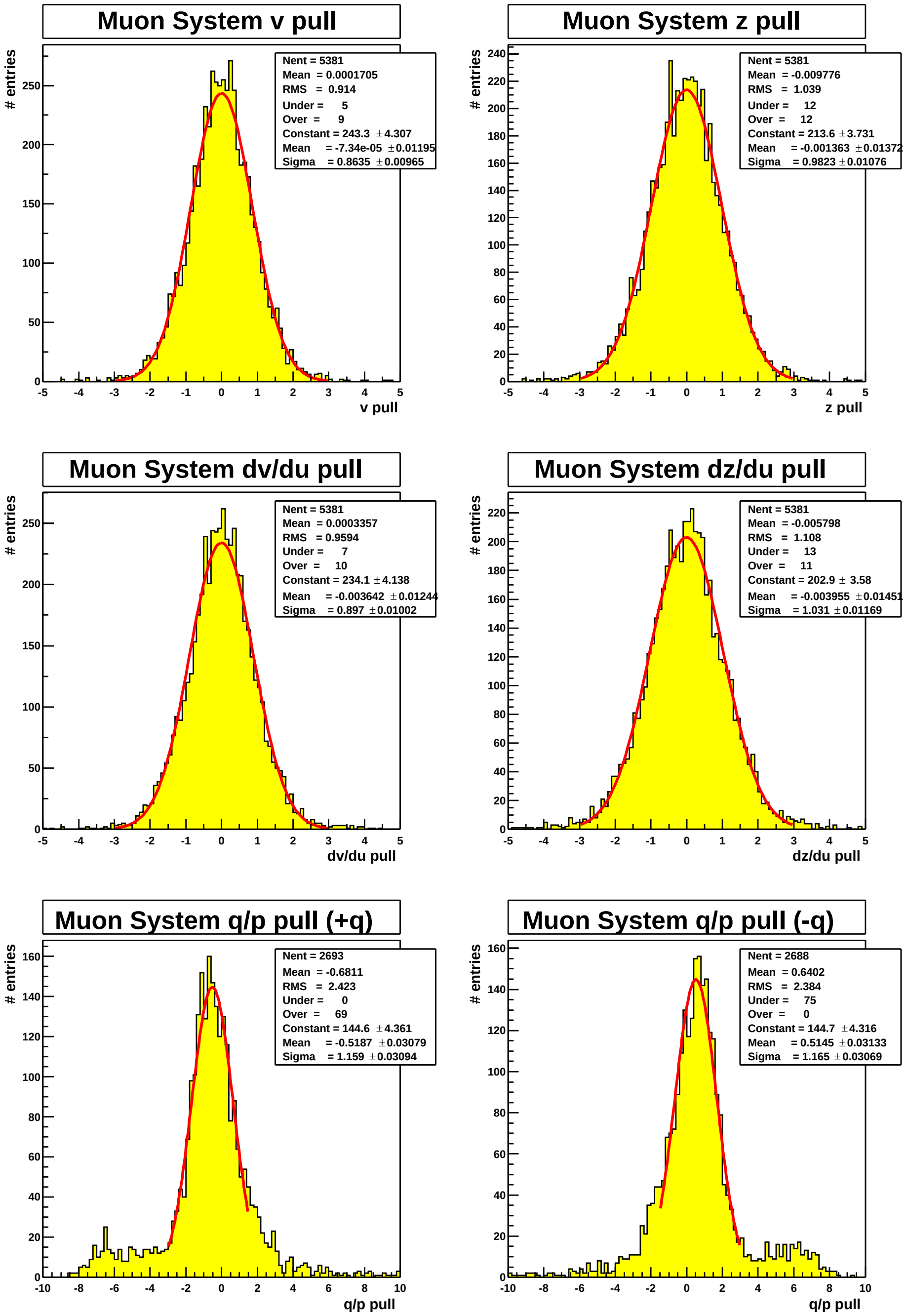

Figure 4.14: Track pulls at the central muon system for the central 5 GeV sample.

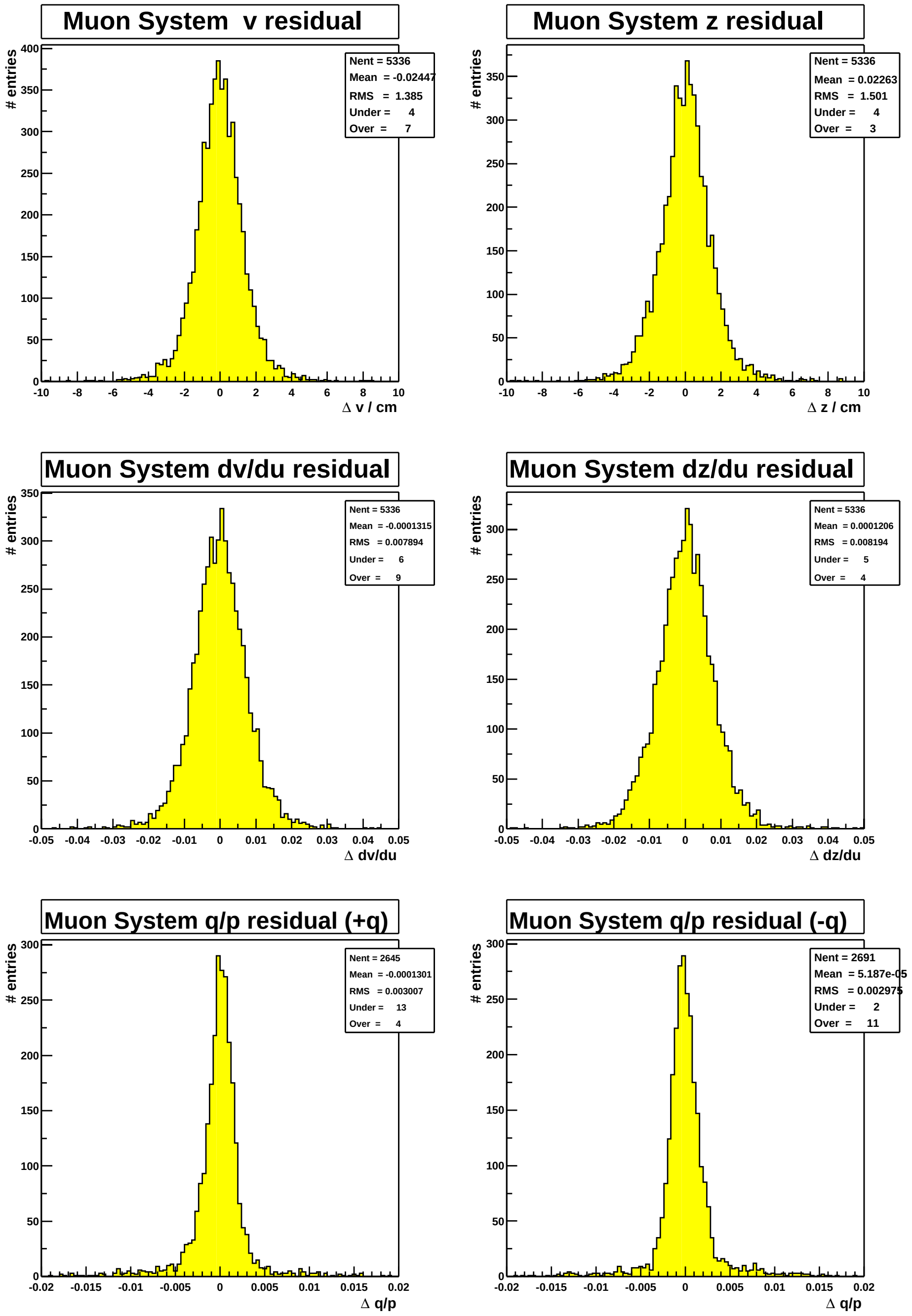

Figure 4.15: Track residuals at the central muon system for the central 40 GeV sample.

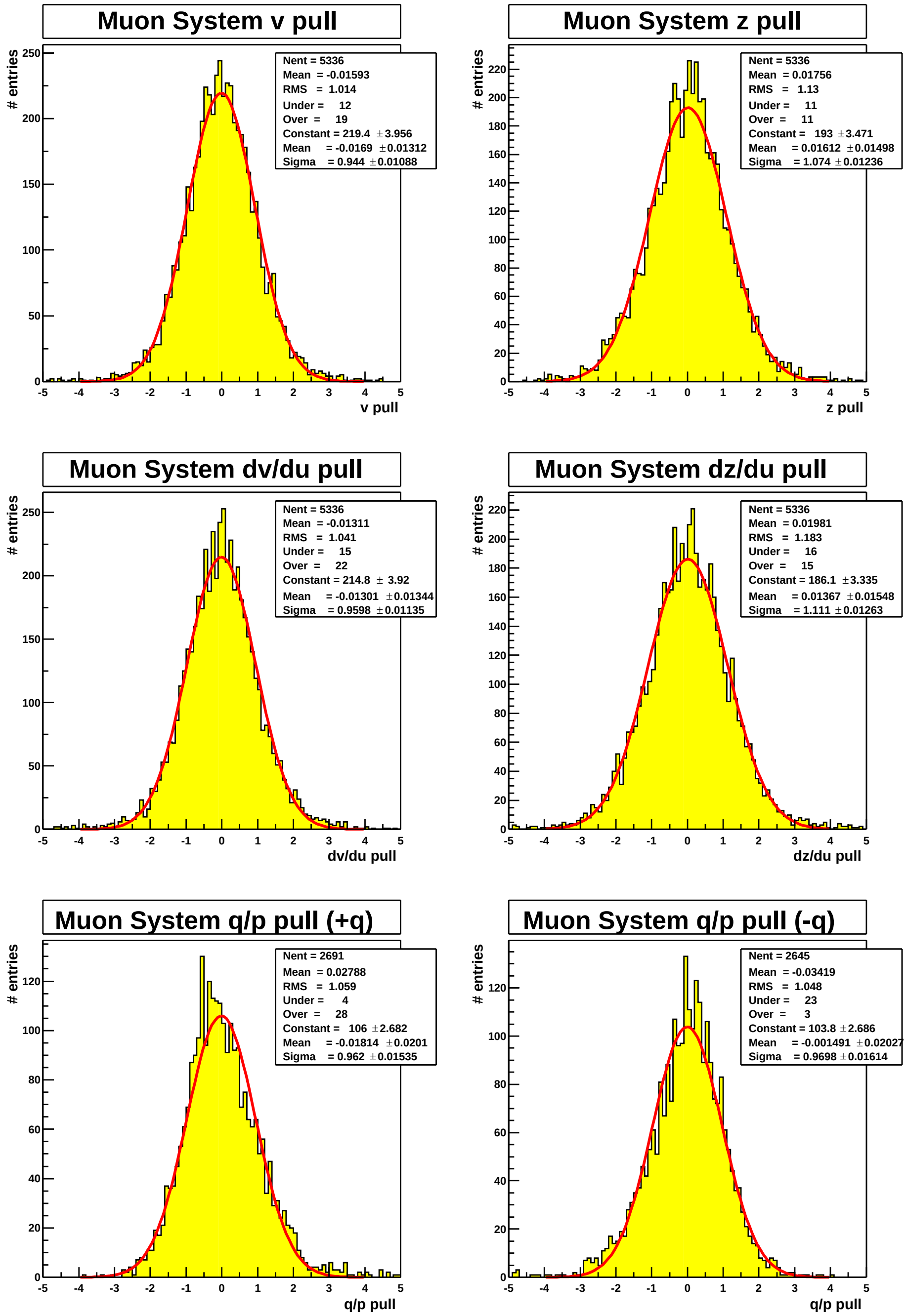

Figure 4.16: Track pulls at the central muon system for the central 40 GeV sample.

calculating the energy loss in the propagator are not longer valid. The amount of energy lost by the muons actually follows Landau rather than Gaussian distribution, with some muons losing significantly more energy than the average. So these tails could also be a manifestation of this effect.

Forward Muon System

The forward muon samples are required to reach the forward muon system, defined as the scintillators and drift chambers arranged in z planes. Figure 4.17 shows that the geometry of the actual forward muon system is more complicated than the simple 'box' shape used for track extrapolation. So, only those muons reaching part of the forward muon system which match the 'box' geometry are used.

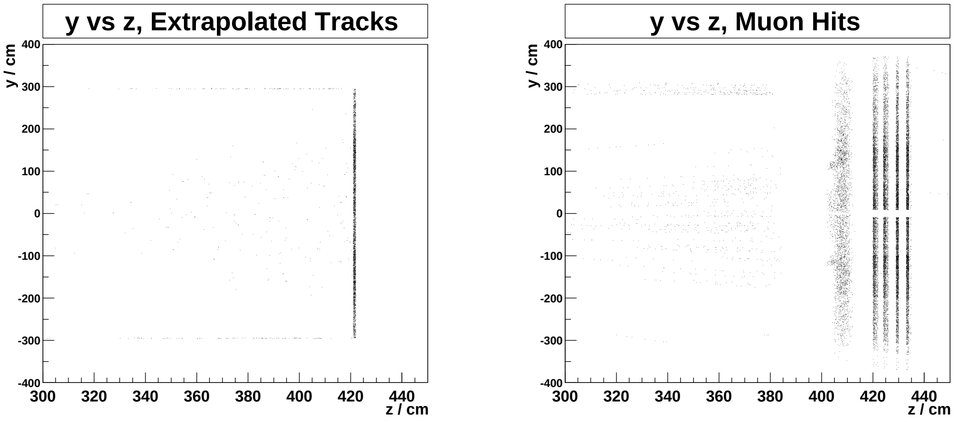

(a) (b)

Figure 4.17: Figure (a) shows the positions of the extrapolated tracks in the forward 5 GeV sample. Figure (b) shows the position of the muons in the muon system, highlighting the different geometry. Hits in the scintillator layer and four layers of drift tubes are visible.

Residuals and pulls for the 5 and 40 GeV central samples are shown in figures 4.18 to 4.21. Again, different track parameters are now used, as the tracks are extrapolated to a z plane.

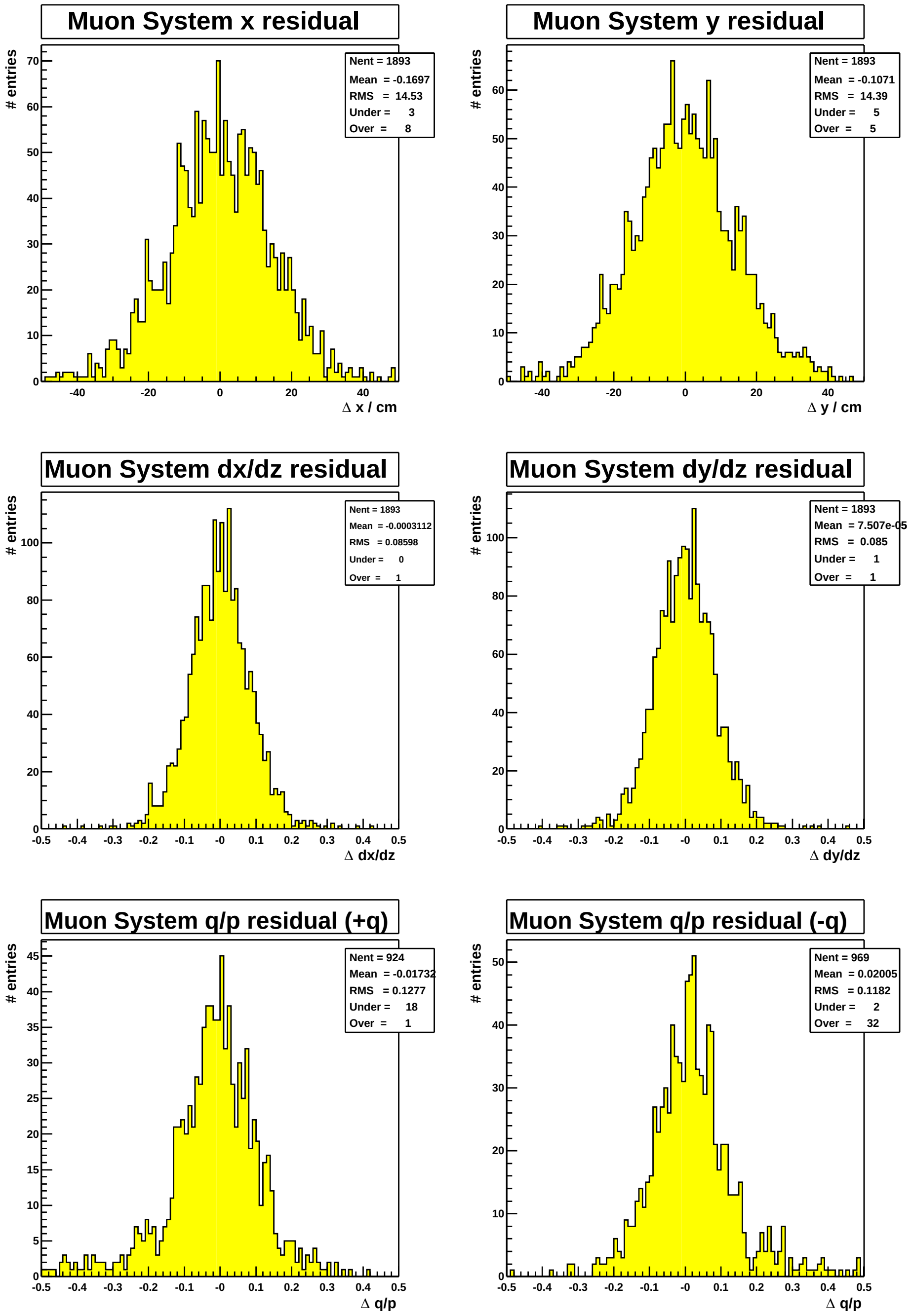

Figure 4.18: Track residuals at the forward muon system for the forward 5 GeV sample.

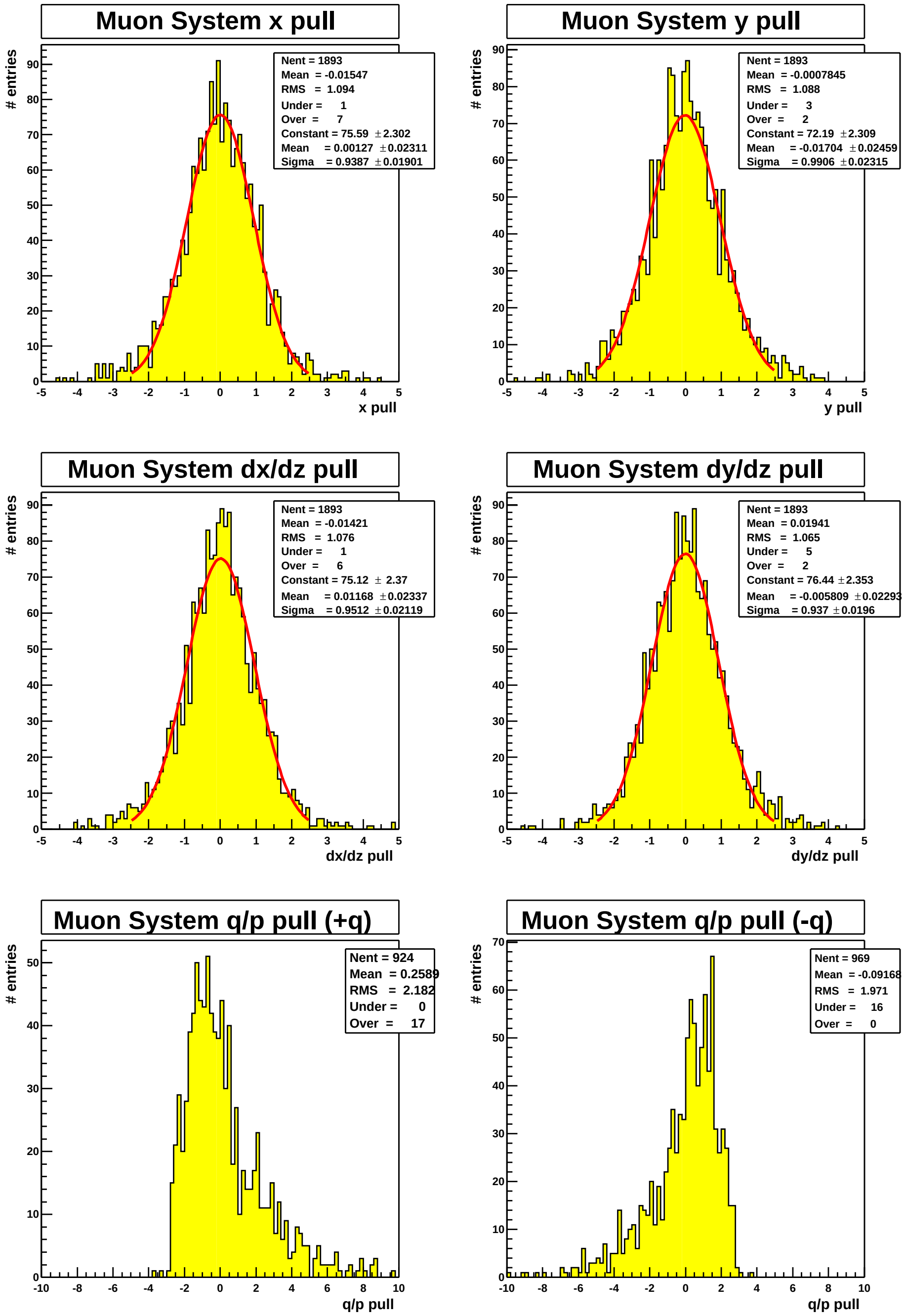

Figure 4.19: Track pulls at the forward muon system for the forward 5 GeV sample.

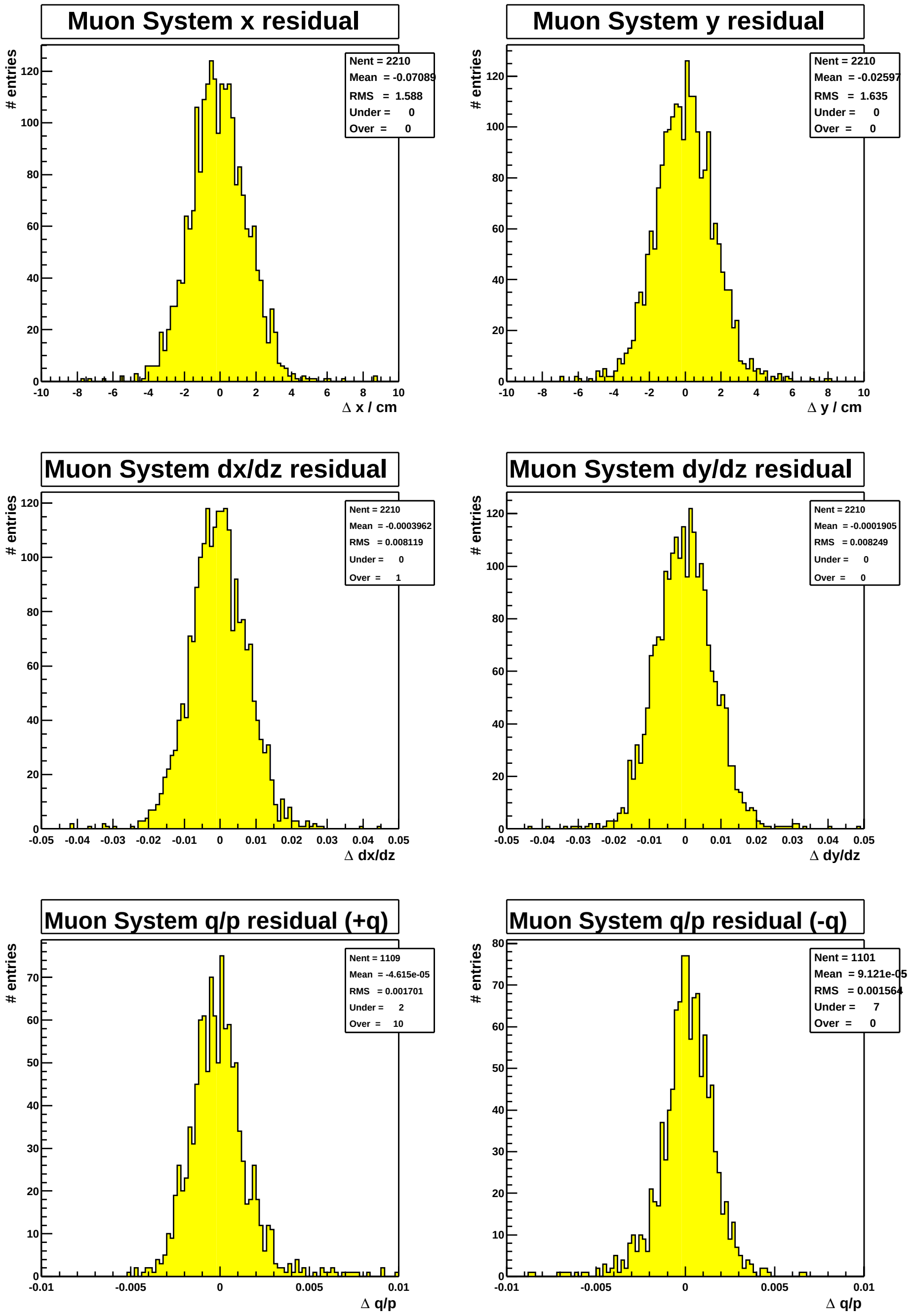

Figure 4.20: Track residuals at the forward muon system for the forward 40 GeV sample.

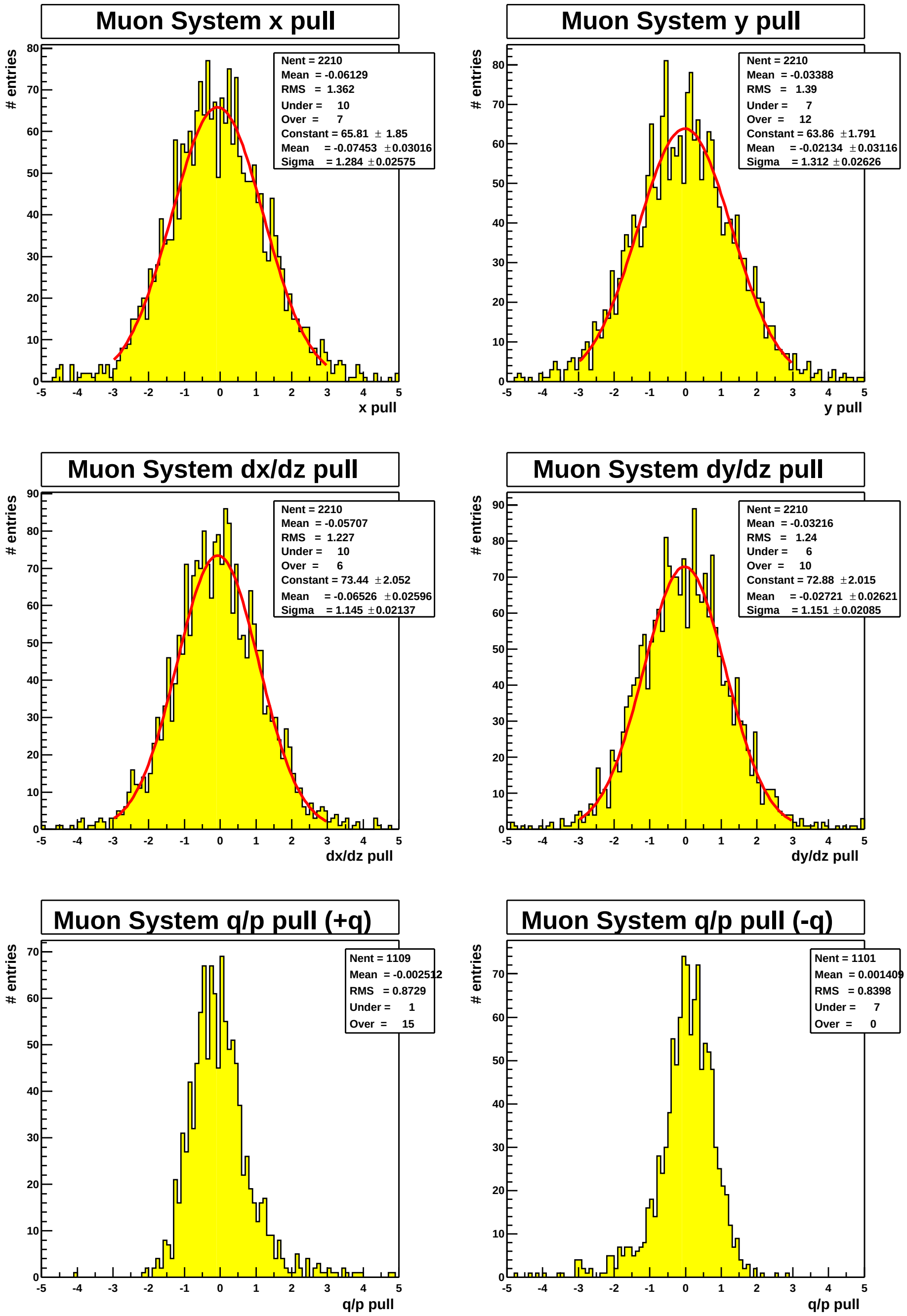

Figure 4.21: Track pulls at the forward muon system for the forward 40 GeV sample.

It can be seen that the position residuals are broader than for the central muon system, indicating that more scattering occurs for muons reaching the forward system. The position and direction pull distributions for the 5 GeV sample have widths very close to 1. In the 40 GeV sample, the widths are around 1.2. This difference may be caused by an incorrect error calculation in the initial track reconstruction or the simplifying assumption of treating the whole forward calorimeter region as one cylinder.

The q/p pull distributions in the 5 GeV sample show a tail. This tail is more prominent than that in the central sample, indicating a problem in the curvature extrapolation. Again this may be caused by uncertainties in the initial track reconstruction. Forward tracks will pass through fewer layers in the central tracking system and so have a less precise measurement of curvature. The problem could also be in treating the forward calorimeter as one volume, instead of the three used in the central calorimeter. So, in the future it would be desirable to implement these three layers for the end cap calorimeters as well.

4.5.5 Residual and Pull Distributions in Data

The next step in this study would be to carry out similar track extrapolation in data, with matching to reconstructed muons in the muon detectors. However, this was difficult, due to the tracking issues described in section 4.1.2, in particular with the final track list.

Due to the final filtering problem, this track list contained mostly tracks found only in the SMT. These track have the poorest momentum resolution, which then affects the multiple scattering and energy loss calculations carried out in the track propagators.

Alternatively, the five separate lists used to build the final track list could have been extrapolated. However, the most plentiful tracks were the axial fibre only tracks, which cannot be extrapolated correctly as they have no z information. Extrapolating the remaining four types of track required prohibitive amounts of computing time during event reconstruction, so was not attempted.

As a result, real data studies have been postponed until the tracking issues have been resolved.

Chapter 5

Muon Identification

This chapter provides an overview of muon identification at DØ. In section 5.1 there is a review of the muon detectors, including the trigger system. Section 5.2 covers the offline muon reconstruction. While the track extrapolation covered in Chapter 4 is intended to be used for muon identification, a simpler method had to be adopted for the data used for this thesis. This is described in section 5.3.

5.1 Muon Detectors

High energy muons are detected as they exit the DØ calorimeter. Here, a tracking system is used to provide position and momentum measurements. This also provides muon identification, as generally all other particles are completely absorbed in the calorimeter.

The muon detectors consist of three layers (labelled A, B and C) at increasing distance from the collision region. These provide position measurements with a combination of drift chambers (described in section 5.1.1) and scintillating pixels (described in section 5.1.2). A toroid magnet between the A and B layers allows a measurement of momentum through the curvature of the muon path.

The muon system has a different geometry than the rest of DØ, with a cuboid rather than cylindrical shape. In the *central* muon system, covering the range $|\eta| < 1$, detectors are arranged in planes of x and y. The two *forward* muon systems consist of detectors in planes of z, extending the coverage to $|\eta| < 2.2$. This is illustrated in figure 5.1, showing a cut-away view of the muon system.

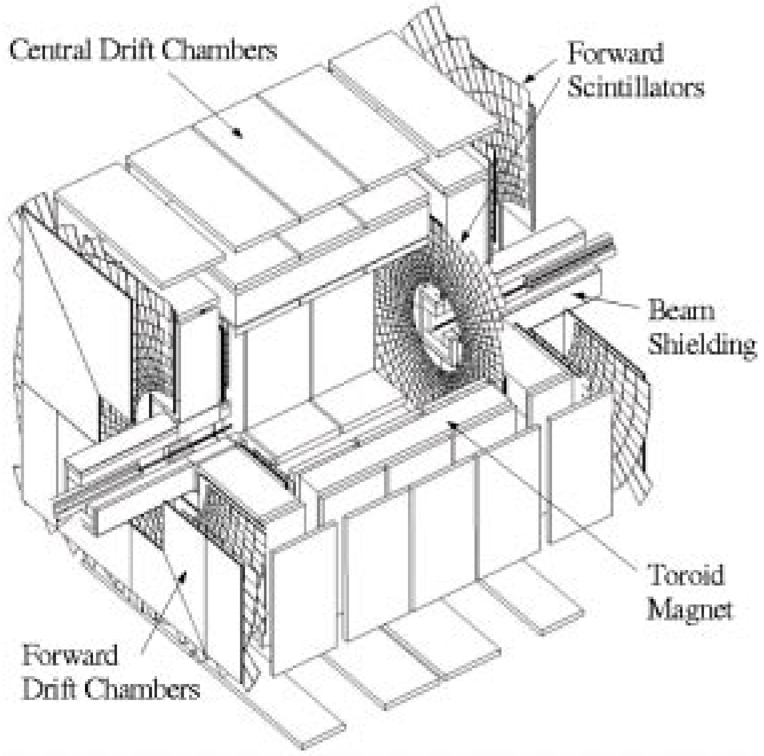

Figure 5.1: A cut away view of the DØ muon system. The drift chambers, forward scintillators and beam shielding are shown. The two layers of central scintillators are not shown.

5.1.1 Drift Detectors

Drift detectors provide a measurement of position by collecting charge ionised in a gas by the passage of a charged particle. Typically the gas is held in a sealed volume, with one or more high voltage sense wires used to collect the charge.

The arrival time of the signal, coupled with the drift velocity of the free electrons in the gas, gives a measurement of the radial distance from the wire at which the charge was created (or the particle traversed the tube). This is called the *drift distance.*

All three layers of the DØ muon system contain drift detectors. The designs of the central and forward system drift detectors differ and are discussed below.

Central Muon Drift Chambers

In the central muon system, the drift chambers hold a row of 24 cells, each with a sense wire running parallel to the magnetic field lines in the toroid magnet. The cells in each chamber have a cross section of approximately 5.5 cm by 10 cm and are approximately 240 cm long. The A-Layer is four chambers deep, with the first chamber lying at $|x| = 297$ cm or $|y| = 297$ cm. The B and C layers are three chambers deep, with the first chamber lying at $|x|$ or $|y| = 445$ cm (B Layer) and $|x|$ or $|y| = 570$ cm (C-Layer). The drift distance in these chambers corresponds to the z coordinate, with expected resolutions of around 0.5 mm. An example cell, with the 3 and 4 chamber assemblies, is shown in figure 5.2.

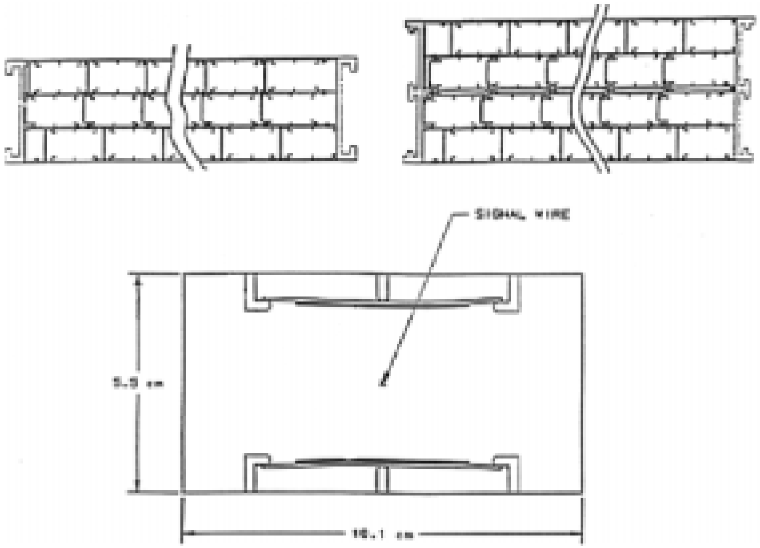

Figure 5.2: An example cell from the central muon drift tubes. The three and four chamber assemblies are shown above.

Neighbouring wires are also joined at one end and read out at the other, allowing an approximate position measurement along the wire (corresponding to the ϕ coordinate) by comparing the signal arrival times from each end. The resolution of this measurement varies with position. If the signal is created far from the readout electronics it travels a comparable distance through both wires and resolutions of around 10 cm are expected. For signals created near the readout electronics on one side, signal dispersion degrades the resolution to around 50 cm. The central muon system drift chambers are discussed in more detail in [25].

Forward Muon Drift Tubes

The forward muon system operates in a significantly higher radiation environment, with muons, beam remnants and hadrons escaping through the calorimeter all contributing. To reduce the dose from beam remnants, shielding has been introduced around the beam pipe.

Even with this shielding, the drift chambers used in the central muon systems would not be able to survive the expected Run II luminosities. So a different design has been chosen, made of individual tubes with a cross section of 1 cm by 1 cm, each holding one sense wire [26]. Each layer is divided into octants, with the tubes in each octant lying approximately along the magnetic field lines in that octant (either x or y, depending on the octant position).

As with the central system, the A-Layer is four layers deep, with the first lying at $|z| = 447$ cm. One layer is shown in figure 5.3. The B and C-Layers are each three layers deep, with the first layer lying at $|z| = 630$ cm (B-Layer) and $|z| = 827$ cm (C-Layer). Drift distance resolutions of approximately 0.7 mm are expected from the forward muon system. No measurement of the coordinate along the sense wires is made by the drift tubes.

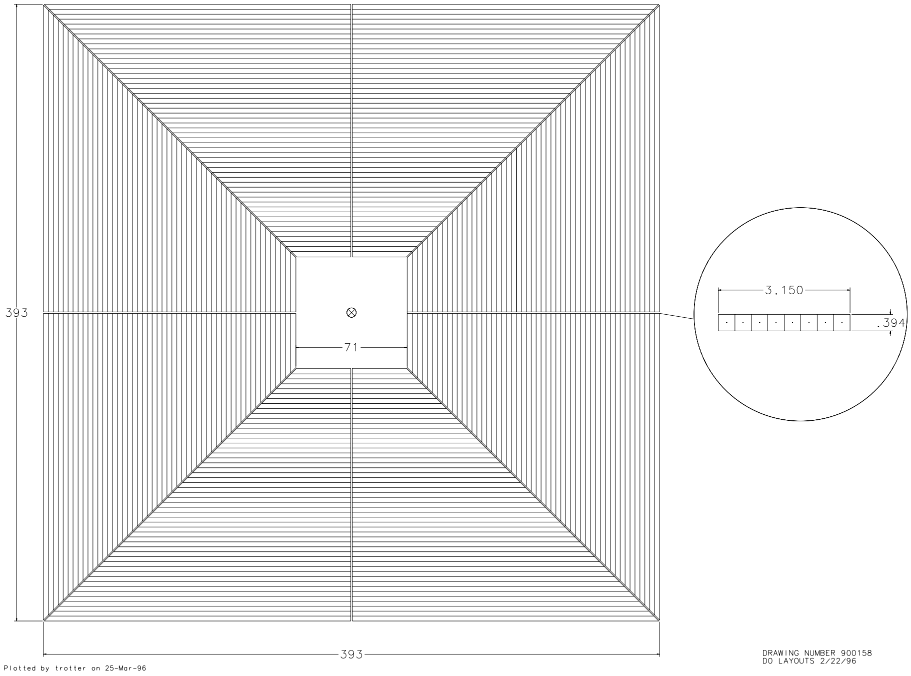

Figure 5.3: A plane of drift tubes used in the forward muon system. Dimensions are given in inches.

5.1.2 Scintillating Pixels

The muon system also contains scintillating pixel detectors [25, 27]. The basic pixel design consists of a slab of scintillator, the surface of which has grooves which hold wavelength shifting readout fibres. Attached to each pixel is a photomultiplier tube, which collects the light from the readout fibres and is connected to readout electronics. The electronics digitise the amplitude and arrival time of the signal from the photomultiplier tubes. Time resolutions of around 2.5 ns are expected, depending on the size of the pixel. A plane of pixels as used in the central muon system is shown in figure 5.4. The pixel arrangement on the forward muon system is visible in figure 5.1.

The pixels also provide a position measurement along the sense wires of the drift chambers. Pixel size is chosen such that each pixel covers a region of approximately

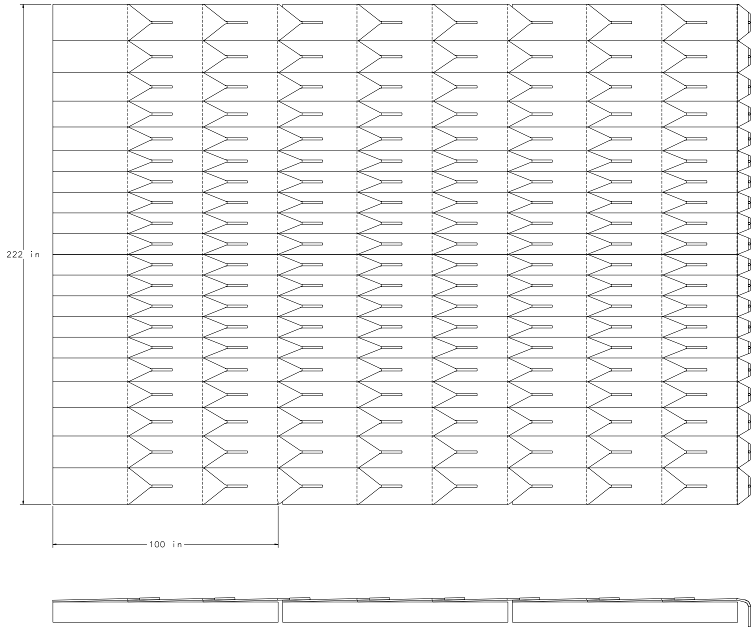

Figure 5.4: A plane of scintillating pixels, as used in the central muon system.

4.5° in ϕ.

The central muon system has scintillators in the A-Layer, lying approximately 10 cm closer to the beam than the drift chambers, and the C-layer, lying approximately 10 cm outside the drift chambers. The forward muon system has scintillators associated with all three layers.

5.1.3 Gap in the Muon System

In the region directly below the calorimeter, only partial coverage by the muon detectors is achieved. Much of the support structure for the DØ detector lies in this region, as well as readout electronics.

While there is some drift chamber and scintillator coverage in the gap region, in the data used for this thesis no muon reconstruction was possible. In detector co-ordinates, the gap extends between $|\eta| < 1.1$ and $4.75 < \phi < 5.25$.

5.1.4 Muon Triggers

Only the Level 1 muon trigger was available when the data used for this thesis were recorded. This was based on a co-incidence of hits in scintillating pixels in two layers of the muon system. The muon detectors are divided into regions (corresponding to the forward and central muon systems) and octants, and to fire the trigger the two hits must lie in the same region and octant.

The scintillating pixels also record a hit time, which is calibrated such that a muon from a pp̄ collision would reach a pixel at a time $t = 0$. A typical A-layer hit time distribution for reconstructed muons is shown in figure 5.5.

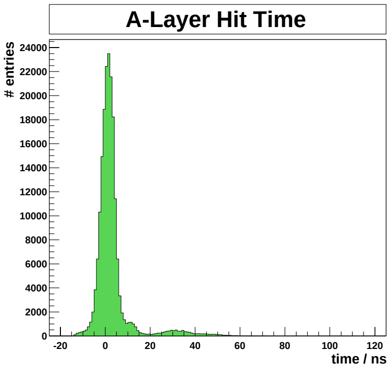

Figure 5.5: The A-layer scintillator hit times for reconstructed muons.

Here, a large peak around zero can be seen, which corresponds to muons from collisions. There is also a bump around 30 ns and a tail to larger positive times, coming mostly from cosmic ray muons. To avoid triggering on out of time muons, a *trigger gate* is defined, allowing only hits with $|\mathrm{t}| < 15$ ns to be used in the trigger.

To further reduce the background contribution from cosmic rays and random hits in the stand-alone muon triggers, the *fast-z* trigger is also required (see section 2.8.1). This is basically an inelastic pp̄ collision trigger based on coincidence of hits in the luminosity monitors either side of the interaction region at DØ.

As there was no Level 2 or 3 filtering available for muons, events passing the Level 1 trigger should automatically have been written to the storage tapes for offline analysis. However, the event rate from the single muon trigger proved too high, so it was *pre-scaled*. A pre-scaled trigger is assigned a pre-scale value, n, then only every n^{th} bunch crossing is allowed to fire this trigger. For the single muon trigger during the data taking period analysed in this thesis, the pre-scale was around 100. The di-muon trigger (requiring two independent single muon triggers and the fast-z trigger), the muon+jet and the muon+electron triggers were not pre-scaled ($n = 1$) and therefore are the triggers used for the analysis described in Chapter 6.

5.2 Muon Reconstruction at DØ

For the purposes of muon reconstruction, the muon detectors are divided into two regions: the A layer before the toroid magnet and the combined B and C layers outside the toroid magnets. Signals from the drift detectors and scintillators in each region are combined into *segments*. Segments are then joined in a fit, with a measurement of the bending in the toroidal magnetic field giving a measure of momentum. A more detailed overview of the muon reconstruction algorithm is given in [56].

5.2.1 Segment Finding

A minimum of two nearby drift detector hits in a region are required to make a segment. The segment itself is the result of a straight line fit through these hits, giving a measurement of both position and direction. Next, a matching scintillating pixel can be added to the segment. The pixels are required to overlap in η with the segment.

5.2.2 Muon Track Fitting

Next, segments from either side of the toroid are combined to form a muon track. Starting in the BC region, a cone in η (the well measured co-ordinate in the drift

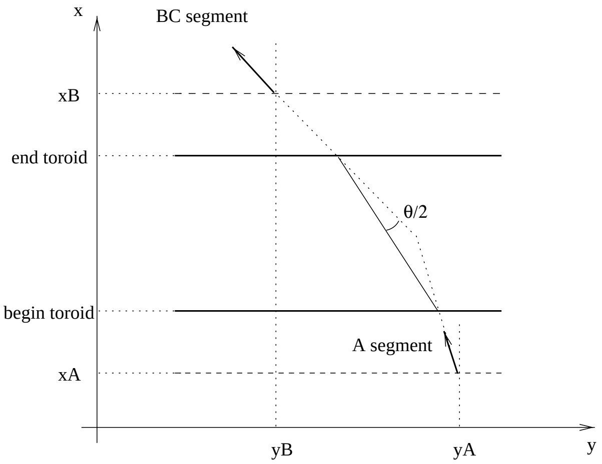

Figure 5.6: Momentum estimation in the muon system. x and y represent the co-ordinates of the bending plane in the toroid magnet

detectors) is extended back to the A layer region. The road is defined by the direction of the BC layer segment in this plane and an opening angle of 0.6 radians. Any A layer segments in this road are used to form muon tracks.

The momentum of a muon track then is estimated using the bending angle, θ, between the A and BC segments in the toroid region. This is illustrated in figure 5.6.

The estimated momentum, p (in GeV), is then given by:

$$p = \frac{0.3 \times B \times s}{|\tan\theta|}. \tag{5.1}$$

where s is the distance travelled in the toroid and B is the toroidal field strength (1.8 T).

This estimated momentum is then used to perform a more accurate fit, in which the BC segment is extrapolated back through the toroid to the A layer, updating the segment and errors for the effects of multiple scattering and energy loss. The A and BC segments are combined to form a matching χ^2, which is then minimised with an iterative procedure, improving the momentum measurement. If this fit does not converge after ten iterations, it is abandoned and the first estimate of the momentum is returned.

5.2.3 Momentum Resolution

The design momentum resolution of the muon system (for fully fitted muons) can be parameterised approximately as:

$$\frac{\sigma_{1/p}}{1/p} \;=\; 0.18 \;+\; 0.005p. \tag{5.2}$$

with p measured in GeV. At low momentum, this is limited by multiple scattering in the iron of the toroid magnet. At high momentum, it is limited by the individual hit resolution. For the data used in this thesis, the momentum resolution was significantly worse, due to calibration and geometry issues.

For the regions with CFT coverage, the central tracking detectors provide a much better measurement of momentum. However in the forward region, with only SMT coverage, the muon system measurement is comparable in resolution.

5.2.4 Muon Identification in the Calorimeter

Muons deposit approximately 2.5 GeV of energy in the calorimeter, through ionisation. Because of the excellent position resolution of the DØ calorimeter, it is possible to reconstruct this 'trail' of energy. Such signals can be used as an independent muon detection method.

A package, MTC (Muon Tracking in the Calorimeter) has been developed at DØ to do this [57]. It uses a histogramming method, storing the energy in each calorimeter cell in arrays indexed by the η and ϕ positions of the cells. Then consecutive layers of cells matching in η and ϕ are combined to form the muon signal. No direct momentum measurement is possible for such 'calorimeter muons'. However, they can be associated with central or muon system tracks, where the momentum is measured.

5.2.5 Muon Isolation

Different muon production mechanisms can result in significantly different experimental signatures, in terms of the properties of the muons themselves and of the other particles produced in the same event. For example, a heavy quark decay can produce a muon as well as hadrons. However, a muon from the decay of a Z^0 boson would generally not have such hadronic activity nearby.

These different signatures are parameterised in terms of *isolation*, which gives a measurement of the activity in the calorimeter near the muon's path. Two isolation definitions are used in this thesis:

- Jet Isolation

  Jet isolation is defined by the angular separation between the path of the muon and the closest reconstructed jet in the calorimeter:

  $$\Delta \mathrm{R}(\mu, \mathrm{jet}) \;=\; \sqrt{\Delta\phi^2 \;+\; \Delta\eta^2}. \tag{5.3}$$

  If ΔR is less than 0.5, the muon is considered non-isolated. If ΔR is greater than 0.5, or no jet is found in the event, the muon is isolated.

- Cone Isolation

  Cone isolation simply sums the energy in calorimeter cells lying in an angular cone around the muon. First, the energy in the electromagnetic layers of the calorimeter in a $\Delta \mathrm{R} < 0.5$ cone around the muon is required to be less than 4 GeV. Second, the energy in the hadronic layers of the calorimeter in a $\Delta \mathrm{R} < 0.5$ cone around the muon is required to be less than 15 GeV. Muons failing these requirements are considered non-isolated.

Isolation proved to be a difficult quantity to define in the early Run II data at DØ, due to poorly understood calorimeter performance. From studies of $Z^0 \rightarrow \mu^+\mu^-$ events, in which both muons are expected to be isolated, the cone isolation performed better than the jet isolation. The actual cut values used for cone isolation followed from these studies.

5.2.6 Muon Quality Definition

The muon reconstruction provides three grades of muon fit quality used in this analysis.

Tight Muon

A tight muon has at least two drift chamber hits in the A layer (which is four chambers deep), as well as a matching scintillator. In the B and C layers, a total of at least three drift chamber hits are required (the B and C layers are each three chambers deep), again with a matching scintillator. Finally, it is required that the track fit converged, giving the best momentum measurement in the muon system.

Medium Muon

The medium muon definition is similar to the tight, except only two drift chamber hits are required in the BC layers. Also, the fit is not required to converge, so medium muons can have a less reliable momentum measurement coming from the first estimation of momentum.

Loose Muon

Loose muons have at least two drift hits in the A layer and at least two drift hits in the BC layer, with no other requirement.

5.2.7 Event Pre-selection

To simplify data analysis, single and di-muon events were pre-selected from the total set of data.

- Single Muon Events

  Events containing at least one tight muon, with a momentum measured in the muon system (*local* momentum) greater then 6 GeV were pre-selected for the single muon data set. This momentum cut was necessary to reduce the data set to a manageable size (less than 1% of the total data set size).

  Single muon events were then separated into isolated and non-isolated subsets, based on the jet isolation definition.

- Di Muon Events

  As there are significantly fewer di-muon events, looser selection criteria could be applied. Events containing at least two medium muons, each with a local momentum greater than 2 GeV were selected. No isolation requirement was used.

5.3 Matching Central Tracks to Muons

As explained in section 4.5.5, the track extrapolation method for matching to muons had to be abandoned in the data used in this thesis.

Instead, to make use of the best measured track in an event, the tracks found by the different stages of GTR before being combined into the final list were used. However, the parameters of these tracks were given only at their point of closest approach (PCA) to (0,0) in x-y, so a method to associate these tracks with muon system information had to be used.

5.3.1 Track Selection

As discussed in section 4.1.2, the following track types were available in early Run II data:

- silicon detector only tracks (at least 4 clusters).

- 8 cluster axial fibre only tracks.
- tracks found in the silicon and extended into the fibre tracker, picking up at least 7 more clusters.
- 16 cluster axial + stereo fibre tracks.
- axial+stereo fibre tracks extended into the silicon detector, adding at least 4 more clusters.

There were approximately equal numbers of silicon only and fibre only tracks. The silicon plus 7 fibre hit tracks were roughly a factor of 10 less common, with the 16 fibre plus silicon tracks being very rare (roughly 1 for every 100 axial fibre only tracks).

Tracks with both silicon and fibre tracker information have the best momentum resolution. However, the tracks found in the fibre tracker and extended into the silicon detector were required to have full axial and stereo fibre information. As the stereo fibres were instrumented only in small regions of ϕ for the data used in this thesis, these tracks were rare.

Of the other types of track, the silicon detector only tracks had very poor momentum resolution and were ignored. Similarly, the tracks found only in the axial fibre layers had limited momentum resolution. When these tracks were extrapolated back to their PCA, the poor curvature measurement was reflected by a poor matching with the beam position. However, by applying a correction to effectively re-fit these tracks through (0,0), the curvature (and hence momentum) measurement was improved. This correction is derived in Appendix B and takes the form:

$$\frac{q}{p_T} = \frac{q}{p_T} - \left(\frac{\sigma_{r,\frac{q}{p_T}}}{\sigma_{\frac{q}{p_T},\frac{q}{p_T}}} \times \frac{r}{16} \right). \tag{5.4}$$

Thus, three track types, all requiring fibre tracker hits, are used as candidates for muon matching. Silicon detector tracks extended into the fibre tracker, axial fibre only tracks (refitted through the origin) and axial plus stereo fibre tracks, extended in the silicon detector. These tracks were required to have a transverse momenta of at least 2 GeV, based on the energy a muon needs to penetrate the calorimeter (around 2.5 GeV).

5.3.2 Track Matching Parameters

As the track parameters are given at the PCA, a simple angular matching method was adopted. The matching is effectively done at the A layer position of the reconstructed muon. The matching parameters chosen were the ϕ residual and η residual between the track and muon at this point:

$$\begin{aligned} \Delta\phi(\mu, \text{track}) &= \phi_{\mu} - \phi_{track}. \\ \Delta\eta(\mu, \text{track}) &= \eta_{\mu} - \eta_{track}. \end{aligned} \tag{5.5}$$

If necessary, $\Delta\phi$ is corrected so that it always lies between -π and π.

The angle ϕ_{track} comes from the direction of the track at PCA, and is corrected to take into account bending in the solenoid field:

$$\phi_{track} = \phi_{track} + 0.3 \times RB\frac{q}{p_T} = \phi_{track} + 0.36\frac{q}{p_T} \tag{5.6}$$

where $R = 0.6$ m, the radius of the solenoid, inside of which it is assumed that there is a constant magnetic field, $B = 2$ T.

For tracks with silicon and fibre tracker information, η_{track} is calculated from the track parameter tanλ. For axial fibre only tracks, no z information is present and the matching can only be carried out in ϕ.

The angle ϕ_{μ} is calculated from x_{μ} and y_{μ}, the position of the muon at the A-layer. In the central muon system, this is taken as the centre of the relevant scintillator rather than the ϕ measurement from the drift chambers. In the forward muon system, the reconstructed segments automatically use the scintillator position.

The muon pseudo-rapidity η_μ is calculated from z_{track}, the z position of the track at PCA, and the position of the muon at the A-layer (x_μ, y_μ, z_μ):

$$\begin{aligned}\theta_\mu &= \text{atan}\left(\frac{\sqrt{x_\mu^2 + y_\mu^2}}{z_\mu - z_{track}}\right), \\ \eta_\mu &= -\ln(\tan(\theta_\mu/2)). \end{aligned} \tag{5.7}$$

The residuals $\Delta\phi$ and $\Delta\eta$ are then calculated for each muon with every track in the event. These are shown in figure 5.7 for the events in the di-muon sample.

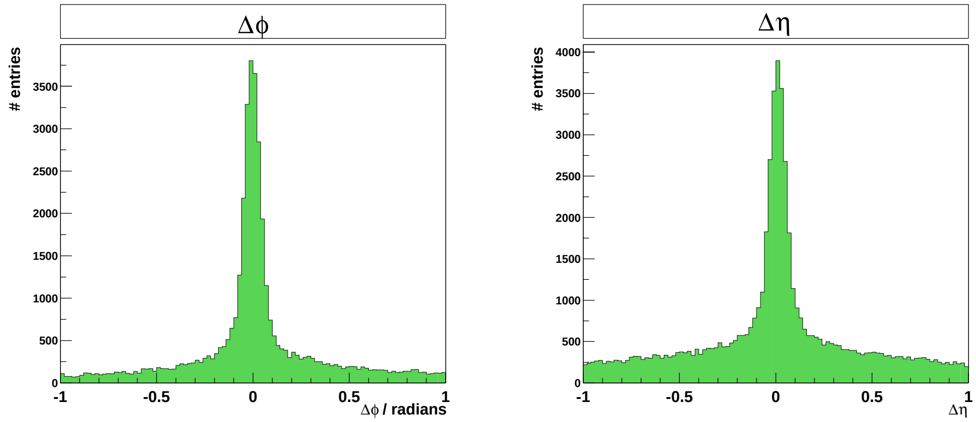

(a) (b)

Figure 5.7: Plots of the (a) ϕ and (b) η residuals, as defined in the text. For each muon, the residuals for every central track are plotted. The peaks show matching tracks

The figures show the matching tracks lie within 0.2 radians in ϕ and 0.2 in η. So, a track match is defined by the following condition:

$$\Delta R = \sqrt{\left(\frac{\Delta\phi}{0.2}\right)^2 + \left(\frac{\Delta\eta}{0.2}\right)^2} < 1. \tag{5.8}$$

For the axial fibre only tracks, ΔR is calculated only from $\Delta\phi$. If such a track is found to match to a muon, it is assigned the z position of the primary vertex (zero if no vertex is reconstructed). The track parameter tanλ is then calculated from this z value and the position of the muon at the A-layer:

$$\tan\lambda \;=\; \frac{z_{\mu} - z_{track}}{\sqrt{x_{\mu}^{2} + y_{\mu}^{2}}}, \tag{5.9}$$

allowing a calculation of the z component of momentum for these tracks.

In the case of two tracks (of any type) matching a muon, the track with the highest transverse momentum is used.

5.3.3 Track Matching Efficiency

The efficiency, ϵ, of this matching can be defined as follows:

$$\epsilon = \frac{\text{number of matched muons}}{\text{total number of muons}}. \tag{5.10}$$

The efficiency as a function of the muon η (from the position of the muon at the A-layer) is shown in figure 5.8 for the all the muons in the pre-selected di-muon sample.

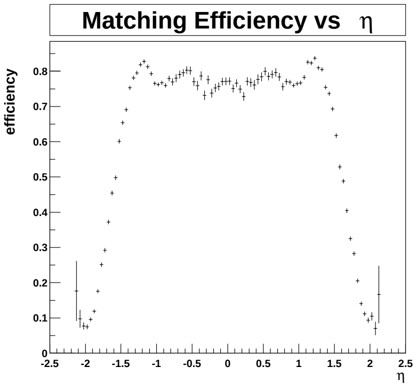

Figure 5.8: The matching efficiency as a function of η. Efficiency is defined in the text.

This efficiency is dominated by the track reconstruction efficiency (rather than failures in track matching). However, it is difficult to interpret directly, as the

the data were taken during a period when the track reconstruction efficiency was changing significantly. The structure in the central η range is caused by detector inefficiencies. The fall above $|\eta| > 1.2$ is due to the fibre tracker acceptance. It is worth noting that without using axial fibre only tracks, the efficiency drops to around 30 %, indicating that the reconstruction efficiency for these tracks is more than double that for tracks with silicon and fibre hits.

This pre-selected di-muon sample is used in the $Z^0 \to \mu^+\mu^-$ analysis in Chapter 6, where a detailed measurement of the track matching efficiency is made.

5.4 The Di-Muon Mass Spectrum

Using the track matching method described in the previous section, it is possible to compare the di-muon mass spectrum obtained with the local muon system and central tracking system.

Figure 5.9 shows the spectrum obtained using the local muon system, requiring two tight muons for the best possible resolution. In the un-like sign charge distribution, a broad peak is visible around the J/ψ resonance (3.1 GeV, all particle masses taken from [11]), with no evidence for other resonances. The like sign distribution gives an indication of the background shape.

Figure 5.10 shows the spectrum obtained when requiring two medium muons, each matched to a central track. The central track momentum is then used to calculate the mass.

In this case, the J/ψ resonance is significantly narrower (around 90 MeV compared to around 1 GeV using the muon system momentum), and the Υ resonances are visible. At this time it is not possible to isolate the 1s (9.46 GeV), 2s (10.0 GeV) and 3s (10.36 GeV) Υ resonances, though this will be possible as the momentum resolution in the central tracking system approaches the design value.

Selecting the events with two muons matched to high transverse momentum (greater than 15 GeV) central tracks highlights the Z^0 resonance (91.18 GeV). This

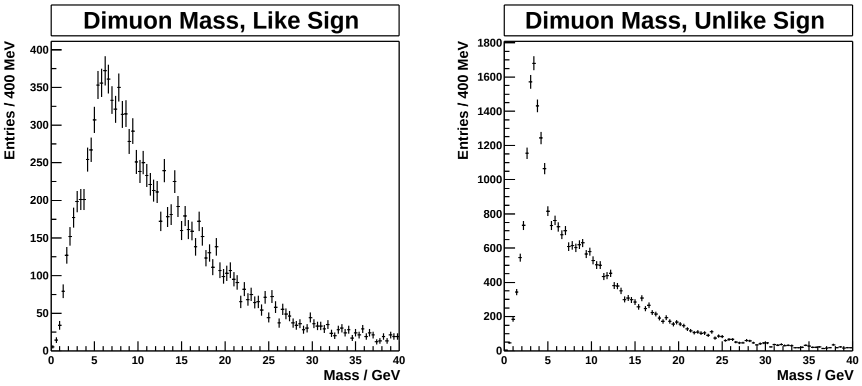

Figure 5.9: Mass plots obtained using the momentum measured in the muon system. A broad J/ψ resonance is visible in the unlike sign charge muon pairs.

sample forms the basis of a preliminary Z^0 cross section × muon branching fraction measurement described in Chapter 6.

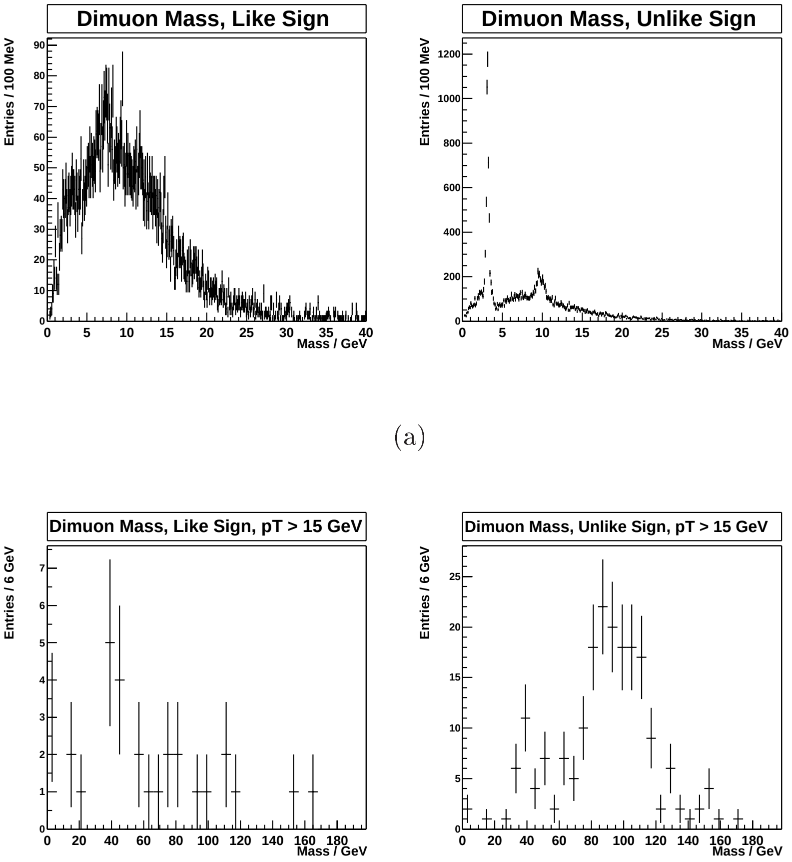

(a)

(b)

Figure 5.10: Plots of the di-muon mass spectrum using the momentum as measured in the central tracking system. The J/ψ and Υ resonances can be seen in figure (a). In (b), tracks with $p_T > 15$ GeV are required and the Z^0 resonance can be seen.

Chapter 6

A Measurement of the Z^0 Boson Production Cross Section

This chapter describes a measurement of the inclusive Z^0 production cross section multiplied by the muon branching fraction in $p\bar{p}$ collisions at a centre of mass energy of 1.96 TeV, using the muon decay channel. The data used for this measurement were recorded during the commissioning phase of DØ, which resulted in some unexpected challenges. However, the completed analysis shows the progress that is being made in understanding of the detector performance and moving from commissioning to physics analysis at DØ.

The first stage in the analysis is to isolate the $Z^0 \to \mu^+\mu^-$ signal. To do this, event selection cuts are applied to a data sample corresponding to a total integrated luminosity available, $\mathcal{L}$, giving a total number of candidate events, N_{ev}. Also, the number of background events (i.e. not the signal of interest), N_{bg}, which may have passed the selection cuts must be estimated. Then, the probability of a $Z^0 \to \mu^+\mu^-$ event to pass these cuts, ϵ, must be measured, in order to determine the total number of $Z^0 \to \mu^+\mu^-$ events which actually occurred.

The inclusive Z^0 production cross section (σ_Z) multiplied by the muon branching fraction (B_μ), can then be extracted from the following equation:

$$\sigma_{\mathrm{Z}} \times B_{\mu} = \frac{\mathrm{N}_{\mathrm{ev}} - \mathrm{N}_{\mathrm{bg}}}{\epsilon \times \mathcal{L}}. \tag{6.1}$$

The event selection and estimates of the backgrounds are described in section 6.1. The event selection efficiency measurement is somewhat complicated, and split into two main components. The first takes into account the event trigger and muon reconstruction efficiencies, which are measured in data and described in section 6.2. The second includes the detector coverage, or *acceptance* and central track reconstruction efficiency, as well as some kinematic effects of the event selection cuts. These are measured with simulated events, tuned to match the data, as described in section 6.3.

These two components are combined into the overall event selection efficiency in section 6.4. Section 6.5 covers the integrated luminosity in the sample and the cross section measurement is presented in section 6.6. Finally, section 6.7 covers some improvements which can be made to this analysis with more recent data.

6.1 Event Selection and Backgrounds

The signature of a $\mathrm{Z}^0 \rightarrow \mu^+\mu^-$ event is two high energy, unlike sign muons. When the data used for this thesis were taken, the main trigger for these events was the di-muon trigger, so part of the event selection is to require that this trigger fired.

The muons themselves are required to be isolated (using the cone isolation described in section 5.2.5) and reconstructed in the DØ muon system with at least medium quality (see definition in section 5.2.6). To accurately reconstruct the Z^0, the momentum measurement of the central tracking system is required. Central tracks are associated with the muons using the method described in section 5.3.

Therefore, the event selection cuts used are as follows:

- Pre-selected di-muon sample (see section 5.2.7).
- Di-muon trigger fired.

- Two isolated (cone isolation) medium quality muons.
- Two matching central tracks, unlike sign charges, each hits in all 8 CFT layers and transverse momentum > 20 GeV.
- $\Delta\mathrm{R}(\mu,\mu) = \sqrt{\Delta\phi(\mu,\mu) + \Delta\eta(\mu,\mu)} > 2$.
- A-layer scintillator hit time difference between muons < 12 ns.

These cuts are explained in more detail in sections 6.1.1 to 6.1.4, along with estimates of the backgrounds. Figure 6.1 shows the invariant mass and transverse momentum (p_T) distributions of muons in the events passing the selection cuts. The masses fall in a broad peak around the Z^0 resonance (91 GeV) and all events are considered as $\mathrm{Z}^0 \rightarrow \mu^+\mu^-$ candidates. There are five 'overflow' events in figure 6.1(a), which have masses in the range 200 – 300 GeV. Looking at all other parameters in these events, they appear consistent with $\mathrm{Z}^0 \rightarrow \mu^+\mu^-$ events in which one track is mis-measured, so are not excluded from the sample. Therefore the total number of $\mathrm{Z}^0 \rightarrow \mu^+\mu^-$ candidate events is 137.

6.1.1 Kinematic Cuts

To illustrate the effectiveness of the track momentum and ΔR cuts, the following distributions show the events remaining after applying every selection cut *except* that on the plotted parameter.

Figure 6.2 shows the transverse momentum of the lowest momentum muon in each event. Significant numbers of like-sign events have $p_T < 20$ GeV, indicating that this cut is very effective in rejecting background events.

Figure 6.3 shows the ΔR distribution from unlike sign events, indicating that the Z^0 decays generally produce back-to-back muons. One of the three events failing the ΔR cut has a mass of around 80 GeV, so may be a $\mathrm{Z}^0 \rightarrow \mu^+\mu^-$ event. The probability for a $\mathrm{Z}^0 \rightarrow \mu^+\mu^-$ event to fail the p_T or ΔR cuts is measured in section 6.3.

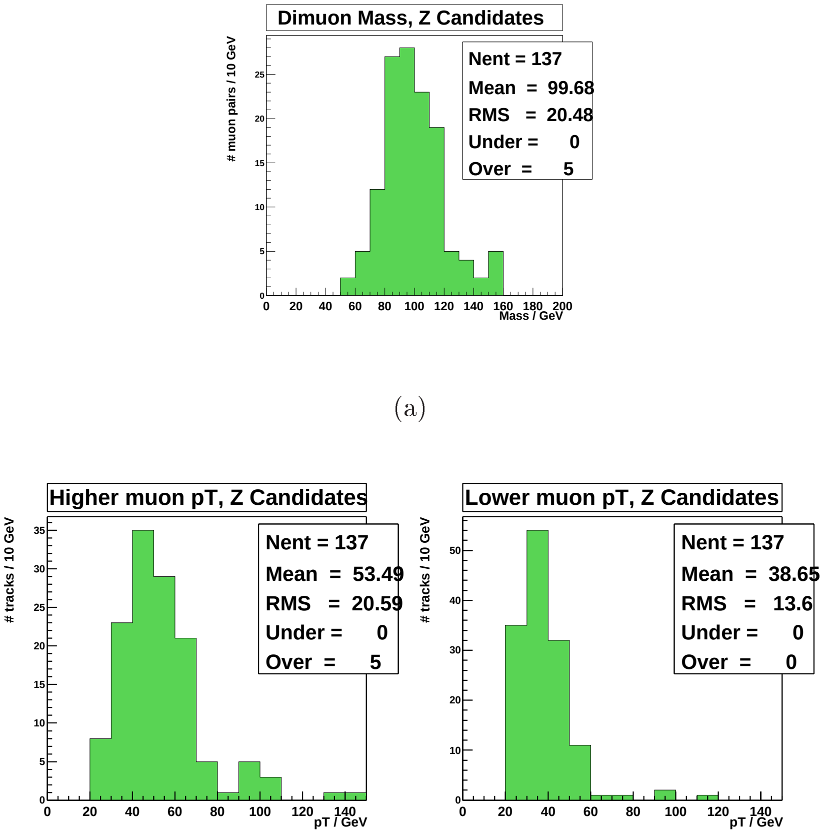

(a)

(b)

Figure 6.1: The (a) invariant mass distribution and (b) muon p_T distributions of events passing the $Z^0 \to \mu^+\mu^-$ selection cuts.

6.1.2 Muon Isolation and Heavy Quark Backgrounds

One of the main backgrounds to $Z^0 \to \mu^+\mu^-$ events is muons from the decay of heavy quarks, such as $b\bar{b} \to \mu^+\mu^- +$ hadrons. It is also possible for hadrons escaping from the calorimeter to produce hits in the muon detectors (‘punch-through’), giving a ‘fake’ muon signal. In both of these cases, the muons or punch-through tend to be close to hadronic activity in the calorimeter, so these events can be rejected by the isolation requirements.

Cone isolation was defined in section 5.2.5 as:

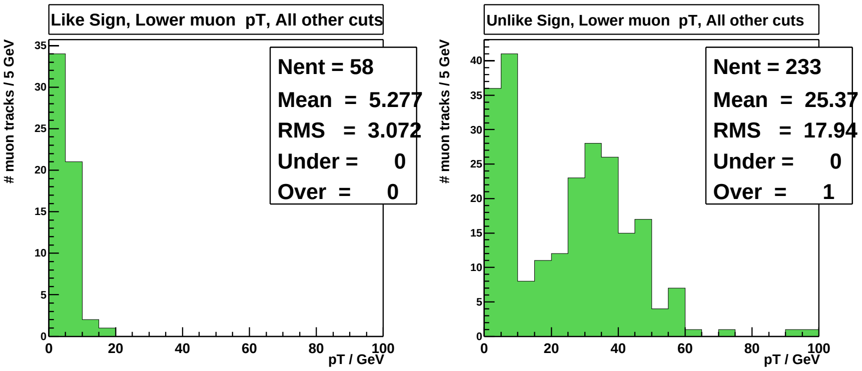

Figure 6.2: The transverse momentum distribution of the lowest energy muon with all other Z^0 event selection cuts applied.

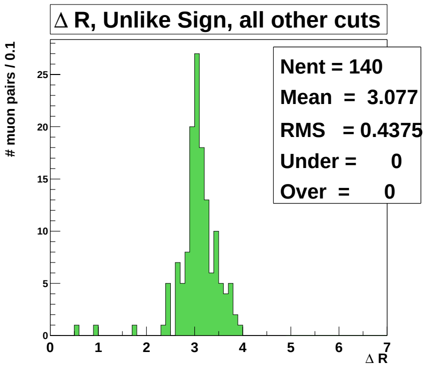

Figure 6.3: The ΔR distribution with all other Z^0 event selection cuts applied.

- Less then 4 GeV in the electromagnetic calorimeter in a $\Delta R < 0.5$ cone around the muon.
- Less then 15 GeV in the hadronic calorimeter in a $\Delta R < 0.5$ cone around the muon.

This gives two isolation requirements on each muon, four in total on a di-muon event.

Applying all the Z^0 event selection cuts except the isolation highlights the effectiveness of this cut. Figure 6.4 shows the resulting mass distributions for events which pass four, three and two of the cone isolation requirements. The mass distributions are split into like and unlike sign charges, with the sign coming from the central tracks associated with the muons.

It can be seen that requiring three or four of the cone isolation cuts gives samples of Z^0 candidates with no like sign events, indicating that there is little background. Requiring only two of the four isolation cuts results in some like sign events and two additional unlike sign events. Allowing more isolation requirements to fail results in an additional 6 like sign events and 4 unlike sign events.

Thus, events were required to pass at least three of the four cone isolation requirements to enter the final sample of 137 events. The lack of unlike sign events outside the Z^0 peak region and the absence of like sign events indicates that there is little background after applying the isolation (and all other event selection cuts). Therefore the heavy quark and punch-through backgrounds are assumed to be negligible.

One of the unlike sign events failing the isolation requirements has a mass in the Z^0 range and may be a $Z^0 \rightarrow \mu^+\mu^-$ event. The efficiency of the isolation requirements, ϵ_{iso}, is therefore estimated as:

$$\epsilon_{iso} = \frac{137}{137+1} = 0.99 \pm 0.01 \tag{6.2}$$

6.1.3 Scintillator Timing and Cosmic Ray Backgrounds

The other main background to di-muon events are muons from cosmic ray activity. Such muons are produced with a wide range of energies high in the atmosphere and can pass through the DØ detector at any time.

Hit time information from the muon scintillators is used to reject such events. For a cosmic ray muon to simulate a di-muon event, it must pass through the detector and be reconstructed in the muon system as it enters and exits. However, as the perpendicular distance between opposite central muon A-layer detector planes is around 6 m, it takes around 20 ns to traverse this distance. Di-muons produced

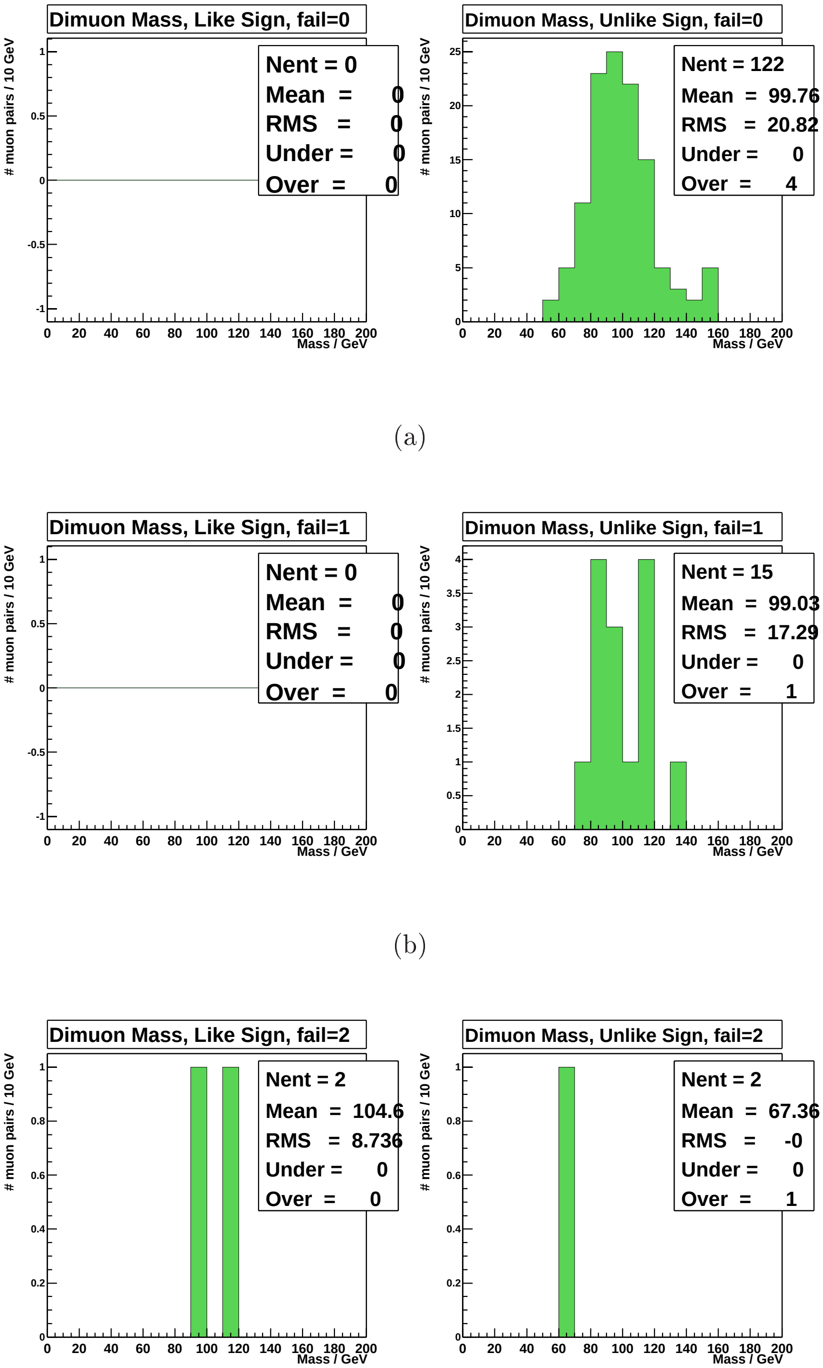

(a)

(b)

(c)

Figure 6.4: Invariant mass distributions applying all Z^0 event selection cuts and (a) four, (b) three and (c) two of the cone isolation cuts.

in p$\bar{\text{p}}$ collisions will reach the A-layer at approximately the same time, as shown in figure 6.5.

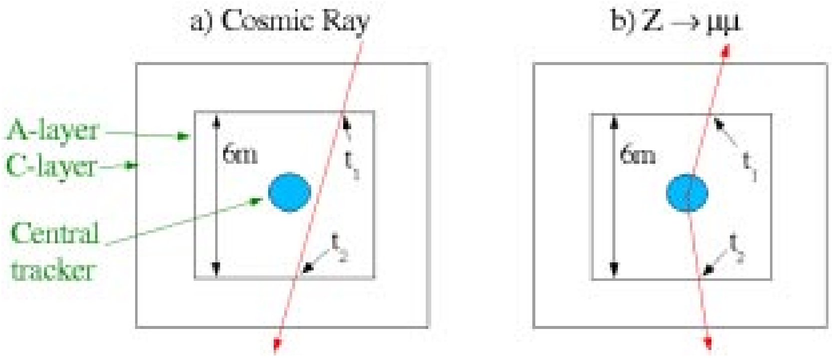

Figure 6.5: The hit times, t_1 and t_2, used to separate cosmic rays from $\text{Z}^0 \rightarrow \mu^+\mu^-$ events.

Therefore, in di-muon events the A-layer scintillator hit time difference, $\Delta\text{t} = \text{t}_1 - \text{t}_2$, can be used to reject cosmic rays. Figure 6.6 shows this time difference for all di-muon events in the pre-selected di-muon sample, and those events remaining after applying all the $\text{Z}^0 \rightarrow \mu^+\mu^-$ event selection criteria *except* the timing cut.

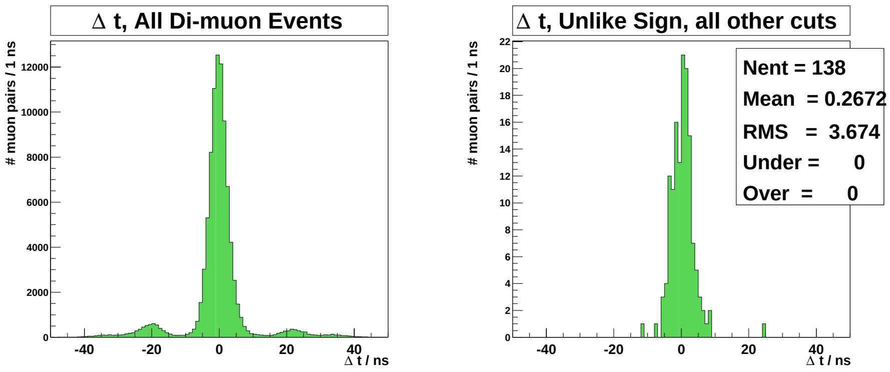

(a) (b)

Figure 6.6: A-layer scintillator hit time difference in di-muon events. Figure (a) has no cuts applied, figure (b) has all Z^0 selection cuts applied apart from the timing cut.

The cosmic ray muons are clearly visible in figure 6.6(a) as an accumulation around ±20 ns. However, as can be seen in figure 6.6(b), most are rejected by the Z^0 selection cuts, with two cuts giving most of the rejection. Firstly, requiring the di-muon trigger, as the 20 ns time difference means that cosmic ray muons generally enter or exit the detector outside the trigger gate (which is around 15 ns wide) and cannot fire the di-muon trigger. Secondly, requiring matching tracks also rejects cosmic ray muons. Unless such a muon passes very close to the interaction region at DØ, it is unlikely to find reconstructed tracks to match the muon system hits.

From the distribution in figure 6.6(b), it can be seen that one unlike sign cosmic ray muon event (reconstructed with a mass around 40 GeV) is rejected (no like sign events fail only the timing cut). Therefore it is assumed that the timing cut is 100% efficient, rejecting no Z^0 events. One unlike sign cosmic ray muon event (reconstructed with a mass around 40 GeV) is rejected, with no like sign events failing only the timing cut. There remains one unlike sign event close to the cut at -12 ns, which may be due to a mis-calibrated pixel or may be a cosmic ray muon. The total number of cosmic ray background events in the final sample is therefore estimated as 1 ± 1.

6.1.4 Other Backgrounds

There are two other backgrounds to $Z^0 \rightarrow \mu^+\mu^-$ events: Drell-Yan muon production and $Z^0 \rightarrow \tau^+\tau^- \rightarrow \mu^+\mu^-\nu_\tau\bar{\nu_\tau}\nu_\mu\bar{\nu_\mu}$. The contributions from these sources to the final sample are estimated in this section.

Drell-Yan Muon Production.

Drell-Yan muon production has contributions from $q\bar{q} \rightarrow Z^0 \rightarrow \mu^+\mu^-$, $q\bar{q} \rightarrow \gamma^* \rightarrow \mu^+\mu^-$, and Z^0/γ^* interference. This analysis attempts to isolate the Z^0, so the photon and interference contributions are considered as backgrounds.

The Drell-Yan contribution to the final sample is estimated in simulated events.

Two samples of 200,000 events are generated using the Pythia event simulation: one of pure Z^0 production (referred to as the 'Z' sample); one of Z^0+ $Z^0\gamma^*$ + Z^0/γ^* interference (referred to as the 'Drell-Yan' sample). From these samples, events are selected which produce two muons inside the detector acceptance (defined in sections 6.2.1 and 6.3.1). The standard kinematic cuts used in the final event selection are then applied:

- Both central tracks reconstructed with $p_T > 20$ GeV.
- $\Delta R(\mu, \mu) > 2$.

Figure 6.7 shows the di-muon mass distributions for events inside the detector acceptance for the two samples before and after applying the kinematic cuts. The two samples are then scaled to correspond to the same luminosity, which involves multiplying the number of events in the Drell-Yan sample by a factor of 4.195.

The Drell-Yan background contribution ($\mathrm{bg}_{\mathrm{dy}}$) is then estimated from the fraction of additional events in the Drell-Yan sample (taking the number of entries in figures 6.7(b) and 6.7(d)):

$$\mathrm{bg}_{\mathrm{dy}} = \frac{15788 \times 4.195 - 60312}{60312} = 0.0981 \pm 0.0012, \tag{6.3}$$

where the uncertainty is calculated as a binomial error once the numerator has been evaluated.

A background fraction of 0.0981 corresponds to 13.4 background events in the final sample of 137 events defined in section 6.1. By comparing with the mass distribution in figure 6.7(b) or 6.7(d) with that found in data (see figure 6.1(a)) it can be seen that the detector simulation carried out on the Pythia event simulation is not realistic. However, the Drell-Yan distribution is not changing very rapidly at the 40 GeV lower mass limit forced by the kinematic cuts (see figure 6.7(c)), so additional smearing due to poorer resolution should not be a large effect. Still, an uncertainty of ±2 events is assigned to the background estimate to cover any effect arising from the unrealistic detector simulation.

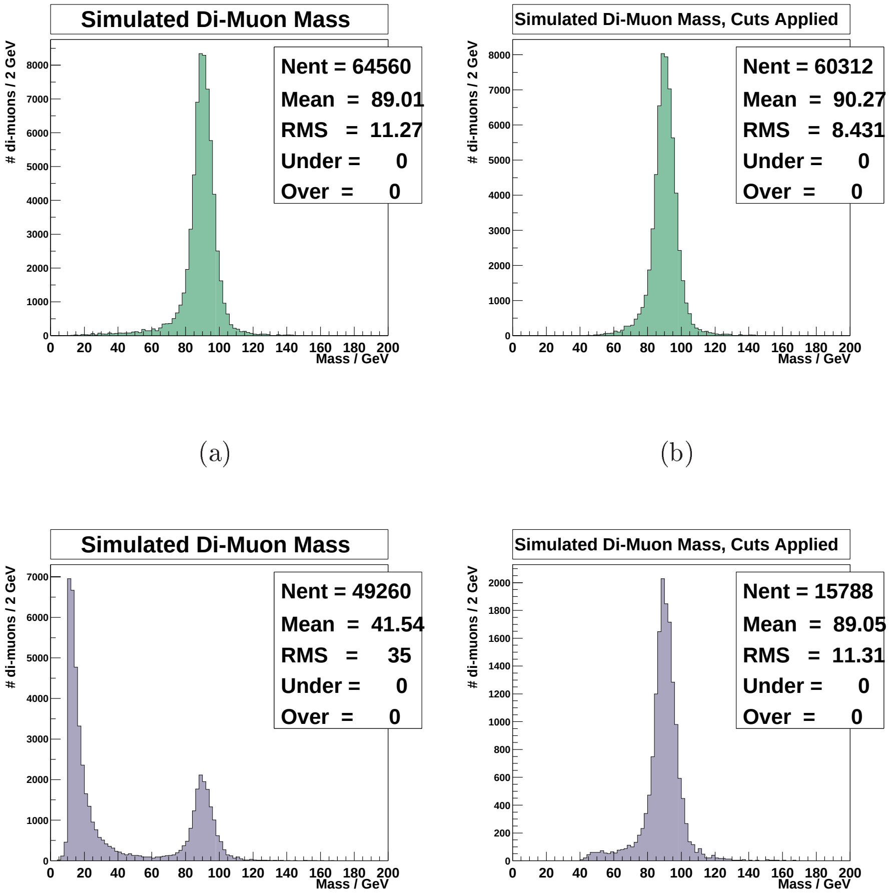

(a) (b)

(c) (d)

Figure 6.7: Di-muon mass distributions: the Z sample without the kinematic cuts (a) and with the cuts (b); the Drell-Yan sample without the kinematic cuts (c) and with the kinematic cuts (d). Samples are defined in the text.

Di-Muons From $\mathbf{Z^0 \rightarrow \tau^+\tau^-}$.

The final background considered is from $Z^0 \rightarrow \tau^+\tau^- \rightarrow \mu^+\mu^-\nu_\tau\bar{\nu_\tau}\nu_\mu\bar{\nu_\mu}$, which can produce two unlike sign, isolated muons. The Z^0 branching fraction to $\tau^+\tau^-$ is approximately the same as the branching fraction to muons, and the τ branching fraction to muons is around 17%. However, the resulting muons have a much softer momentum spectrum due to the presence of the neutrinos. To check the probability for a $Z^0 \to \tau^+\tau^-$ event to pass the $Z^0 \to \mu^+\mu^-$ event selection, a sample of 25,000 $Z^0 \to \tau^+\tau^-$ events were generated using the Pythia event simulation. From these events, 269 (1.1%) give two muons inside the detector acceptance (defined in sections 6.2.1 and 6.3.1). Figure 6.8 shown the di-muon mass and muon transverse momentum distributions for these 269 events, using the generated muon momenta (no detector simulation).

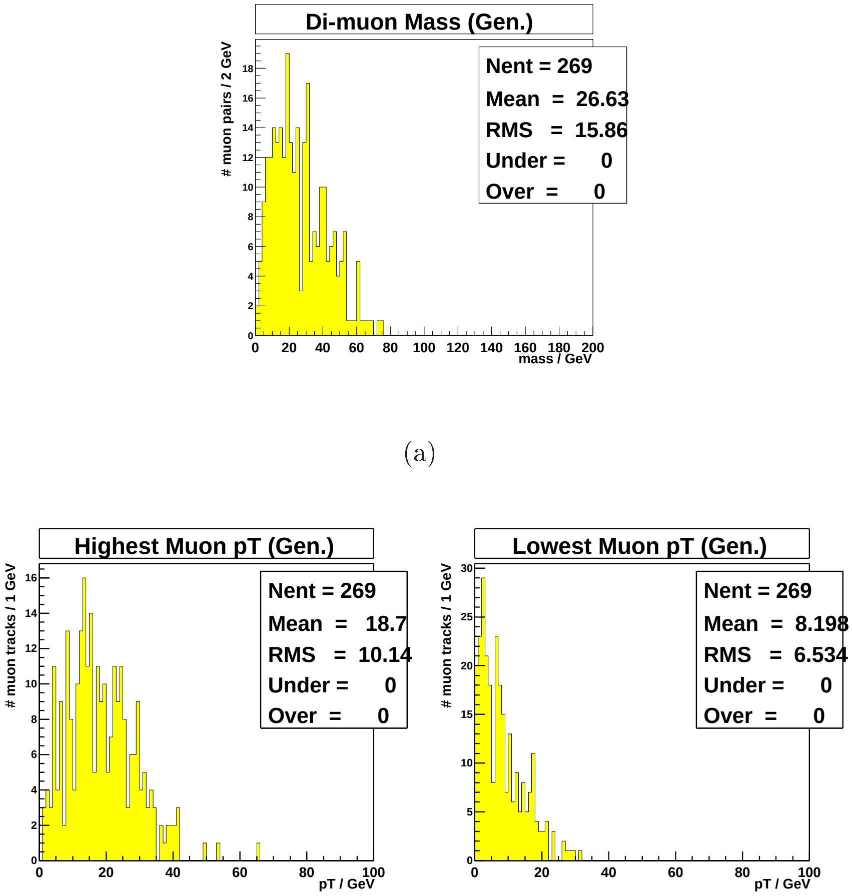

(a)

(b)

Figure 6.8: Plots of (a) the di-muon mass and (b) p_T distributions for simulated $Z^0 \to \tau^+\tau^-$ events in which both taus decay to muons. The generated muon momenta are used, with no detector simulation.

Only 16 events produce two muons with $p_T > 20$ GeV. Using this to calculate the background fraction bg_τ:

$$\mathrm{bg}_\tau = \frac{16}{25000} = 0.00064, \tag{6.4}$$

shows that the $Z^0 \to \tau^+\tau^-$ background in the final sample is negligible.

The contributions from all background sources are summarised in table 6.1 and the total is estimated as 14.4 ± 3 events in the final sample.

Background Source	Number of Events
Drell-Yan	13.4
Cosmic Rays	1
Heavy Quark Decays and Punch-through	Negligible
$Z^0 \to \tau^+\tau^-$	Negligible

Table 6.1: A summary of background contributions to the final $Z^0 \to \mu^+\mu^-$ sample.

6.2 Muon Trigger and Reconstruction Efficiency

The next stage in the analysis is to measure the probability for a $Z^0 \to \mu^+\mu^-$ event to pass the event selection cuts. This section contains a measurement of the trigger and reconstruction probabilities for muons which pass through the muon detectors. To measure these, it is necessary to define the muon detector acceptance, which is done in section 6.2.1. Then, the following probabilities are measured in data:

- z, the probability for a $Z^0 \to \mu^+\mu^-$ event to fire the fast-z trigger (required as part of the di-muon trigger).
- S, the probability for a muon (inside the muon system acceptance) to produce hits in the muon system scintillators.
- T, the probability for a muon that has produced hits in the muon system scintillators to fire the muon trigger.

- M, the probability for a muon in a $Z^0 \to \mu^+\mu^-$ event (in which the di-muon trigger fires) to be reconstructed with at least medium quality.

The final $Z^0 \to \mu^+\mu^-$ event selection for the cross section measurement requires the di-muon trigger and two reconstructed muons, which can be expressed in terms of these probabilities as $z(STM)^2$.

Ideally, z, S, T and M should be measured in $Z^0 \to \mu^+\mu^-$ events. For example, the probability to reconstruct a low momentum muon from a J/ψ decay may be significantly different from the probability to reconstruct a high momentum muon from a Z^0 decay. However, due to the large pre-scale on the single muon trigger in the data used, the majority of $Z^0 \to \mu^+\mu^-$ events are recorded only when the di-muon trigger fires.

As a result, the di-muon trigger efficiency is measured first. This requires the fast-z trigger and two muons which produce hits in scintillators and fire the muon trigger, which can be expressed as $z(ST)^2$. The measurements of z, T and S are described in sections 6.2.2 to 6.2.4. T is measured before S due to some of the complications in the methods that had to be adopted. Then, in a sample of $Z^0 \to \mu^+\mu^-$ events which fire the di-muon trigger, the muon reconstruction efficiency is measured, as described in section 6.2.5.

The individual probabilities are combined into the di-muon reconstruction probability, defined as $z(STM)^2$ in section 6.2.6.

6.2.1 Muon System Acceptance

The muon system acceptance is found by looking at the positions of medium quality muons reconstructed in data, plotted as ϕ against η in figure 6.9 for the pre-selected di-muon sample.

Here, it can be seen that the muon system coverage extends to around $|\eta| = 2$, but the acceptance is defined as $|\eta| < 1.9$ to ensure full coverage in ϕ. The gap in the central muon system is also visible, extending between $4.25 < \phi < 5.15$ for

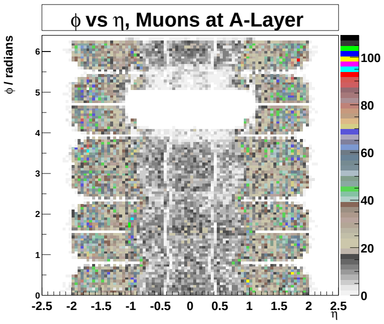

Figure 6.9: ϕ vs η for reconstructed medium quality muons at the A-Layer.

$|\eta| < 1.1$. This acceptance definition is used for the efficiency measurements and as part of the overall detector acceptance for $Z^0 \to \mu^+\mu^-$ events, measured in section 6.3.5.

6.2.2 Fast-z Trigger Efficiency, z

The fast-z trigger is based on a coincidence of hits in the DØ luminosity monitors and is required as part of the single and di-muon triggers. The probability for the fast-z to fire may depend on the type of process that occurs in a $p\bar{p}$ collision. To avoid any bias, $Z^0 \to e^+e^-$ events, in which the underlying event is phenomenologically identical to $Z^0 \to \mu^+\mu^-$ events, are used to measure z. The fast-z trigger is not required as part of the electron trigger, so z can be extracted directly from the fraction of $Z^0 \to e^+e^-$ events in which the fast-z trigger fires.

To select $Z^0 \to e^+e^-$ events, two reconstructed electrons are required (electron selection cuts are defined in [61]) with energy greater than 20 GeV. The electrons are required to be back to back ($\Delta R(e, e) > 2$).

This selection gives 91 events from the same data taking runs as the di-muon data used in the cross section analysis. As shown in figure 6.10, the sample is further purified by cutting on the reconstructed mass, M, requiring $60 < M < 110$.

Of the remaining 76 events, 71 fire the fast-z trigger, giving the fast-z efficiency

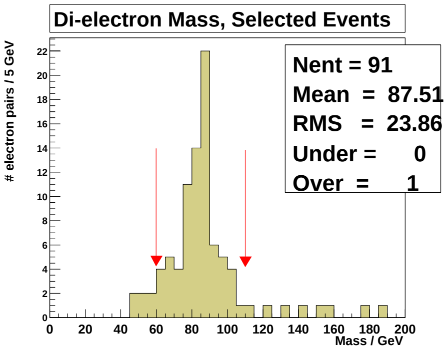

Figure 6.10: Invariant mass of electron pairs used for the fast-z efficiency measurement. The red arrows indicate the mass cut values used to isolate the Z^0 signal.

to be:

$$z = \frac{71}{76} = 0.934 \pm 0.028. \tag{6.5}$$

This takes into account the hardware efficiency and the geometric acceptance of the fast-z trigger for Z^0 events.

6.2.3 Muon Trigger Efficiency, T

Due to the large pre-scale on the single muon trigger at the time the available data were recorded, $Z^0 \rightarrow \mu^+\mu^-$ events were generally only recorded if the di-muon trigger fired. Therefore, the muon trigger efficiency has to be measured with a different type of event.

The approach adopted is to use heavy quark or similar events which can contain two leptons of different flavour. Events are then selected on the presence of an electron trigger and an offline muon. Then, the fraction of these events which also fire the muon+electron trigger can be used to measure the muon trigger efficiency.

The event selection requirements for this measurement are:

- Level 1 15 GeV electron trigger fired.

- Offline medium quality muon with matching 5 GeV central track.
- A-Layer scintillator hit time of the muon is inside trigger gate ($|\mathrm{t}| < 5$ ns).
- No other muon of any quality in the event.

When the data used for this measurement were taken, the 15 GeV electron trigger was not pre-scaled and automatically passed Level 2 and Level 3.

Medium quality muons are required to have scintillator hits, so the scintillator efficiency must be measured separately. Attempts to measure the muon trigger efficiency for loose muons (no scintillator hits required, see loose definition in section 5.2.6) suffered from cosmic ray contamination, with around 10% of the reconstructed muons lying outside the trigger gate. The timing cut on the medium muon, track match requirement and second muon veto all reject cosmic ray backgrounds, at the expense of requiring the muon scintillator hits.

The event selection yields a sample of 518 events. The 'test' trigger is then the muon+5 GeV electron Level 1 trigger, which was also un-prescaled and automatically passed Level 2 and 3. The electron component of this trigger automatically fires (as the 15 GeV electron trigger is required), so it only depends upon the efficiency of the muon trigger. The muon+electron trigger fired in 446 of the 518 events.

The muon trigger efficiency (given scintillator hits), T, is then given by:

$$T = \frac{446}{518} = 0.861 \pm 0.015. \tag{6.6}$$

6.2.4 Muon Scintillator Efficiency, S

For the muon trigger efficiency measurement, scintillator hits were required as part of the event selection. Therefore, it is necessary to measure the probability for a muon, within the muon system acceptance, to produce hits in the muon system scintillators. To do this, it is necessary to select events containing muons without requiring scintillator hits - i.e. without requiring a muon trigger.

In fact, di-muon events which fire a single muon trigger are used. As the stand-alone single muon trigger was heavily pre-scaled, the Level 1 muon+jet[1] trigger is the best choice, being un-prescaled and automatically passing Level 2 and Level 3. As a result of using this trigger, the scintillator efficiency is measured mostly with heavy quark events. Such events are not guaranteed to contain two muons, so two reconstructed muons have to be required as part of the event selection, which is:

- Pre-selected single muon sample.
- Level 1 muon+jet trigger fired (jet $E_T > 5$ GeV).
- Control muon: tight quality muon passing the pre-selection requirements, matched to a central track with transverse momentum > 5 GeV. A-layer scintillator hit time inside trigger gate ($|t| < 5$ ns).
- Test Muon: loose quality muon, matched to a central track with $p_T > 5$ GeV

This selection gives a sample of 297 events. The track matching is required to provide cosmic ray muon rejection, as no timing cut can be placed on the test muon. Studies on the hit time of the control muon and, if scintillator hits are present, the test muon, indicate that there is negligible cosmic ray contamination remaining in this sample.

The aim is to extract the scintillator efficiency from the fraction of test muons with matching scintillator hits. However, a problem was found in the muon reconstruction in certain parts of the detector, resulting in scintillator hits not being picked up even though they were present. Such reconstruction failures will be taken into account in the muon reconstruction efficiency, M, described in section 6.2.5.

---

[1] Unlike the stand-alone muon triggers, the muon+electron and muon+jet triggers do not require the fast-z trigger to also fire.

Therefore, to avoid double-counting this inefficiency, a different approach is necessary.

Having already measured the probability for a muon with scintillator hits to fire the trigger, the number of selected events in which the di-muon trigger fires (194) can be used to extract the probability that the test muon produced scintillator hits.

To see this, some algebra is required to clear up an ambiguity – if the test muon does produce scintillator hits, it is not clear which muon actually fired the muon+jet trigger. Therefore the probability that the muon+jet trigger fires has two factors. The first is the simple case in which the control muon fires the muon+jet trigger (and there is no requirement on the test muon producing scintillator hits). There is also the possibility that the control muon does not fire the muon+jet trigger (in which case the test muon must have scintillator hits and fire the trigger). These can be expressed as:

$$\text{Muon} + \text{jet probability} = ST + S(1-T) \times ST = ST(1+S-ST). \tag{6.7}$$

where T is the efficiency for a muon with scintillator hits to fire the muon trigger (measured in section 6.2.3) and S is the probability for a muon to produce scintillator hits.

The probability for two muons to produce hits in the scintillators and fire the di-muon trigger is $z(ST)^2$, where z is the fast-z trigger efficiency measured in section 6.2.2. Thus, the fraction, of events in which the di-muon trigger fires, F, is given by:

$$F = \frac{z(ST)^2}{ST(1+S-ST)} = \frac{194}{297} = 0.653 \pm 0.028. \tag{6.8}$$

Rearranging gives:

$$S = \frac{F}{zT + FT - F} = 0.915 \pm 0.062. \tag{6.9}$$

6.2.5 Muon Reconstruction Efficiency, M

Having measured the probability for a muon to produce scintillator hits and fire the muon trigger, it is now necessary to measure the probability that this muon is also reconstructed offline. For this measurement, $Z^0 \rightarrow \mu^+\mu^-$ events can be used. These events are identified based on the presence of the di-muon trigger and requiring one reconstructed muon in the muon detectors. Then, the other muon in each event contributes to an unbiased sample of high energy muons which can be used to measure the reconstruction efficiency.

The pre-selected single isolated muon sample is used (see 5.2.7), which requires a tight quality, isolated (jet isolation) muon with transverse momentum, as measured in the muon system (*local* p_T) > 6 GeV. In each pre-selected event, the muon which passed the pre-selection is identified and cuts are applied to isolate the $Z^0 \rightarrow \mu^+\mu^-$ signal.

The event selection is then:

- Pre-selected single isolated muon sample (see 5.2.7).
- Di-muon trigger fired.
- Control muon: Muon passing the pre-selection requirements, isolated (cone isolation), matched to central track with transverse momentum > 20 GeV.
- Test Muon: Isolated (cone isolation) calorimeter muon, matched to a central track with transverse momentum > 20 GeV, lying within the muon system acceptance.
- ΔR between the tracks > 2.

The cone isolation (2 requirements on each muon) and central track kinematic cuts reject non-Z^0 events.

The muon reconstruction efficiency, M, is then measured on a muon-by-muon basis. Both muons in each event are checked to see if they pass the 'test' requirements and are back-to-back with a 'control' muon. A total of 146 test muons are found, coming from 109 events.

As part of M, it is also possible to measure the probability for a $Z^0 \rightarrow \mu^+\mu^-$ event to pass the di-muon pre-selection (the sample used for the cross section measurement). To enter the di-muon sample, an event must contain two muons of at least medium quality with local $p_T > 2$ GeV. Therefore, M is taken as the fraction of test muons which have a matching medium muon with local $p_T > 2$ GeV. Of the 146 test muons, 113 have such a matching muon.

As two central tracks are required as part of the event selection, the purity of events used to measure M can be checked by plotting the invariant mass, as shown in figure 6.11. It can be seen that there are no like sign events and the unlike sign events appear to be pure Z^0 candidates.

The muon reconstruction efficiency, M, is then:

$$M = \frac{113}{146} = 0.774 \pm 0.035. \tag{6.10}$$

As part of M, four sources of inefficiency are taken into account:

- Muon system drift chamber coverage and efficiency (within acceptance).
- Medium quality muon reconstruction efficiency (given scintillator hits).
- Local $p_T > 2$ GeV (as required by the di-muon pre-selection).
- Central track matching efficiency (given the central track).

6.2.6 Di-Muon Identification Efficiency

The probability for a $Z^0 \rightarrow \mu^+\mu^-$ event to fire the di-muon trigger and have both muons reconstructed can now be calculated. This includes:

- The fast-z trigger efficiency, $z = 0.934 \pm 0.028$.
- The probability that a muon (within the muon system acceptance) will hit scintillators: $S = 0.915 \pm 0.062$.

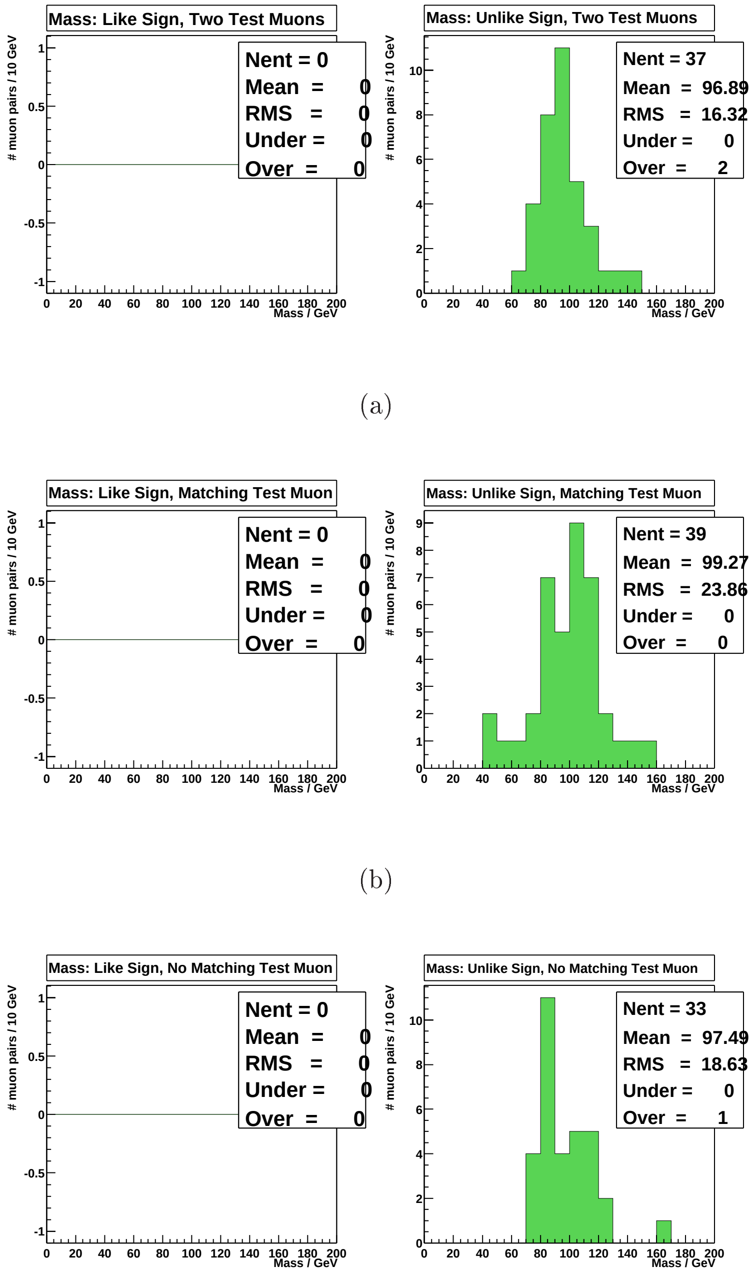

(a)

(b)

(c)

Figure 6.11: Invariant mass distributions from the muon reconstruction efficiency sample. Figure (a) shows the events containing two test muons, (b) the events with one test muon and a matching medium muon (c) the events with one test muon without a matching medium muon.

- The probability that a muon which hit scintillators fires the muon trigger: $T = 0.861 \pm 0.015$.
- The probability that a muon which fires the trigger to be reconstructed with at least medium quality and correctly matched to the central track: $M = 0.774 \pm 0.035$.

The di-muon identification efficiency is then defined as $\epsilon_{\mu\mu} = z(STM)^2$. However, rather than using the calculated value and error for S, the correct final uncertainty is more easily obtained if $\epsilon_{\mu\mu}$ is expressed in terms of the four statistically independent quantities, z, T, F and M:

$$\epsilon_{\mu\mu} = \frac{z(FTM)^2}{(zT + FT - F)^2} = 0.348 \pm 0.049. \tag{6.11}$$

Given that S and T were not measured in $\mathrm{Z}^0 \to \mu^+\mu^-$ events, there may be a bias due, for example, to the softer momentum spectrum of muons in heavy quark events. However, the systematic uncertainty is large enough to cover the effects of such a bias.

6.3 Acceptance and Tracking Efficiency

When measuring the muon trigger and reconstruction probabilities, central tracks were always required. The next step in the analysis is therefore to measure the track reconstruction efficiency for $\mathrm{Z}^0 \to \mu^+\mu^-$ events. To do this, it is first necessary to define the tracking detector acceptance, which is done in section 6.3.1. The efficiency is then measured in data, with the method described in section 6.3.2.

The final part of the event selection efficiency is to find the fraction of $\mathrm{Z}^0 \to \mu^+\mu^-$ events which fall outside the detector acceptance or fail the track p_T and $\Delta\mathrm{R}$ cuts. This is measured in simulated $\mathrm{Z}^0 \to \mu^+\mu^-$ events, which are described in section 6.3.3. The simulation is tuned to reproduce the tracking efficiency and momentum resolution obtained in data. To test the agreement, the tuned simulation and data are compared in section 6.3.4. Finally, the effects of the detector acceptance and kinematic cuts are extracted from the tuned simulation in sections 6.3.5 and 6.3.6

6.3.1 Tracking Detector Acceptance

The acceptance of the tracking detectors at DØ varies as a function of the z position of the interaction, as shown in figure 6.12.

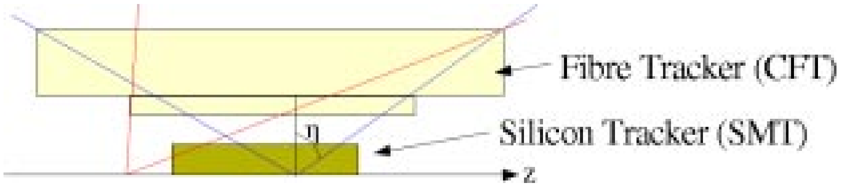

Figure 6.12: The dependence of the tracking detector acceptance on the z position of the interaction.

As all tracks used to match to muons are required to have fibre tracker hits, the acceptance is limited by the fibre tracker geometry. Most tracks are required to have hits in all eight layers of the fibre tracker with no silicon detector hits required (see section 4.1.2). However, as the track reconstruction code requires hits in only seven out of eight fibre layers for tracks found in the silicon tracker, the acceptance for these tracks is slightly larger.

Rather than defining different acceptances for different tracks, an eight hit fibre track is required when matching to a muon. This track requirement was used when defining the sample of 137 events for the cross section measurement and in all efficiencies measured so far in this analysis. An additional 9 Z^0 candidates have at least one track being found only as a 7 fibre layer (with silicon hits) track. Regaining only these 9 events was not considered worth the complication and extra systematic uncertainty of two tracking acceptance definitions and calculations.

The tracker acceptance is then defined simply by the geometry of the fibre tracker, with the positions and lengths of the first, second and eighth fibre layers limiting the acceptance. The first and second layers are 166 cm long, centred at $z = 0$ and lying at radii of 19.5 and 23.4 cm. The eighth layer is 257 cm long, again centred at $z = 0$, lying at a radius of 51.5 cm. A particle which passes through these three layers is defined as lying inside the tracker acceptance. All muons with a matching eight fibre layer track are assumed to lie within the acceptance.

6.3.2 Tracking Efficiency in Data

The track reconstruction efficiency is measured in $Z^0 \to \mu^+\mu^-$ events. A sample of $Z^0 \to \mu^+\mu^-$ events is identified requiring only one track, then the number of times the second track is found gives the tracking efficiency.

However, identifying $Z^0 \to \mu^+\mu^-$ events based only on one track is difficult, as the second p_T cut usually rejects many background events (see figure 6.2). The event selection used is as follows:

- Di-muon trigger fired.
- Primary vertex reconstructed.
- Control Muon: Isolated medium quality muon, matched to a central track with transverse momentum > 30 GeV.
- Test Muon: Isolated medium quality muon inside the tracker acceptance and with local $p_T > 8$ GeV.
- $\Delta\phi(\mu, \mu) > 2.6$.

The primary vertex is required to give a measurement of the z coordinate of the interaction and allow the tracking acceptance to be applied to the test muon. Compared to the standard $Z^0 \to \mu^+\mu^-$ event selection based on events with two tracks, a harder cut is placed on the p_T of the control muon (> 30 GeV compared to > 20 GeV), the ΔR cut is replaced by a harder cut on $\Delta\phi(\mu, \mu)$ and a cut is made on the test muon local p_T. These changes are required to reject non-Z^0 background events.

The tracking efficiency is then measured on a muon-by-muon basis. Both muons in each event are checked to see if they passes the 'test' requirements and are back-to-back with a 'control' muon. This yields a sample of 145 test muons, coming from a total of 107 $\mathrm{Z}^0 \rightarrow \mu^+\mu^-$ candidate events. Of these test muons, 127 have a matching track. No cut can be placed on the momentum of this track, as obviously no such cut can be applied to the events in which no matching track is found.

The tracking efficiency, ϵ_{tr}, is therefore found to be:

$$\epsilon_{tr} = \frac{127}{145} = 0.876 \pm 0.027. \tag{6.12}$$

In making this measurement, it is assumed there is no correlation between the reconstruction probabilities for the two tracks in each event. Preliminary studies in the $\mathrm{Z}^0 \rightarrow e^+e^-$ events indicate that this is a valid assumption [62].

In section 6.3.4 this tracking efficiency is included in the event simulation and comparisons made between the simulation and data. First, section 6.3.3 gives an overview of the simulation used.

6.3.3 Event Simulation

A sample of 0.5 million $\mathrm{Z}^0 \rightarrow \mu^+\mu^-$ events were generated with WZGEN [63], a vector boson generator used during Run I at DØ. Rather than simulating the full $\mathrm{p\bar{p}}$ collision, WZGEN simply generates W or Z bosons with a distribution of momenta and collision z. The momentum distribution is derived from the theoretical calcuation of the differential Z^0 cross section in parton-parton collisions. The inputs to this calcuation are parton distribution functions tuned with Run I data. For Run II, the 160 GeV increase in centre of mass energy has been taken into account and the z distribution of Z^0 production is smeared to match the 25 cm spread in the interaction region. The output from WZGEN is simply the four-vectors of the muons resulting from the Z^0 decay. No underlying event simulation is done.

To simulate the detector response to those muons, the ‘fast’ simulation, PMCS, is used (see section 2.9.1). This ‘smears’ the generated momenta by the expected detector reconstruction resolution, which in this case is the central tracking system resolution.

The design resolution of the central tracking system where there is full SMT and CFT coverage can be parameterised as:

$$\frac{\Delta p_T}{p_T} = \sqrt{0.015^2 + (0.0014 p_T)^2}. \tag{6.13}$$

To match the width and shape of the J/ψ and Z^0 mass peaks found in the data used in this thesis, the constant term was multiplied by a factor of 2.9 and the momentum dependent term by a factor of 1.8 [40]. An overall shift in momentum was also observed in the data, which is due to the value assumed for the central tracking field strength at the time. To compensate for this, the smeared momenta in the simulated events were multiplied by a factor of 1.09. The mass and momentum distributions for the generated and smeared muons are shown in figure 6.13.

When carrying out the smearing, PMCS removes muons with $|\eta| > 3$, resulting in some events being lost, as can be seen in the number of entries in the histograms in figure 6.13.

To provide some basic cross-checks of the WZGEN events, in particular for the effects of detector acceptance, 7500 events were also generated using Pythia [37]. Rather than simulating pure Z^0 production, Pythia models the full $\mathrm{p\bar{p}}$ collision and also includes the γ^* and Z^0/γ^* interference contributions to Drell-Yen muon production. To isolate the Z^0 events, the generated mass is required to be between 80 and 100 GeV, giving a sample of 6261 events. The detector simulation carried out on the Pythia events did not reflect the status of the actual detector at the time, so was not used.

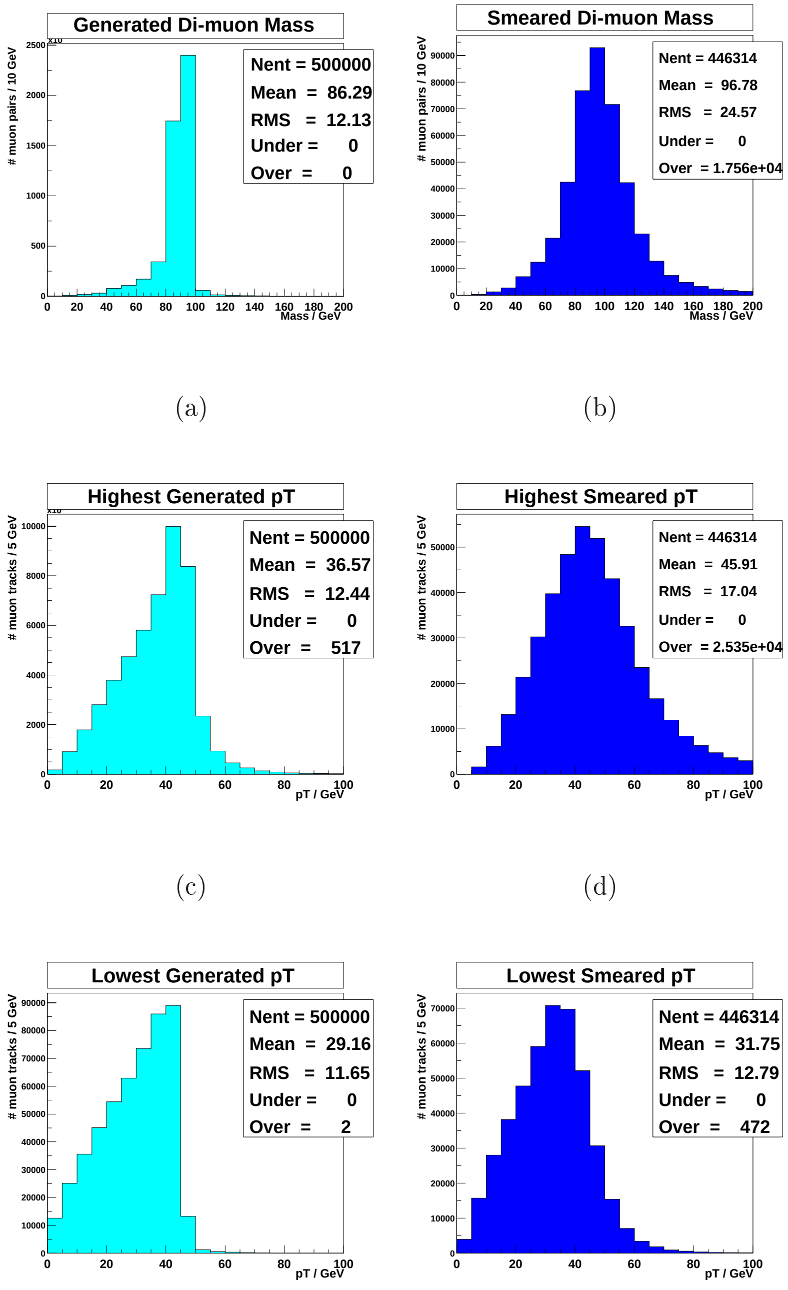

(a) (b)

(c) (d)

(e) (f)

Figure 6.13: The generated (light blue) and smeared (dark blue) mass distributions (a and b) and momentum distributions (c–f) from the WZGEN $Z^0 \rightarrow \mu^+\mu^-$ events.

6.3.4 Data - Simulation Comparison

To include the track reconstruction efficiency in the PMCS simulation, a fixed 'reconstruction probability' is assigned for each central track from a muon to be reconstructed. This reconstruction probability is set to the value measured with data in section 6.3.2 (0.876 ± 0.027) and a random number (taken from a uniform distribution between 0 and 1) is used to decide if each simulated muon was found. The reconstruction probability is set to 0.876 for comparisons with the data, but is varied by $\pm 1\sigma$ to estimate uncertainties in section 6.3.6.

To test the agreement between the event simulation and data, the data measurement of tracking efficiency is reproduced as closely as possible in the simulated events:

- Two muons inside tracking and muon system acceptances.
- One muon with (smeared) transverse momentum > 30 GeV.
- $\Delta\phi(\mu, \mu) > 2.6$.

By looking at the fraction of events in which a second muon is found, the tracking efficiency of 0.876 is recovered. The simulated events are then scaled to contain the same total number of events as the data and the mass and momentum distributions found in the data and simulation can be compared.

Figure 6.14 shows the transverse momentum distributions of the control track in the events where the test muon does ('two track' events) and does not ('one track' events) have a matching track. Also, the invariant mass and transverse momentum distributions of the test track are shown for the cases where a matching track is found. These show reasonable agreement between the simulation and data. Some overflow entries are visible in the data, indicating that a small number of tracks (around 2%) are being badly mis-measured. This is not reflected in the simulation.

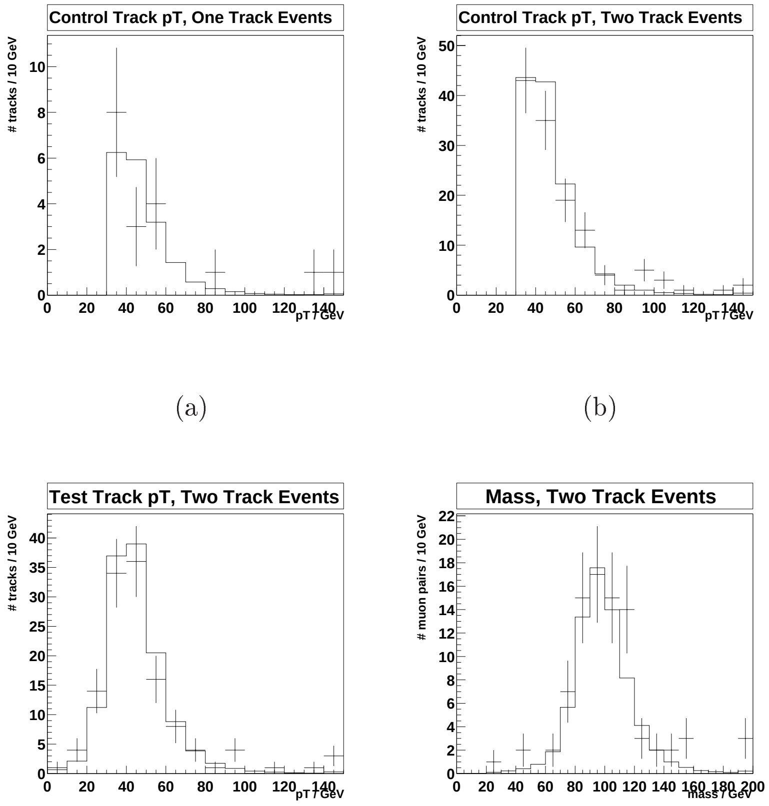

(a) (b)

(c) (d)

Figure 6.14: Comparison between the data (points with errors) and simulation (solid line) from the samples used for the tracking efficiency study. Overflows are summed and shown in the final bin of each histogram.

To further test the agreement, a cut can be placed on the transverse momentum of the test track and the distributions compared again. With cuts at 10, 20 and 30 GeV, these distributions are shown in figure 6.15.

These again show reasonable agreement between the simulation and data, other than the overflows. Thus the simulation provides a generally realistic description of the data, and can be used to measure the probability for a $Z^0 \rightarrow \mu^+\mu^-$ event to lie within the detector acceptance and pass the kinematic selection cuts. An uncertainty will be added to this probability to cover the additional 2% of mis-measured tracks

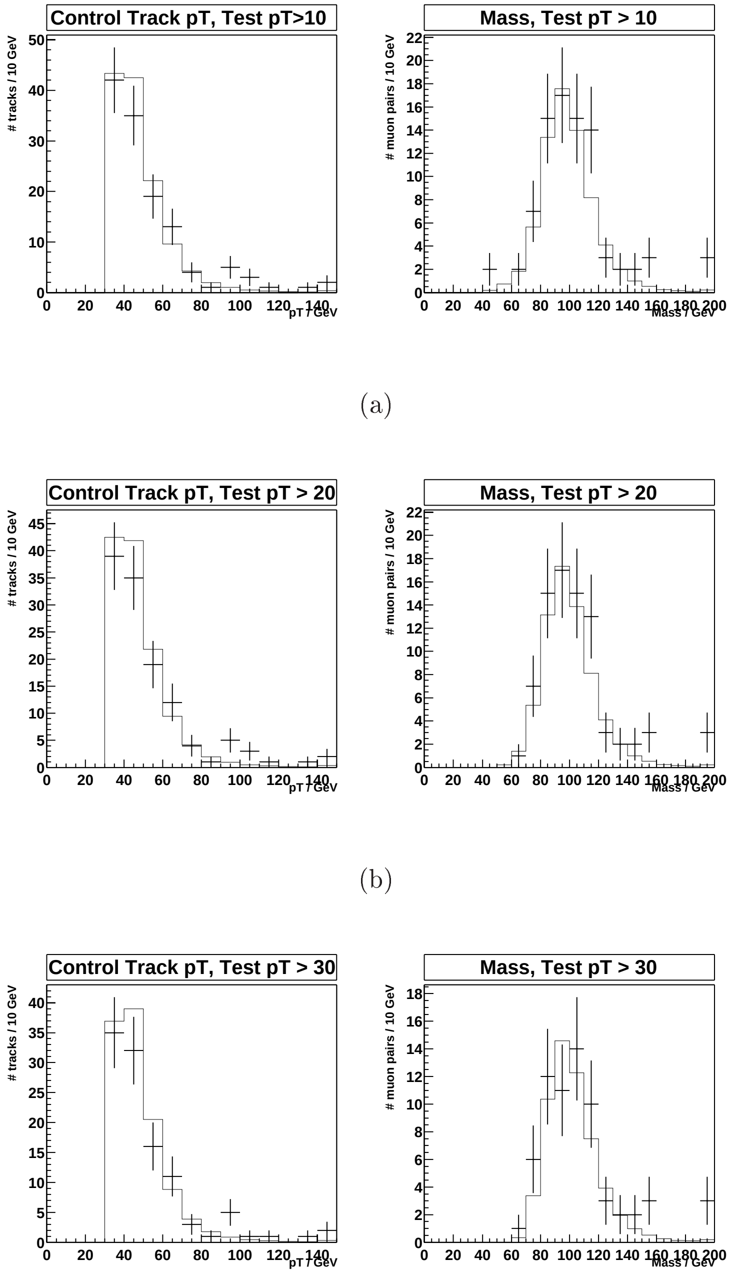

(a)

(b)

(c)

Figure 6.15: Comparison between the data (points with errors) and simulation (solid line) for the two track events from the samples used for the tracking efficiency study. A cut of (a) 10, (b) 20 and (c) 30 GeV is placed on the test track. Overflows are summed and shown in the final bin of each histogram.

found in the data but not in the simulation.

6.3.5 Total Acceptance for $Z^0 \to \mu^+\mu^-$ Events

Applying the definitions of the tracking and muon system acceptances to the simulation, it is possible to measure the fraction of $Z^0 \to \mu^+\mu^-$ events which produce two muons lying within the detector acceptance.

For this measurement, only the generated muons are used, with no detector simulation. In the WZGEN events, the fraction of events inside the acceptance is 0.343. In the Pythia events, this fraction is 0.362. Therefore, the acceptance for $Z^0 \to \mu^+\mu^-$ events, $\mathcal{A}$, is taken to be between the Pythia and WZGEN values, with the difference being assigned as an uncertainty:

$$\mathcal{A} = 0.353 \pm 0.010. \tag{6.14}$$

6.3.6 Tracking Efficiency and Kinematics

Finally, the probability for a $Z^0 \to \mu^+\mu^-$ event to pass the p_T and ΔR event selection cuts is measured in the tuned simulation.

The following selection is applied to the 0.5 million simulated $Z^0 \to \mu^+\mu^-$ events:

- Two muons inside tracker and muon system acceptance.
- Both central tracks reconstructed with $p_T > 20$ GeV.
- $\Delta\mathrm{R}(\mu, \mu) > 2$.

The momentum and mass distributions obtained with these cuts can be compared with the distributions found in data to give another cross check of the simulation. Figure 6.16 shows the result of this comparison, with the distributions from the simulated data scaled to contain the same number of events as the data distributions. Again, there is reasonable agreement between the simulation and data.

The measured efficiencies from the simulated events are:

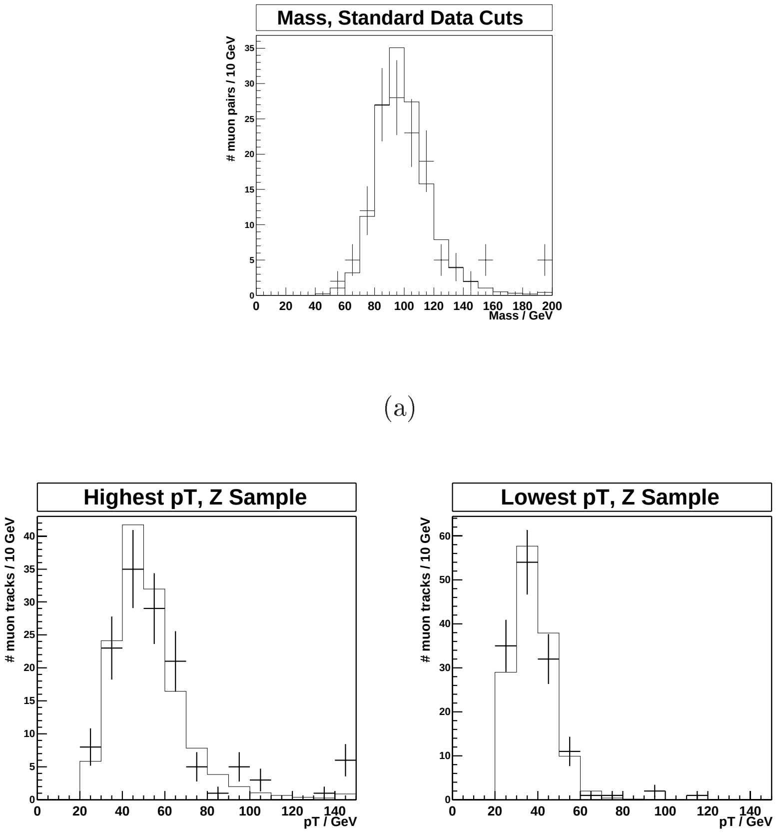

(a)

(b)

Figure 6.16: Comparisons between the data (points with errors) and simulation (solid line) using the $Z^0 \rightarrow \mu^+\mu^-$ event selection cuts.

- Fraction events with two tracks, both reconstructed with $p_T > 20$ GeV $= 0.718 \pm 0.060$.
- Fraction of events passing the p_T cut with $\Delta R(\mu, \mu) > 2 = 0.992$.

The uncertainty on the tracking efficiency is derived by adjusting the track reconstruction efficiency used in the event simulation by $\pm 1\sigma$ of the data value (see section 6.3.2), with a further 2% added to cover the additional mis-measurement effect observed in data (see section 6.3.4). The statistical uncertainty on the ΔR

cut efficiency is negligible and it is assumed there is no systematic uncertainty on this efficiency. The combined efficiency of the kinematic cuts, ϵ_{kin} is:

$$\epsilon_{kin} = 0.718 \times 0.992 = 0.712 \pm 0.060. \tag{6.15}$$

6.4 Event Selection Efficiency

It is now possible to combine all the efficiencies into a total event selection efficiency, ϵ. This has four components:

$$\epsilon = \text{Isolation} \times \text{Muon ID} \times \text{Acceptance} \times \text{Tracking} \tag{6.16}$$

The isolation efficiency was estimated in section 6.1.2 as 0.99 ± 0.01. The di-muon identification efficiency of 0.348 ± 0.049 includes the scintillator, drift chamber and di-muon trigger efficiencies. The acceptance was found to be 0.353 ± 0.010. The tracking efficiency of 0.712 ± 0.06 includes track reconstruction efficiency as well as the momentum and ΔR cuts.

The overall $Z^0 \rightarrow \mu^+\mu^-$ event selection efficiency is then:

$$\epsilon = 8.67 \pm 1.43\ \%. \tag{6.17}$$

6.5 Integrated Luminosity

The number of p$\bar{\text{p}}$ collisions occurring in DØ is measured by recording hit coincidences in the luminosity monitors either side of the interaction region (see section 2.4). To convert this to an integrated luminosity, the inelastic p$\bar{\text{p}}$ cross section within the luminosity monitor acceptance is required. This has yet to be measured in Run II, but extrapolating from the Run I value (base on very similar luminosity monitor acceptance), a value of:

$$\sigma = 43 \pm 4 \text{ mb} \tag{6.18}$$

is used [62]. Due to the preliminary nature of the calibration and efficiency studies for the luminosity monitors, a conservative 10% systematic error is assigned.

The data used for this analysis were recorded in the period between mid March and early May 2002. During this time, the di-muon trigger was operational when an integrated luminosity of $4.57 \pm 0.46\ \mathrm{pb}^{-1}$ was recorded by DØ.

6.6 Extracting the Z^0 Cross Section

Returning to the inclusive Z^0 production cross section formula,

$$\sigma_Z \times B_\mu = \frac{\mathrm{N}_{\mathrm{ev}} - \mathrm{N}_{\mathrm{bg}}}{\epsilon \times \mathcal{L}} \tag{6.19}$$

all the components have now been measured and the cross section can be extracted. Based on a sample of 137 events containing 14.4 ± 3 background events, the cross section is found to be:

$$\sigma_Z \times B_\mu = 309\ \pm\ 31\ (\mathrm{stat})\ \pm\ 51\ (\mathrm{sys})\ \pm\ 31\ (\mathrm{lum})\ \mathrm{pb}. \tag{6.20}$$

The uncertainties are summarised in table 6.2, with the di-muon identification presents the largest uncertainty. The complicated methods used to obtain this can certainly be improved in the future, once the un-prescaled single muon triggers become available.

Combining all the uncertainties in a quadratic sum gives:

$$\sigma_Z \times B_\mu = 309\ \pm\ 67\ \mathrm{pb}. \tag{6.21}$$

The $\mathrm{Z}^0 \to \mu^+\mu^-$ branching fraction measured at LEP (see, for example, [11]) can also be used to extract the Z^0 production cross section from the cross section × branching fraction measurement. Taking:

$$\mathrm{BF}(\mathrm{Z}^0 \to \mu^+\mu^-) = (3.366 \pm 0.007)\% \tag{6.22}$$

the production cross section is found to be:

Factor	Uncertainty (%)
Di-muon Identification	14
Luminosity	10
Statistics	9.9
Tracking	8.3
Acceptance	2.7
Isolation	0.7

Table 6.2: A summary of the uncertainties in the $Z^0 \to \mu^+\mu^-$ cross section measurement.

$$\sigma(\mathrm{p\bar{p}} \to \mathrm{Z}^0 + \mathrm{X}) = 9190 \pm 1990 \text{ pb.} \tag{6.23}$$

For comparison, the cross section in the electron channel has also been measured in Run II at DØ [62]:

$$\sigma_Z \times B_e = 266 \ \pm\ 20 \text{ (stat)} \ \pm\ 20 \text{ (sys)} \ \pm\ 27 \text{ (lum) pb.} \tag{6.24}$$

It can be seen that the results are consistent within the experimental uncertainties. This is expected from the very similar electron and muon branching fractions of the Z^0 measured at LEP. The Run I measurements from CDF and DØ and the Run II electron and muon measurements from DØ are summarised in figure 6.17. The Run I DØ measurements of the Z^0 production cross section in the muon and electron channels are [58]:

$$\begin{aligned} \sigma_Z \times B_\mu &= 178 \ \pm\ 22 \text{ (stat)} \ \pm\ 21 \text{ (sys)} \ \pm\ 9 \text{ (lum) pb,} \\ \sigma_Z \times B_e &= 218 \ \pm\ 8 \text{ (stat)} \ \pm\ 8 \text{ (sys)} \ \pm\ 12 \text{ (lum) pb.} \end{aligned} \tag{6.25}$$

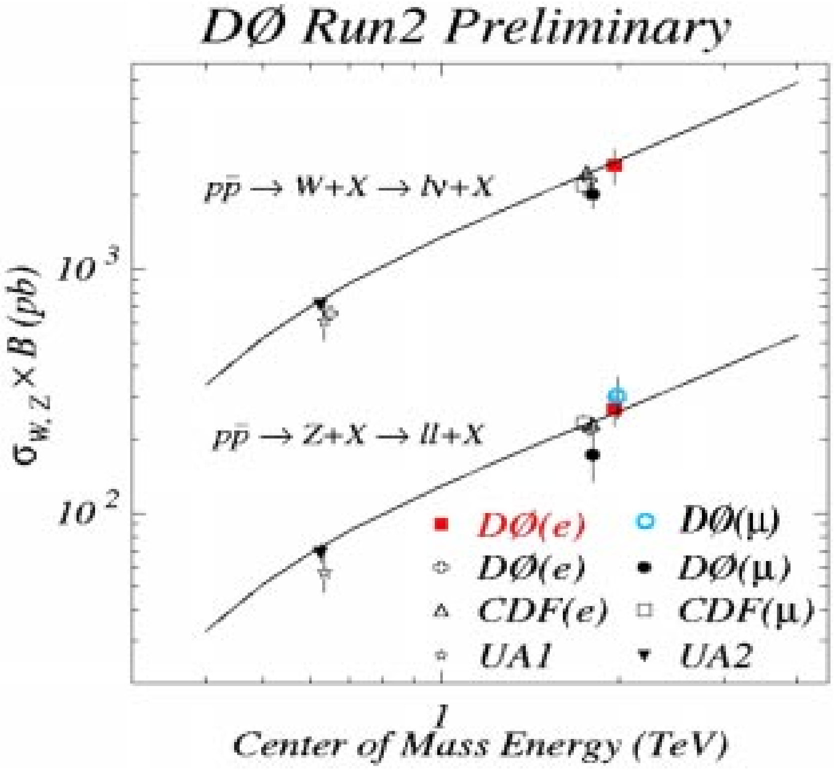

Figure 6.17: Inclusive W and Z production cross sections in p$\bar{\text{p}}$ collisions at various centre of mass energies. Experimental results (points with error bars)[58, 64, 65, 66] and theoretical prediction (solid lines)[67].

6.7 Future Improvements to this Analysis

Several improvements to the performance of DØ will have direct impact on this analysis.

First, the trigger and data acquisition systems have been upgraded, allowing a higher accept rate at each trigger level. The muon triggers themselves have also been significantly improved. The Level 1 trigger will soon be upgraded to include a trigger based on the muon drift chambers. Extra rejection is now coming from the Level 2 muon trigger and central track matching at Level 3 with the Level 3 muon trigger soon to be operational. As a result of these improvements, the pre-scale on the Level 1 single muon trigger has been reduced to less then 10 (from around 100). Soon, central track matching will be required at Level 1, allowing the removal of the pre-scale altogether. Offline muon identification has also been improved, with looser hit requirements in the muon system and improvements to segment reconstruction.

The central tracking has improved significantly. All the stereo fibres have been operational for several months and the offline track reconstruction has been improved by the implementation of a mixture of track reconstruction algorithms. It is also now possible to carry out the full track extrapolation described in Chapter 4 which will improve the muon track matching methods.

Finally, DØ has now recorded an integrated luminosity of around 65 pb^{-1}, more than 10 times the amount used for this analysis. With this data set, the systematic and statistical uncertainties could be greatly reduced. Also, with a useful single muon trigger, the methods used to measure the efficiencies may also be improved.

While it proved impossible to obtain a signal for $\mathrm{W} \rightarrow \mu\nu_\mu$ in the data used for this thesis, the single muon trigger now allows a measurement of $\mathrm{W} \rightarrow \mu\nu_\mu$and the W cross section. If both the W and Z^0 cross sections are measured, many of the systematic uncertainties cancel when taking the ratio,

$$\mathcal{R} = \frac{\sigma_W \times B(\mathrm{W} \rightarrow \mu\nu)}{\sigma_Z \times B(\mathrm{Z} \rightarrow \mu\mu)}. \tag{6.26}$$

This ratio can also be used to measure the W width, with input from theory and other experiments. First, the W branching fraction is extracted using the theoretical calculation of the ratio of the total cross sections:

$$B(\mathrm{W} \rightarrow \mu\nu) = \mathcal{R} \times B(\mathrm{Z} \rightarrow \mu\mu)\frac{\sigma_Z}{\sigma_W}, \tag{6.27}$$

using the LEP measurement of the Z^0 branching fraction. Then, the W width, Γ_W, is measured using the theoretical prediction for the partial width of the W, Γ_W^μ:

$$\Gamma_W = \frac{\Gamma_W^\mu}{B(\mathrm{W} \rightarrow \mu\nu)}. \tag{6.28}$$

With large statistics, the Tevatron experiments will be able to improve the precision of the W width measurement, which is currently [11]:

$$\Gamma_W = 2.118 \pm 0.042 \text{ GeV}, \tag{6.29}$$

which can be compared with the Standard Model prediction of:

$$\Gamma_W = 2.094 \pm 0.006 \text{ GeV}. \tag{6.30}$$

Chapter 7

Summary

The work described in this thesis was carried out at DØ, a multi-purpose particle detector located on the Tevatron proton anti-proton collider in Illinois, USA. The Tevatron is the highest energy facility in the world, with many exciting physics prospects over the next few years. Most significant are perhaps the measurements of the top quark and W boson masses, which tell us a great deal about the mechanism of electroweak symmetry breaking and the possible mass of the higgs boson. There is also the possibility that the higgs boson can be discovered at the Tevatron, but this depends critically on the higgs mass and the integrated luminosity delivered to the Tevatron experiments.

Run II at the Tevatron begin in 2000, and the shift from commissioning to physics analysis at DØ since then is reflected in the work described in this thesis. Chapter 3 reviewed some work carried out on the on-line monitoring framework for the silicon detector (SMT) at DØ. Two packages have been developed: a histogramming package (SMT-Examine); and an on-line event display. These are used to study the performance of the SMT on-line and are run at all times when DØ is recording data.

The SMT is an important part of the tracking system at DØ and Chapter 4 described a method developed to combine particle tracks with information from the different sub-detectors at DØ. This is achieved by extrapolating the reconstructed tracks through the DØ detector. At the time, there was no real data available, so the extrapolation has been tuned on simulated events. Good results are achieved, with possible improvements to come from improving some of the simplifying assumptions made in treating the material of the end-cap calorimeters. However, testing the code in real data is a higher priority.

The track extrapolation is most applicable to muon identification, but due to software issues could not be used on the data available for this thesis. Chapter 5 reviews muon reconstruction at DØ and describes the alternative track matching method developed for muons in the data used for this thesis. This method was subsequently adopted by the whole DØ collaboration and proved vital to the identification of the Z^0 resonance in the di-muon mass spectrum.

Having identified the Z^0 signal, it was possible to measure the production cross section (σ_Z) multiplied by muon branching fraction (B_μ), as described in Chapter 6. This measurement has large uncertainties, but revealed many things about the performance of the DØ experiment and analysis tools. The final result, based on an integrated luminosity of 4.57 ± 0.46 pb^{-1}:

$$\sigma_Z \times B_\mu = 309 \ \pm \ 31 \text{ (stat)} \ \pm \ 51 \text{ (sys)} \ \pm \ 31 \text{ (lum) pb}, \tag{7.1}$$

which is consistent with the measurement in the electron channel and the theoretical prediction. Many of the methods adopted to measure the efficiencies were motivated by the status of the detector at the time the data were recorded and can be improved in the future. The uncertainties are mainly statistics limited.

DØ is significantly closer to design performance, with improvements to the hardware, event triggers and offline event reconstruction. The Tevatron performance has also improved, and DØ has recorded more then ten times the luminosity used for this thesis. The $Z^0 \to \mu^+\mu^-$ cross section analysis will benefit hugely from these improvements, and as the precision is improved it can be used to test the understanding QCD production of the Z^0 boson. The Z^0 signal will continue to be used to calibrate the detector, reconstruction and analysis code developed at DØ. Recent improvements at DØ also allow a measurement of the $W \to \mu\nu_\mu$ cross section. From the ratio of the W and Z^0 cross sections it is possible to extract the W width, which is sensitive to new physics beyond the Standard Model. The Tevatron experiments will be able provide the world's best measurement of the W width over the coming years.

Appendix A

Multiple Scattering Conversions

In Chapter 4, multiple scattering is quantified in terms of a direction and position parameter:

$$\theta_0 \;=\; \frac{13.6 \text{ MeV}}{\beta p}\; z \sqrt{\frac{x}{X_0}}\; [1 \;+\; 0.038\; \ln(x/X_0)], \tag{A.1}$$

$$y_{rms} \;=\; \frac{x\theta_0}{\sqrt{3}}. \tag{A.2}$$

where p, β and z are the momentum (in units of MeV), velocity (as a fraction of the speed of light) and charge (in units of e) of the incident particle, x is the distance travelled in the material and X_0 is the radiation length of that material,

In addition, there is a correlation co-efficient between y and θ_0 [11]:

$$\rho_{\theta y_{rms}} = \frac{\sqrt{3}}{2}. \tag{A.3}$$

For use in the track extrapolation code, θ_0 and y_{rms} must be converted to the parameters used on the GTR cylinder and z plane surfaces. The corrections (denoted by σ_{ij}) are then added to the relevant terms in the track error matrix. For off-diagonal terms, one correction is calculated and the symmetry of the matrix used to update two terms (i.e. $\sigma_{ij} = \sigma_{ji}$).

A.1 Conversions for Cylinders

The parameters used in a cylinder are: $r, \phi, z, \alpha, \tan\lambda$ and q/p_T, as defined in section 4.1. The corrections to the diagonal elements of the error matrix are given by:

$$\sigma_{\phi\phi} = \frac{y_{rms}^2}{r^2}, \tag{A.4}$$

$$\sigma_{zz} = y_{rms}^2(1 + \tan^2\lambda), \tag{A.5}$$

$$\sigma_{\alpha\alpha} = \theta_0^2(1 + \tan^2\lambda) + \frac{y_{rms}^2}{r^2}, \tag{A.6}$$

$$\sigma_{\tan\lambda\tan\lambda} = \theta_0^2(1 + \tan^2\lambda)^2, \tag{A.7}$$

$$\sigma_{\frac{q}{p_T}\frac{q}{p_T}} = \theta_0^2\frac{q}{p_T}^2\tan^2\lambda. \tag{A.8}$$

The corrections to the off-diagonal error matrix elements are given by:

$$\sigma_{\phi\alpha} = \frac{\rho}{r} \times \left(\frac{y_{rms}^2}{r} + \theta_0 y_{rms}(1 + \tan^2\lambda)\right), \tag{A.9}$$

$$\sigma_{z\tan\lambda} = \rho x\theta_0 y_{rms}\sqrt{(1 + \tan^2\lambda)^3}, \tag{A.10}$$

$$\sigma_{\tan\lambda\frac{q}{p_T}} = \theta_0^2\frac{q}{p_T}\tan\lambda \times (1 + \tan^2\lambda). \tag{A.11}$$

A.2 Conversions for z Planes

The parameters used for a z plane are $z, x, y, dx/dz, dy/dz$ and q/p, as defined in section 4.1. To simplify the calculation of the z plane conversions, the track vector on the z plane is used to define a unit vector in the same direction. The x, y and z components of this unit vector are then calculated the usual polar angles θ and ϕ, along with the component of the vector parallel to the z plane ($\hat{r}$):

$$\hat{x} = \sin\theta\cos\phi, \tag{A.12}$$

$$\hat{y} = \sin\theta\sin\phi, \tag{A.13}$$

$$\hat{z} = \cos\theta, \tag{A.14}$$

$$\hat{r} = \sqrt{\hat{x}^2 + \hat{y}}. \tag{A.15}$$

The corrections to the diagonal elements of the track matrix are then given by:

$$\sigma_{xx} = y_{rms} \times \left(\left[\frac{\hat{x}}{\hat{r}\hat{z}} \right]^{2} + \frac{\hat{y}}{\hat{r}} \right), \tag{A.16}$$

$$\sigma_{yy} = y_{rms} \times \left(\left[\frac{\hat{y}}{\hat{r}\hat{z}} \right]^{2} + \frac{\hat{x}}{\hat{r}} \right), \tag{A.17}$$

$$\sigma_{\frac{\mathrm{d}x}{\mathrm{d}z}\frac{\mathrm{d}x}{\mathrm{d}z}} = \theta_0 \times \left(\frac{\hat{y}}{\hat{r}\hat{z}}^{2} + \left[\frac{\hat{x}/\hat{r}}{1 + (\frac{\hat{r}}{\hat{z}})^2} \right]^{2} \right), \tag{A.18}$$

$$\sigma_{\frac{\mathrm{d}y}{\mathrm{d}z}\frac{\mathrm{d}y}{\mathrm{d}z}} = \theta_0 \times \left(\frac{\hat{x}}{\hat{r}\hat{z}}^{2} + \left[\frac{\hat{y}/\hat{r}}{1 + (\frac{\hat{r}}{\hat{z}})^2} \right]^{2} \right). \tag{A.19}$$

Only one off-diagonal term is required for a z plane:

$$\sigma_{\frac{\mathrm{d}x}{\mathrm{d}z}\frac{\mathrm{d}y}{\mathrm{d}z}} = \theta_0 \times \left(\frac{\hat{x}\hat{y}}{[\hat{r}(1 + (\frac{\hat{r}}{\hat{z}})^2)]^2} - \frac{\hat{x}\hat{y}}{\hat{z}^2} \right). \tag{A.20}$$

Appendix B

Refitting Axial Fibre Tracks

Many of the particle tracks used in this thesis were reconstructed only in the fibre tracker, which lies between radii of 19.5 and 52 cm. The momentum resolution on these tracks can be significantly improved by re-fitting them to have a point of closest approach (PCA) of zero - effectively adding another measurement at a radius of zero. This is achieved through minimising the fit χ^2 for the track with the new PCA (denoted by r).

The original fit χ^2 of the track is minimised during track reconstruction. For small variations in r and $\frac{q}{p_T}$ of the track, the χ^2 of the track is given by:

$$\chi^{2\prime} = \chi^2 + \sigma_{r,r}(r' - r)^2 + 2\sigma_{r,\frac{q}{p_T}}(r' - r)\left(\frac{q}{p_T}' - \frac{q}{p_T}\right) + \sigma_{\frac{q}{p_T},\frac{q}{p_T}}\left(\frac{q}{p_T}' - \frac{q}{p_T}\right)^2, \quad \text{(B.1)}$$

where the primes indicate the varied parameters and $\sigma_{i,j}$ corresponds to the $(i,j)^{th}$ element of the track error matrix.

In this case, r' is set to zero, as we want to refit the track with a PCA of zero. Then, the value of $\frac{q}{p_T}'$ which minimises $\chi^{2\prime}$ will correspond to the optimum refitted curvature. To find the minimum in $\chi^{2\prime}$, the derivative is set to zero:

$$\frac{\mathrm{d}\chi^2}{\mathrm{d}\frac{q}{p_T}'} = 2\sigma_{r,\frac{q}{p_T}}(0 - r) + 2\sigma_{\frac{q}{p_T},\frac{q}{p_T}}\left(\frac{q}{p_T}' - \frac{q}{p_T}\right) = 0. \quad \text{(B.2)}$$

Rearranging give $\frac{q}{p_T}'$ in terms of the parameters and error matrix of the original track:

$$\frac{q}{p_T}' = \frac{q}{p_T} - \left(\frac{\sigma_{r,\frac{q}{p_T}}}{\sigma_{\frac{q}{p_T},\frac{q}{p_T}}} \times r \right). \tag{B.3}$$

In the data used for this thesis, a problem was found in the track error matrix and an additional factor of 16 had to be included, leading to the correction quoted in Chapter 5:

$$\frac{q}{p_T}' = \frac{q}{p_T} - \left(\frac{\sigma_{r,\frac{q}{p_T}}}{\sigma_{\frac{q}{p_T},\frac{q}{p_T}}} \times \frac{r}{16} \right). \tag{B.4}$$

Bibliography

[1] M.E. Peskin and D.V. Schroeder, "An Introduction to Quantum Field Theory", Perseus Books, 1995.

[2] F. Halzen and A.D. Martin, "Quarks and Leptons", John Wiley & Sons Inc, 1984.

[3] S. Weinberg, Phys. Rev. Lett. 19 (1967) 1264;
A. Salam, *Elementary Particle Theory*, ed. N. Svartholm (Almquist and Wiksells, Stockholm, 1969) p.367;
S.L. Glashow, J. Iliopoulos and L. Maiani, Phys. Rev. D 2 (1970) 1285.

[4] P.W. Higgs, "Spontaneous Symmetry Breakdown Without Massless Bosons", Phys. Rev. 145 (1966) 1156.

[5] M. Carena *et al*, "Report of the Higgs Working Group of the Tevatron Run 2 SUSY/Higgs Workshop", p-ph/0010338

[6] B.R. Martin and G. Shaw, "Particle Physics, Second Edition", John Wiley and Sons, 1997.

[7] A. Einstein, "Ist die Trägheit eines Körpers von sienem Energiegehalt Abhängig?", Ann.Phys. 17, 1905.

[8] LHC Study Group, "The LHC Conceptual Design Report", CERN/AC/95-05, 1995.

[9] LEP2 Team, "LEP Design Report: Vol. 3, LEP2", CERN/AC/96-01, 1996.

[10] S. Drell and T. Yan, Ann. Phys. 66, 578 (1971).

[11] K. Hagiwara *et al*, Phys. Rev. D 66, 010001 (2002).

[12] J. Thompson, "Introduction to Colliding Beams at Fermilab", FERMILAB-TM-1909, October 1994.

[13] G. Jackson (editor), "The Fermilab Recycler Ring Technical Design Report", FERMILAB-TM-1991.

[14] The CDF Collaboration, "The CDF II Detector Technical Design Report", FERMILAB-Pub-96/390-E.

[15] H.A. Bethe, "Molière's Theory of Multiple Scattering", Phys. Rev. 89, 1256 (1953).

[16] "The DØ Upgrade, the Detector and its Physics", Fermilab Pub-96/357-E.

[17] A. Lo *et al*, "Luminosity Monitor Technical Design Report", DØ Note[1] 3320, October 1997.

[18] "Design of the 2 Tesla Superconducting Solenoid for the Fermilab DØ Detector Upgrade", Fermilab Pub-098/047E.

[19] "DØ Silicon Tracker Technical Design Report", DØ Note 2169.

[20] "DØ Fibre Tracker Technical Design Report", 1997. Available online: http://d0server1.fnal.gov/users/stefan/www/CFT_TDR/CFT_TDR.ps.

[21] "DØ Fiber Tracking Group VLPC/Cryo Design Review", DØ Note 1536, November 1992.

---

[1] All DØ Notes can be obtained by contacting the author

[22] Adams *et al*, "Design Report of the Central Pre-shower Detector for the DØ Upgrade", DØ Note 3014, January 1996.

[23] A. Gordeev *et al*, "Technical Design Report of the Forward Pre-shower Detector for the DØ Upgrade", DØ Note 3445, May 1998.

[24] J. Kotcher, "Design, Performance and Upgrade of the DØ Calorimeter". FERMILAB-Conf-95/007-E, January 1995.

[25] T. Diehl *et al*, "Technical Design of the Central Muon System", DØ Note 3365, March 1998.

[26] T. Diehl *et al*, "Technical Design for the DØ Forward Muon Tracking Detector Based on Mini-Drift Tubes", DØ Note 3366, December 1997.

[27] T. Diehl *et al*, "Technical Design for the DØ Forward Trigger Scintillation Counters", DØ Note 3237, November 1997.

[28] M. Abolins *et al*, "DØ Run II Level 1 Trigger Framework Technical Design Report", June 1998,
http://www.pa.msu.edu/hep/d0/ftp/l1/framework/l1fw_tdr_05june98.txt.

[29] CTT Group, "Technical Design Report for the Upgrade L1/L2 Tracking Trigger", DØ Note 3551, January 1999.

[30] "DØ Run II Level 1 Calorimeter Trigger",
http://www.pa.msu.edu/hep/d0/l1/cal_trig/index.html.

[31] D. Edmunds *et al*, "Technical Design Report for the Level 2 Global Processor", DØ Note 3402, February 1998.

[32] H. Evans *et al*, "Silicon Track Trigger for the DØ Experiment in Run II - Technical Design Report", DØ Note 3510, September 1998.

[33] M. Adams *et al*, “Level 2 Calorimeter Preprocessor Technical Design Report”, DØ Note 3651, May 1999.

[34] A. Maciel and M. Fortner, “The Level 2 Muon Trigger Algorithms, DØ Note in preparation”, September 2000.

[35] A. Boehnlein *et al*, “Description of the DØ Level 3 Trigger Software Components”, DØ Note 3630, April 1999.

[36] M. Narain and F. Stichelbaut, “A Framework for Run II Offline Vertex Reconstruction”, DØ Note 3559, April 1999.

[37] T. Sjöstrand and L. Lönnblad, “PYTHIA 6.2”, LU TP 01-21 [hep-ph/0108264], August 2001.

[38] G. Corcella *et al* “HERWIG 6.5”, JHEP 0101 (2001) 010 [hep-ph/0011363]; hep-ph/0210213.

[39] Y. Fisyak and J. Womersley, “DØ GEANT Simulation of the Total Apparatus Response”, DØ Note 3191, September 1997.

[40] G. Graham *et al*, “Status of the Fast Simulation, PMCS”, DØ Note 4059, December 2002.

[41] S. Choi *et al*, “SMT Barrel Assembly”, DØ Note 3849, March 2001 .

[42] P. van Gemmeren, “Assembling of F-Disk Wedge Detectors”, DØ Note 3719, January 2000.

[43] F. Blekman, “Numbering Schemes for the DØ SMT”, DØ Note 3899, August, 2001.

[44] R. Yarema *et al*, “A Beginners Guide to the SVXIIe”, FERMILAB-TM-1892, October 1996.

[45] G. Briskin *et al*, “The DØ Level 3/Data Acquisition System for Run II”, DØ Note 3568, June 1998.

[46] G. Guglielmo and C. Moore, “DØ Run II Data Distributor Design”, DØ Note 3624, March 1999.

[47] H. Fox, “Online Calibration of the DØ Vertex Detector”, online presentation: http://www-d0.fnal.gov/∼fox/SmtCalib/SmtCalibWWW.htm.

[48] R. Illingworth, “Raw Data Format and Unpacking for the SMT”, DØ Note 3829, January 2001.

[49] R. Demina *et al*, “Charge distribution in SMT Clusters”, DØ Note 3981, April 2002.

[50] J. Yu and J. Kowalkowski, “DØ Run II Online Examine Framework Design and Requirements”, DØ Note 3578, January 1999.

[51] G. Hesketh, Online documentation:
http://www-d0.fnal.gov/∼ghesketh/examine/examine.html.

[52] L. Landau, J. Physics (USSR) 8 (1944) 201.

[53] S. Dean and G. Hesketh, “An Online Event Display for the DØ SMT Detector”, DØ Note 4078, January 2002.

[54] D. Adams, “Finding Tracks”, DØ Note 2958, July 1998.

[55] G. Hesketh, “Central Track Extrapolation Through the DØ Detector”, DØ Note 4079, January 2002.

[56] F. Déliot, “The Fit Algorithm in muo_trackreco”, November 2000. Available online:
http://d0-france.in2p3.fr/WORKING_GROUPS/MUONS/doc.ps.

[57] D. Whiteson, “Muon Tracking in the Calorimeter”, DØ Note 3996, July 2002.

[58] S. Abachi *et al* (DØ Collaboration), "Measurement of W and Z Boson Production Cross Sections", Phys. Rev. D. Letters 1999, FERMILAB PUB-99/015-E, hep-ex/9901040.

[59] F. Abe *et al* (CDF Collaboration), Phys. Rev. D 49 (1994) 1.

[60] R.K. Ellis, W.J Sterling and B.R Webber, "QCD and Collider Physics", Cambridge University Press 1996.

[61] Details of the electron identification at DØ can be found online: http://www-d0.fnal.gov/phys_id/emid/d0_private/certification/main_v1_3.html.

[62] M. Kado and R. Zitoun, "Measurement of the Z and W Boson Production Cross Sections in the Electron Mode in p$\bar{\rm p}$ Collisions at $\sqrt{s}$ = 1.96 TeV", DØ Note 4003, August 2002.

[63] J. Zhu and S. Eno, "WZ Generator for Run II", DØ Note 4103, March 2003.

[64] C. Albajar *et al* (UA1 Collaboration), Phys. Lett. B253, 503 (1991).

[65] J. Allitti *et al* (UA2 Collaboration), "A Measurement of the Z and W Production Cross Section and Determination of $\Gamma_{\rm W}$ at the CERN p$\bar{\rm p}$ Collider", Phys. Lett. B276, 365 (1992).

[66] F. Abe *et al* (CDF Collaboration), Phys. Rev. D 52 2624 (1994) 1.

[67] R. Hamberg, W.L. van Neerven and T. Matsuura, Nucl. Phys B359, 343 (1991); W.L. van Neerven and E.B. Zijlstra, Nucl. Phys. B382, 11 (1992).